Abnormal cardiac metabolism affects accelerated cardiac fibrosis and dysfunction in ACTC^{E99K} induced HCM

Anan Huang

St Peter's College

A thesis submitted to the Division of Medical Sciences at the University of Oxford for the Degree of Master by Research

Trinity Term 2025

Radcliffe Department of Medicine

University of Oxford

ABSTRACT

Hypertrophic cardiomyopathy (HCM) is an inherited cardiac disorder, with both monogenic and polygenic forms, affecting approximately 1 in 500 individuals. While its morbidity and mortality rates are lower than those of many other cardiovascular diseases (CVDs), patients with HCM often experience a poor quality of life and unfavourable clinical prognosis. To date, over 1000 genetic mutations have been identified as potential etiological factors for HCM. HCM patients typically present diastolic dysfunction, and abnormal systolic dysfunction has also been reported. Despite recent advances in mechanical interventions and pharmacotherapies, treatment options remain limited. Disease-causing mutations are most frequently found in genes encoding cardiac contractile proteins, particularly MYH7 and MYBPC3 (thick filament components), but also occur in thin filament protein genes such as ACTC, which encodes alpha-cardiac actin. Functional studies on HCM-linked contractile protein mutations indicate that they initially induce a hypercontractile state. This altered contractility is postulated to disrupt Ca^{2+} handling - potentially triggering Ca^{2+} dependent hypertrophic signalling- and impair cardiac energetics. However, the precise secondary mechanism through which these initial changes lead to remodelling and fibrosis remain elusive.

This study employed a previously characterized $ACTC^{E99K}$ mouse model, which recapitulates the human E99K missense mutation in alpha-cardiac actin known to cause HCM and apical hypertrophy. This model exhibited severe cardiac fibrosis (CF) and contractile dysfunction at an early stage. Pronounced cardiac hypertrophy, particularly in the apical region, was observed alongside increased fibrotic accumulation. Cardiac contractile function was significantly impaired from 10 weeks of age, as evidenced by a reduced ejection fraction. Mechanistically, transcriptomic analysis revealed aberrant expression of genes involved in cardiac energetics. Pathways related to cardiac metabolism were significantly downregulated, with both

glycometabolism and fatty acid metabolism found to be attenuated. Furthermore, mitochondrial metabolism and calcium homeostasis were disrupted in ACTC^{E99K} hearts. These findings suggest that abnormal cardiac metabolism contributes to the accelerated cardiac fibrosis and dysfunction in ACTC^{E99K}-induced HCM. The ACTC^{E99K} mutation induces early cardiac hypertrophy accompanied by accelerated fibrosis, with mitochondrial metabolic abnormalities and calcium dysregulation likely playing key roles in pathogenesis. This work validates the ACTC^{E99K} HCM model as a robust platform for detailed molecular investigation of HCM mechanisms.

Acknowledgements

I wish to express my sincere gratitude to my supervisors, Professor Hugh Watkins and Professor Charles Redwood, for invaluable guidance, unwavering support, and immense patience throughout my research. Their expert supervision and insightful mentorship have profoundly deepened my understanding of scientific inquiry. I am also deeply indebted to all members of the Watkins group for fostering a stimulating and collaborative research environment, which was indispensable for the completion of this work. I extend my special thanks to Dr. Ying-jie wang and Dr. Kamayani Singh for their insightful discussions and invaluable advice, particularly troubleshooting biochemical experiments. I am also thankful to Dr. Adam Lokman and Julia Beglov for their patient instruction in a wide range of essential laboratory techniques.

My appreciation goes to the staff at the Wellcome Trust Centre of Human Genetics (Radcliffe Department of Medicine, Cardiovascular Department of Medicine) for their generous assistance and support. I am grateful to my college (St Peter's), for its supportive community, which greatly alleviated the sense of solitude while studying abroad.

I acknowledge with thanks the China Scholarship Council (CSC) for the generous funding of my tuition and living expenses during my studies in Oxford.

Finally, and most importantly, I thank my family for their unconditional love and steadfast support throughout my time at Oxford. This achievement would not have been possible without them.

Acronyms and abbreviations

ACTC	Alpha-cardiac actin
ALPK3	α kinase 3
ATP	Adenosine Triphosphate
α-SMA	α-smooth muscle actin
AV	Aortic valve
BHF	British Heart Foundation
BSA	Bovine serum albumin
CAV3	Caveolin 3
CaMKII	Calcium/calmodulin-dependent protein kinase type II
CMR	Cardiac magnetic resonance
CPB	Cardiopulmonary bypass
CPT1a	Carnitine palmitoyltransferase 1a
CRYAB	Crystalline αB
CSA	Cross-sectional area
CVDs	Cardiovascular diseases
DAPI	4′, 6-diamidino-2′-phenylindole
DEGs	Differentially expressed genes
ECM	Extracellular matrix
ER	Endoplasmic reticulum
ETC	Electron transport chain

FACS	Fluorescence-activated cell sorting
FDA	Food & Drug Association
GDMT	Guideline-directed medical treatment
GO	Gene ontology
HBSS	Hank' Balanced Salt Solution
HCM	Hypertrophic cardiomyopathy
HF	Heart failure
HFpEF	Heart failure preserved ejection fraction
HW	Heart weight
KEGG	Kyoto encyclopaedia of genes genomes
LGE	Late gadolinium enhancement
LV	Left ventricular
LVEDd	Left ventricular end-diastolic diameter
LVEF	Left ventricular ejection fraction
LVESd	Left ventricular end-systolic diameter
LVPW	Left ventricular posterior wall
LVOTO	Left ventricular outflow tract obstruction
MAPK	Mitogen-activated protein kinase
mtDNA	Mitochondrial DNA
MR	Mitral regurgitation
MYBPC3	Gene encoding cardiac myosin-binding protein C

MYH7	Gene encoding beta-myosin heavy chain
MYL2	Myosin light chain 2
MYL3	Myosin light chain 3
MYH6	Gene encoding alpha-myosin heavy chain
OCT	Optimal cutting temperature
OXPHOS	Oxidative phosphorylation
PBS	Phosphate-buffered saline
PDGF	Platelet-derived growth factors
PFA	Paraformaldehyde
PIMSRA	Percutaneous intramyocardial septal radiofrequency ablation
PLN	Phospholamban
PVDF	Polyvinylidene difluoride
ROS	Reactive oxygen species
RIPA	Radioimmunoprecipitation assay
RYR	Ryanodine receptors
SAM	Systolic anterior motion
SCD	Sudden cardiac death
SERCA2a	Sarcoplasmic reticulum Ca^{2+} -ATPase 2a
SR	Sarcoplasmic reticulum
SRT	Septal reduction therapy
TA-BSM	Transapical beating-heart septal myectomy

TBST	Tris-buffered saline with 0.1% Tween 20 detergent
TCF21	Transcription 21
TE	Tris-EDTA
TEM	Transmission electron microscope
TL	Tibia length
TnI3	Troponin I type 3
TTN	Titin
TUNEL	Terminal-deoxynucleoitidyl Transferase Mediated Nick End Labeling
WGA	Wheat germ agglutinin

Table of Contents

Chapter 1. INTRODUCTION

Hypertrophic cardiomyopathy (HCM) is a common inherited heart disease with a prevalence of approximately 1:500 in the United States[1, 2]. It can be inherited as an autosomal dominant monogenic disorder, or as a more complex polygenic trait. The one-year and five-year mortality of HCM are 0.5% and 2.5%, respectively, which are lower than other cardiovascular diseases (CVDs) (**Figure 1**)[3]. Diagnosis primarily relies on the phenotypic hallmark of cardiac hypertrophy, often asymmetrical, as assessed by echocardiography or other imaging modalities. In adults, a maximum left ventricular end-diastolic wall thickness exceeding 13 mm (or 15 mm for greater specificity) defines clinical hypertrophy[4]. Apical HCM, a subtype characterized by predominant hypertrophy at the left ventricular apex, is also well-recognized[2]. The diagnosis is typically made after excluding secondary causes such as hypertension and valvular disease. Currently, no clear predilection for HCM based on sex, ethnic background, or geographic location has been established[5, 6]. Following the first description of a HCM patient by French pathologists in the 19th century, the disease was gradually recognized as a “familial cardiomegaly” with autosomal dominant inheritance[7-9]. In 1990, a mutation in the gene encoding beta-myosin heavy chain (MYH7) was the first genetic variant identified in HCM family, heralding the era of molecular genetics in this disease[10].

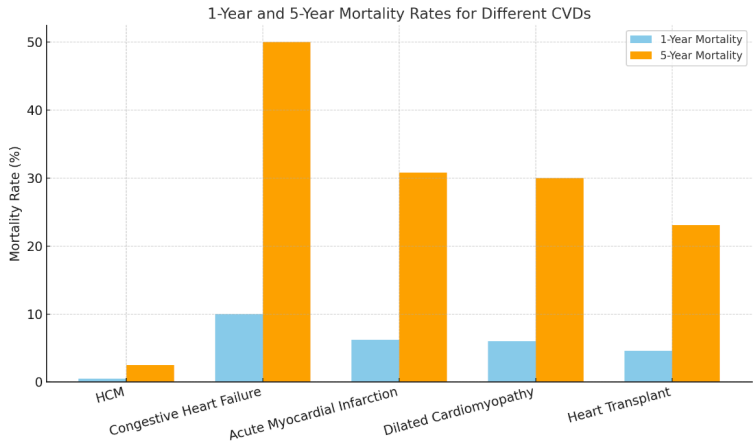

Figure 1. Comparative mortality rates of hypertrophic cardiomyopathy (HCM) among cardiovascular diseases (CVDs). This bar graph presents a comparative analysis of the one-year and five-year all-cause mortality rates for HCM alongside other common cardiovascular diseases, including heart failure (HF), ischemic heart disease (IHD), and aortic stenosis (AS). Data were synthesized from contemporary population-based studies and clinical registries. The height of each bar represents the mortality percentage at the specified time point. Although HCM exhibits lower one-year (0.5%) and five-year (2.5%) mortality rates compared to other CVDs, it is consistently associated with significant morbidity, a poor quality of life, and an unfavourable long-term clinical prognosis. *Adapted from [Maron et al., 2022[3]]. CVDs = cardiovascular diseases.*

1.1 Cardiac sarcomere

The physiological contraction of the heart depends on the coordinated function of the cardiac sarcomere, the fundamental contractile unit, which is activated by precise electrical stimulation (**Figure 2**). The sarcomere comprises two sets of filaments: thick and thin. Thick filaments, composed primarily of myosin, generate force and drive sarcomere shortening through ATP hydrolysis[11]. In contrast, thin filaments mediate the Ca^{2+}-dependent regulation of contraction[12]. The two filaments work together to regulate and drive the cardiac muscle contraction with well-timed synchrony[13]. Thick filaments are assemblies of myosin hexamers, each consisting of two heavy chains and four light chains. The C-terminal domains of the heavy chains form an α-helical coiled-coil rod that facilitates filament assembly, while

the N-terminal domains constitute the globular myosin heads (each associated with one essential and one regulatory light chain) responsible for actin binding, ATP binding, and ATPase activity. Cardiac myosin-binding protein C (MyBP-C, ~140kDa), encoded by the MYBPC3 gene, interacts with myosin via its N- and C-terminal domains, modulating the structural state and activity of the myosin head. The thin filament is primarily composed of actin, tropomyosin, and the troponin complex, which includes troponin C (the Ca^{2+}-binding subunit), troponin I (the inhibitory subunit), and troponin T (the tropomyosin-binding subunit). Additionally, titin, the largest of human proteins (~3MDa) and spans half a sarcomere from the Z-disc to the M-line, functioning as a crucial molecular spring and scaffolding element that contributes to passive and structural integrity[14-16].

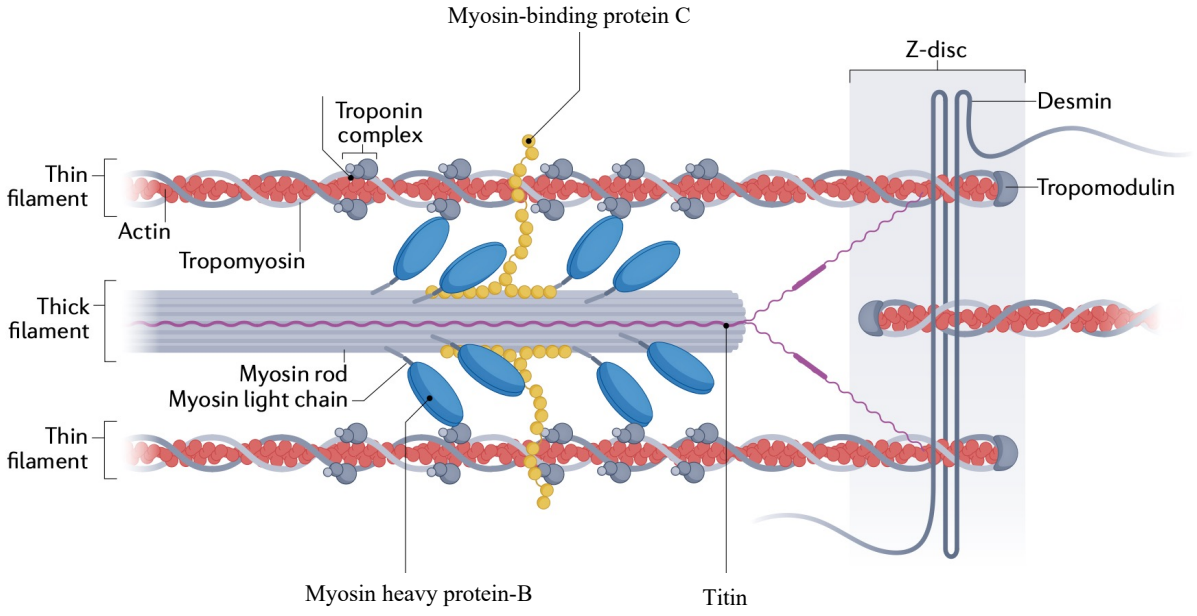

Figure 2. Architectural and regulatory components of the cardiac sarcomere. Schematic diagram detailing the highly ordered structure of the cardiac sarcomere, the fundamental contractile unit of the cardiomyocyte. The illustration highlights the interplay between the thick filaments (composed primarily of myosin heavy chains, MYH7, and associated with myosin-binding protein C, MyBP-C) and the thin filaments (composed of filamentous actin, ACTC1, tropomyosin, and the troponin complex TnC, TnI, TnT). The cyclic interaction of the myosin heads with actin, powered by ATP hydrolysis, drives filament sliding and contraction. The giant elastic protein titin is depicted spanning from the Z-disc to the M-line, functioning as **a**

molecular spring that determines passive stiffness and provides structural integrity. This figure underscores that HCM-causing mutations most frequently occur in the protein components illustrated here, disrupting the delicate balance of force generation and regulation. *Adpated from [Lehman et al., 2022[9]].*

1.1.1 Contraction of cardiac sarcomeres

Integrated cardiac contraction is triggered by electrical stimulation, which causes increased intracellular Ca^{2+} levels. An initial increase in intracellular Ca^{2+} levels is caused by opening of the L-type voltage-gated calcium channels and this leads to cascaded calcium release through activation of ryanodine receptors (RyR2) to release Ca^{2+} from the sarcoplasmic reticulum (SR); this is termed calcium-induced calcium release[17, 18]. The intracellular Ca^{2+} rises sufficiently to bind to the troponin C on the thin filament, which results in the interaction of troponin C and troponin I and weaking the inhibitory binding of troponin I to actin. Finally, the position of tropomyosin on the thin filament is changed and the myosin-binding sites on actin are exposed to myosin[19]. As the binding sites are exposed, the myosin binds to the thin filament, leading to strong cross-bridges to stabilize the link between thick and thin filament and generate the force[20].

1.1.2 Relaxation of cardiac sarcomeres

After the contraction is completed, the cardiac muscle must be relaxed for the next contraction. Therefore, the cytoplasmic Ca^{2+} needs to be reduced to allow dissociation from troponin C. This is achieved by two mechanisms: transport of Ca^{2+} either back into the SR or extracelluarly via the sodium-calcium exchanger. In human cardiomyocytes, the former mechanism predominates, mediated by the SR Ca^{2+} -ATPase 2a (SERCA2a) pump and regulated by phospholamban (PLN) on the SR membrane. Both SERCA2a and PLN (as negative regulator when dephosphorylated) work together to regulate the calcium uptake into SR[21].

1.1.3 Thick filament regulation of contraction

While the classical view of muscle regulation has centered on calcium-mediated activation of the thin filament, emerging evidence highlights the critical role of the myosin-containing thick filament in modulating contractility[22]. In resting muscle, a significant proportion of myosin motors are sequestered in an auto-inhibited conformation known as the interacting-heads motif (IHM), which sterically blocks their interaction with actin and reduces ATPase activity. This structural state is associated with a super-relaxed (SRX) biochemical state characterized by slow ATP turnover. Activation of contraction thus requires not only calcium-dependent thin filament activation but also the release of myosin motors from this inhibited state on the thick filament. This thick filament-based regulation is mediated by several key proteins, including myosin-binding protein-C (MyBP-C) and titin. MyBP-C, localized in the C-zone of the thick filament, stabilizes the IHM and may also form dynamic links with actin, thereby influencing both thin and thick filament activation. Titin, beyond its role as a passive elastic element, contributes to mechanosensing by transmitting stress to the thick filament backbone, promoting the transition of myosin motors from the OFF to the ON state[23]. Notably, pharmacological agents such as Mavacamten—a myosin inhibitor used in the treatment of hypertrophic cardiomyopathy (HCM)—target this regulatory system by stabilizing the IHM and reducing the number of myosin motors available for actin interaction. This therapeutic approach underscores the physiological and clinical relevance of thick filament-mediated regulation, particularly in the context of cardiac muscle where hypercontractility due to dysregulated myosin activity is a hallmark of HCM[24]. Thus, the thick filament represents a central node in a dual-filament regulatory paradigm, integrating mechanical and biochemical signals to fine-tune the strength and kinetics of muscle contraction in both skeletal and cardiac muscle.

1.2 Genetic basis of HCM

As early as 1990s, linkage analysis and DNA sequencing identified mutant alleles in families with monogenic HCM and over the past three decades, at least 1000 mutations associated with

HCM have been discovered[25, 26]. Current evidence firmly establishes the link between variants in genes encoding sarcomeric or sarcomere-associated proteins and HCM pathogenesis[27]. Several sarcomeric genes are recognized as canonical causative genes, including beta myosin heavy chain (MYH7), cardiac myosin-binding protein C (MYBPC3), alpha-cardiac actin (ACTC1), cardiac troponin I (TNNI3), cardiac troponin T (TNNT2)[2, 28]. In addition, variants in genes that indirectly regulate the sarcomere, such as filament C (FLNC), α kinase 3 (ALPK3), caveolin 3 (CAV3), and crystalline αB (CRYAB), have also been implicated in HCM[4] (**Table 1**).

Table 1. Genetic variants associated with HCM

This tables lists the major gene implicated in HCM pathogenesis, including those encoding sarcomeric proteins and sarcomere-associated proteins.

Thick filament	Thin filament	Z lines	M line	Ca^{2+} homeostasis	Sarcomere-associated proteins
MYH7	TNNT2	MYOZ2	OBSCN	JPH2	FLNC
MYBPC3	TNNI3/TNNC1/TPM1	ACTN2	TRIM63	PLN	ALPK3
MYL2 and MYL3	ACTC1	CSRP3	MYOM2		CAV3
TTN		TCAP			CRYAB
MYH6		FHL1			

β-myosin heavy chain encoded by MYH7 is the main component of the thick filament, which generates contractile force via the ATP-dependent interaction of α-cardiac actin in myosin. MYBPC3 stabilizes MYH7 in the thick filament, modulating cross-bridge cycling efficiency and synchronizing force production. TNNT2 anchors the troponin complex to tropomyosin, enabling calcium-dependent regulation of ACTC1-MYH7 interaction. In addition, FLNC stabilizes the sarcomeric Z-disc and cytoskeletal integrity, ensuring mechanical force transmission during contraction. ALPK3 regulates sarcomere assembly and cardiomyocyte maturation, with mutations causing impaired contractile protein organization. CAV3 modulates ion channel activity and β-adrenergic signalling in caveolae, affecting electrical stability and contractile responsiveness. CRYAB acts as a molecular chaperone, protecting sarcomeric proteins from stress-induced damage. Besides Mendelian inheritance, recent studies also highlight polygenic variation can also contribute to phenotypic variability[29].

1.2.1 Genetic variants in genes encoding thick filament proteins

In genes encoding thick filament proteins of the sarcomere, mutations in MYH7 and MYBPC3 are the most common causes of monogenic HCM[28]. In addition, but at lower frequency, mutations in myosin light chain 2 (MYL2), myosin light chain 3 (MYL3), TTN, and alpha myosin heavy chain (MYH6) are also responsible for the phenotype of HCM. Variants in the MYH7 and MYBPC3 genes are each identified in appropriate 20% of HCM patients [30, 31]. Although as rare causes of HCM (less than 1%), these two genes are identified as causes of early HCM [32]. TTN is the giant sarcomere protein expanding from M to Z lines, which is almost expressed in cardiomyocytes and skeletal muscles. Potential truncating variants are a rare cause of HCM but major causes of inherited DCM[33]. Finally, MYH6 gene encoding for alpha myosin heavy chain protein, accounts for less than 10% of the total myosin protein in the ventricular cardiomyocyte; there are few reports of genetic variants in MYH6 contributing to HCM [34].

1.2.2 Genetic variants in genes encoding thin filament proteins

The thin filaments in cardiomyocytes principally consist of ACTC1, troponin (subunits T, I and C) and tropomyosin. ACTC1 is predominant part of the thin filament and participates in generating force through interacting with MYH7 protein. Although genetic variants in the ACTC1 gene account for no more than 1% of HCM, a mouse HCM model based on the genetic mutation of ACTC1 was reported previously [35, 36]. The $ACTC1^{E99K}$ mutation, a pathogenic variant in the ACTC1 gene, has emerged as a critical model for studying hypertrophic cardiomyopathy (HCM), offering insights into both molecular mechanisms and translational implications. This mutation, located at a surface residue in actin subdomain 1, disrupts sarcomeric function by altering actin-myosin interactions and calcium (Ca^{2+}) sensitivity, leading to a cascade of structural and functional cardiac abnormalities.

Other genetic variants in genes encoding the protein constituents of the Z lines and M lines are rare causes of HCM and in addition, mutations in genes regulating calcium homeostasis or encoding sarcomere-associated proteins have also been identified as potential causes of HCM [4]. Genetic testing and family screening is strongly recommended in HCM families including first-line genetic testing, gene panels, exome sequencing or genome sequencing, which can be beneficial to identify family members at risk of HCM [2, 37].

1.3 Disease Mechanisms in Monogenic HCM

HCM mutations in contractile protein genes are typically missense mutations resulting in a single amino acid substitutions. It is postulated that these act as dominant-negative alleles, that is they lead to the expression of stable proteins that are incorporated into the sarcomere, where they affect contractile function. This has been validated in a number of cases which have indicated close to 1:1 ratios of wild type and mutant proteins, for example by the use of mass spectrometry to quantitate MYH7 variants and the anomalous migration of TPM1 variants by SDS-PAGE [38, 39]. The exception to this is approximately half of the mutations in MYBPC3 which are truncations; these are likely to act via haploinsufficiency. There is a considerable body of biochemical and biophysical work that has shown that HCM mutations in contractile proteins initially lead to a hypercontractile state, either the mutations in thick filament proteins leading to activation of myosin activity, or the mutations in thin filament proteins resulting in an increase in the Ca2+-sensitivity of contractile regulation [40]. These inherent changes in contractility have been postulated to affect Ca2+ handling - which may trigger Ca2+-dependent hypertrophic signalling – and cardiac energetics [40, 41]. The precise details of how these changes in contractility ultimately lead to remodelling and fibrosis remain unclear.

1.4 Functional Studies on the E99K mutation in ACTC

The work in this thesis focusses on the ACTC E99K mutation. This was first reported to cause HCM in a Spanish family and has since been among the most frequently reported mutations in ACTC. It is particularly associated with apical hypertrophy [42]. More than a dozen publications have since been published, examining the functional consequences of the mutation at the biophysical, biochemical, cellular and whole organ level. At the myofilament level, thin filaments composed of E99K mutant actin were shown to give a higher Ca^{2+}-sensitivity of contractile regulation than filaments composed on wild type actin. Moreover, the mutant desensitised the thin filament to protein kinase A phosphorylation of cardiac troponin I [35, 43]. In engineered heart tissue composed of iPSC-derived cardiomyocytes, the presence of the E99K mutation was associated with arrhythmic events [44]. In the overexpressing mouse model used in this thesis which had cardiac actin composed of c.50% mutant protein, the mutant hearts showed apical hypertrophy, in common with the nature of the hypertrophy in affected patients with the mutation[35]. However, the pathomechanism is complex. While heterozygous HCM mutations are often assumed to lead to a uniform 50% reduction in functional protein (haploinsufficiency) or a 50:50 mixture of wild-type and mutant protein (for missense mutations), emerging evidence challenges this simplistic view. Studies indicate that sarcomeric genes, including MYH7 and MYBPC3, are transcribed in stochastic, independent bursts. This burst-like transcription leads to significant cell-to-cell variation in the ratio of mutant to wild-type mRNA and, consequently, in the relative abundance of mutant and wild-type protein among individual cardiomyocytes[45]. The mouse model was found to exhibit cardiac contractile dysfunction with increased end-diastolic volume and end-diastolic pressure, and reduced relaxation rates compared with NTG mice. The initial report also found a high incidence of sudden death in the 28-to-45-day old window [35]. There has been no detailed study of the pathways involved in cardiac remodelling in this model.

1.5 Clinical manifestations and Pathophysiology

For HCM patients, their clinical manifestation ranges from limited to severe symptoms such as chest pain, syncope, dyspnoea and even sudden cardiac death. Many clinical manifestations result from 4 pathophysiological processes including left ventricular outflow tract obstruction (LVOTO) diastolic dysfunction, mitral regurgitation (MR) and myocardial ischemia[2]. Previous multi-centre studies showed there are several adverse events including heart failure (HF), stroke, arrhythmia and even death in HCM patients[46, 47].

Approximately two thirds of patients with HCM present with LVOTO at rest or during provocative manoeuvres, and only one third of patients have no obvious LVOTO [48-50]. Mitral valve, and septal wall, hypercontractile myocardium and various papillary muscle abnormalities participate in the formation of LVOTO, and the severity of LVOTO is highly affected by ventricular preload, afterload and contractility[51, 52]. Obstruction is generally defined as the peak LVOT gradient over 30 mmHg, and of 50 mmHg at rest or during provocative manoeuvres this may cause symptoms. HCM patients presenting gradients of LVOT less than 30 mmHg are recommended to perform provocative manoeuvres such as standing, Valsalva strain or exercise[53, 54]. To assess severity of HCM, it is feasible to use 2D and doppler echocardiography to assess peak velocity, but it is easy to under- or over-estimate the septal wall thickness compared with assessment using cardiac magnetic resonance (CMR)[55]. Appropriate clinical management of LVOTO depends on a clear understanding of obstructive physiology, and for the majority of HCM patients, initial usage of beta-blockers, non-dihydropyridine calcium-channel blocking agents, and disopyramide[50]. In addition, several mechanical interventions including septal myectomy, alcohol septal ablation or right ventricular pacing may also work in improving symptoms of LVOTO.

1.5.1 Diastolic dysfunction

HCM patients generally present with elevated intraventricular pressure and diastolic dysfunction, reflecting impaired ventricular relaxation and compromised hemodynamic

efficiency, which results in diastolic dysfunction with participation of increased cardiac stiffness, fibrosis, and altered energetics[2]. The diastolic dysfunction of HCM is characterized by increased left ventricular end diastolic pressure, and this increase further leads to raised left atrial pressure and pulmonary resistance[56]. The clinical manifestations in HCM patients with higher left diastolic pressure consists of exertional dyspnoea, peripheral edema, and heart failure with preserved ejection fraction (HFpEF). Secondary to increased diastolic pressure, elevated atrium pressure may lead to poor tolerance of atrial tachyarrhythmia in some patients[2].

1.5.2 Mitral regurgitation

Mitral regurgitation (MR) occurs in patients with HCM frequently due to drag forces from the aortic valve (AV) to attract the anterior mitral leaflet, which is called systolic anterior motion (SAM) [57]. In addition, approximately 10-20% of patients with HCM present with MR due to intrinsic abnormalities of the MV[57]. Multiple elements including excessive length of the mitral leaflet, anteriorly displaced papillary muscles, anomalous papillary muscle insertion, and anomalous mitral valve annulus lead to these intrinsic abnormalities of the MV[2]. The severity of SAM can be divided into three types including mild (no contact between mitral leaflet and ventricular septum), moderate (less than 30% systolic time of mitral leaflet-septal contact), severe (over 30% systolic time of mitral leaflet-septal contact). In East Asian patients, the presence of MR always implies a poor prognosis[58].

1.5.3 Myocardial ischemia

Ischaemic chest pain can occur in patients with HCM resulting from mismatch between myocardial oxygen supply and demand[2, 48]. Myocardial ischemia is associated with adverse ventricular remodelling and poor prognosis[59]. Myocardial ischemia is multifactorial with causes including microstructural, macrostructural and metabolic mechanisms revealed through post-mortem, biopsy, and imaging techniques[59]. In HCM, significant thickening of vessel

walls, specific luminal narrowing of small intramural coronary arteries, and abnormal arterial stiffness contribute to the potential myocardial ischemia[60, 61]. In addition, lower density of small vessels in septal and LV tissues also exacerbate myocardial ischemia[59]. In addition, LVOTO, and diastolic dysfunction both participate in myocardial ischemia of HCM through reduced coronary flow reserve (CFR) in the left anterior descending artery[62, 63]. Myocardial bridging, as epicardial coronary arteries tunnel through myocardium but not over it, leads to systolic compression of coronary arteries and can induce perfusion impairment in HCM[2, 48]. Approximately 20-40% of patients with HCM have such myocardial bridging in the heart[64].

1.5.4 Systolic dysfunction

Whilst Diastolic dysfunction is observed in many patients with HCM, whether HCM patients present with abnormal systolic function remain inconclusive. Previous literature demonstrated that HCM patients with specific variants of sarcomere related genes show a higher risk of long term left ventricular systolic dysfunction[46]. Compared to genetic variants in the MYH7 gene, mutations of MYBPC3 are susceptible to lower left ventricular ejection fraction (LVEF) in patients aged over 40 years old[65]. Although mutations of MYH7 lead to similar energetic and metabolic abnormalities in the myocardium, the failure of cell autophagy, accumulation of poison peptides and severe cardiac fibrosis may contribute to the age-related systolic dysfunction in patients with MYBPC3 mutations[66]. Left ventricular (LV) remodelling and systolic dysfunction associated HF may be severe complications of HCM.

In HCM, cardiac contractility is initially affected and this then triggers compensatory cardiac hypertrophy to maintain normal cardiac output. Different gene mutations may lead to varied extents of cardiac hypertrophy. Mutations in MYH7 are apt to cause severe cardiac hypertrophy but mutations in MYBPC3 may tend to induce a delayed cardiac hypertrophy[48]. Additionally, mutations in MYH7 may lead to higher energy cost of tension generation compared to that of mutations in MYBPC3[48]. Abnormal substrate metabolism and vascular remodelling may

also lead to accelerated myocardial fibrosis and ultimately contractile dysfunction in HCM[67]. Through CMR, late gadolinium enhancement (LGE), as one of the representative characteristics of myocardial fibrosis, is always progressive in HCM patients. This fibrotic process can be driven by impaired energetics and perfusion abnormality[67]. Abnormal fibrotic accumulation in HCM is often found in the septum and left ventricle and right ventricular insertion areas[68]. In addition, recent studies imply that pro-fibrotic effectors act early before the appearance of hypertrophic phenotype[69, 70].

1.6 Cardiac fibrosis in normal interstitium

In normal adult mammalian hearts, cardiomyocytes account for 75% of myocardial volume and are surrounded by an interstitial extracellular matrix (ECM) network[71]. This ECM matrix consists of not only type I or III collagen but also glycoproteins, glycosaminoglycans, proteoglycans and others[72]. It is critical for ECM matrix as a mechanical scaffold and to participate in mechanical transmission of contractile force. In addition, several other types of cardiac cell populations including immune cells, vascular mural cells are also enmeshed within cardiac ECM to execute biological functions[73, 74]. In the normal hearts, cardiac fibroblasts, located in the endomysium and perimysium, work and serve to build the structural integrity of cardiac ECM through the regulation of platelet-derived growth factors (PDGF)-α[75]. The biological function includes increased proliferation, contractile protein expression, cytokine secretion and fibrotic accumulation[76]. Fibroblasts are identified with expression of discoidin domain-containing receptor 2, PDGFR-α, and transcription factor 21 (TCF21)[76].

1.7 Cardiac fibrosis and HCM

Once the heart is injured by severe hypoxia or other damaging stimuli, cardiac fibroblasts are converted into myofibroblasts with expression of α-smooth muscle actin (α-SMA)[77]. Fibroblasts are activated and then lead to matrix remodelling through secreting and degrading

ECM proteins in the hearts[71]. Besides fibroblasts/myofibroblasts, other cell types also play a crucial role in fibrotic process including immune cells, endothelial cells, pericytes and vascular smooth muscle cells. Due to cardiac injury, a series of neurohumoral effectors, growth factors, and cytokines induce profibrotic intracellular signalling cascades through binding to specific cell receptors[78-81]. In HCM, cardiac fibrosis can be detected in young patients through CMR with obvious LGE[82]. Through detection of circulating biomarkers of collagen synthesis, emerging evidence suggests that the development of cardiomyocyte hypertrophy precedes the activation of fibrogenic pathways, resulting in delayed but progressive myocardial fibrosis in HCM[69]. In animal models, abnormal fibrotic accumulation is observed in the myocardium of many HCM genetic models [35, 70, 83]. Cardiac fibrosis may be not just a simple secondary response to HCM, and even further worsen the degree of injury through secreted ECM proteins[71].

A major pathological feature of manifest HCM is always energetic impairment[84]. Energetic abnormalities have been identified in different mouse models of HCM and in patients with HCM[85, 86]. Normally, the heart requires high energy consumption with continuous ATP demand for physiological function, and always uses different types of fuels including glucose, fatty acids, lactate and others[87]. Fatty acid β-oxidation provides the majority of energy source through consuming free fatty acids and in human HCM heart, fatty acid oxidation was decreased with increased reliance on ketone bodies and branched chain amino acids[88, 89]. In addition, several previous studies demonstrated that most HCM mutations have heterogeneous abilities to develop increased total force production and utilization of ATPase, which suggests excessive energy demand is needed in the myocardium[25]. Several enzymes related to cardiac metabolism are frequently dysregulated in HCM[90]. HCM always presents comprehensive energetic decompensation with low production of high energy phosphate metabolites and a decreased expression of mitochondrial genes[25]. Previous integrated omics

data indicated that abnormality of fatty acid metabolism dominated in HCM[89]. In addition, glycolysis and oxidative phosphorylation were also downregulated in a HCM model at the protein level[90]. Animal model or human HCM heart samples both showed significant mitochondrial dysfunction, suggesting impairment of oxidative phosphorylation [91]. The analysis of myectomy tissue of HCM also indicated abnormality of oxidative mitochondrial metabolism, which suggested mitochondrial respiratory function might be impaired in HCM[84]. Previous literature suggests that impairment of sarcomere energetics leads to an abnormal increase of reactive oxygen species (ROS) and eventually mitochondrial dysfunction through a reduction in the Krebs cycle activity[92]. In HCM, excessive usage of ATP may produce more ADP and further induce oxidative stress[92]. In addition, abnormal bonding of $Ca2^{+}$ and sarcomere proteins increases the $Ca2^{+}$ sensitivity, which leads to less $Ca2^{+}$ participating in the Krebs cycle.

For HCM patients, the characteristic feature of diastolic dysfunction may be attributed at the cardiomyocyte level to increased resting calcium levels, decreased calcium transients and abnormal expression of calcium handling machinery[93]. Thus, abnormality of calcium homeostasis may be one of potential pathway to the pathophysiological progression of HCM. Aberrant calcium related genes in HCM can be split into genotype-dependent and independent genes[94]. Genotype dependent calcium related genes could induce adverse downstream effects on hypertrophic signalling in specific sarcomeric mutation induced HCM[93]. On the contrary, a previous study reported that SERCA2 activity was downregulated in all HCM samples with no association to the type of sarcomeric mutations, which suggested it might be a common mechanism of calcium mishandling in HCM[94].

1.8 Treatment of HCM

Although many patients with HCM are asymptomatic and current medical treatment is limited, clinical management options are still needed including lifestyle modification, genetic screening,

drug or surgical therapy for symptom control[2, 95]. For pharmacotherapy in HCM, heart rate control and negative inotropic regulation are main targets. Until now, in clinical practice, beta blockers or calcium channel blockers are recommended to decrease heart beats, while disopyramide are used due to its negative inotropic effect[96]. In addition, surgical myectomy, and several transcatheter therapies are also being performed in HCM with promising therapeutic effects[97-100] (**Figure 3**).

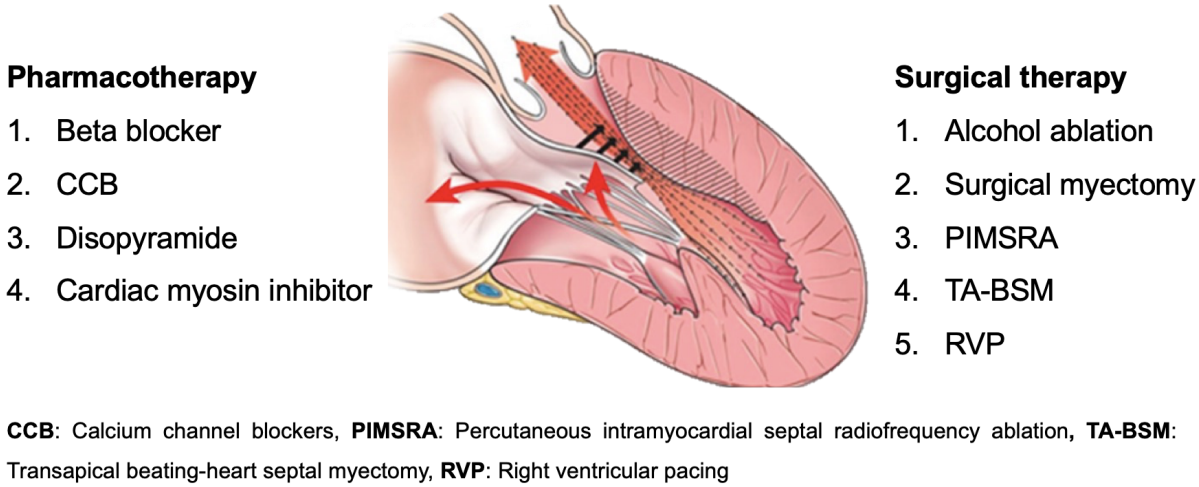

Figure 3. Contemporary therapeutic landscape for obstructive hypertrophic cardiomyopathy. This flowchart summarizes the current guideline-directed management strategies for patients with symptomatic oHCM, categorized into pharmacotherapy and invasive (surgical/catheter-based) therapies. Pharmacological options (left) include beta-blockers, non-dihydropyridine calcium channel blockers (CCB), disopyramide, and the novel cardiac myosin inhibitor (Mavacamten), all aimed at reducing left ventricular outflow tract (LVOT) gradient by modulating contractility and heart rate. Invasive septal reduction therapies (SRT) (right) are reserved for patients with drug-refractory symptoms and significant obstruction, including surgical septal myectomy, alcohol septal ablation, and emerging percutaneous techniques such as percutaneous intramyocardial septal radiofrequency ablation (PIMSRA) and transapical beating-heart septal myectomy (TA-BSM). Right ventricular pacing (RVP) is a niche option. The inset diagram illustrates the pathophysiological hallmarks of oHCM: a black arrow indicates the dynamic LVOT obstruction caused by systolic anterior motion (SAM) of the mitral valve, and a red arrow denotes the consequent mitral regurgitation (MR). The management goal is to alleviate symptoms by mitigating these mechanical sequelae. *Adpated from [Hutt & Desai, 2024[95]].*

1.8.1 Pharmacotherapy

Beta blockers are given to most patients with HCM, which reduces LVOT gradient and improves symptoms. Oral use of beta blocker lowers heart rates, decreases ventricular wall tension followed by decrease of excessive cardiac oxygen requirement. In addition, beta blocker can also promote coronary perfusion through prolonging diastolic period. As an anti-arrhythmic drug, beta blockers also reduce supraventricular or ventricular arrhythmias by blocking the activity of sympathetic nerves[2]. If the maximum tolerated dose of beta blockers cannot achieve the heart rate control, non-dihydropyridine calcium channel blockers are also used in HCM patients. The usage of calcium channel blockers reduces of LV diastolic pressure and increases LV filling[101]. Both beta blockers and non-dihydropyridine calcium channel blockers have vasodilator effects, which limits its use in HCM patients with low blood pressure. Previous study reported that disopyramide, as a sodium channel blocker with no vasodilator effect, can lead to a decrease of LVOT gradient and improve symptoms in HCM[102]. Recently, a novel drug called mavacamten, a cardiac myosin inhibitor targeting the binding site of cardiac myosin to actin, has been approved by the Food & Drug Association (FDA) with promising therapeutic effect on HCM with LVOT obstruction[103, 104].

1.8.2 Non-drug treatment

In HCM patients with LVOT obstruction, pharmacotherapies are insufficient to relieve severe drug-refractory symptoms completely, and septal reduction therapy (SRT) is required. Current guidelines recommend that SRT can be performed in patients with obstructive HCM who have refractory symptoms despite guideline-directed medical treatment (GDMT)[2]. Traditional SRT consists of surgical myectomy and alcohol septal ablation, and several new techniques have also been reported to have promising therapeutic effects on obstructive HCM[50, 97, 99, 100, 105, 106].

Compared to alcohol ablation, HCM patients aged over 65-years-old who underwent surgical myectomy have lower mortality and need for redo SRT during the first 2-years, while no difference at 4-year after SRT[105]. In the Sarcomeric Human Cardiomyopathy Registry (SHARE), 30-day mortality is 0.4% after SRT including alcohol ablation and surgical myectomy and 4% HCM related death is identified after 6.8 years follow-up. These results suggest that alcohol ablation and surgical myectomy may be appropriate treatment. Percutaneous intramyocardial septal radiofrequency ablation (PIMSRA) is also performed in obstructive HCM guided by echocardiography. Obstructive patients with HCM underwent PIMSRA show an obvious relief of symptoms with better hemodynamic in long-term follow-up[99]. Traditional surgical myectomy requires cardiopulmonary bypass (CPB) which may increase CPB related complications and struggles to determine the resected extent of the ventricular septum in an arrested heart[100]. A novel transapical beating-heart septal myectomy (TA-BSM) was developed via a minimally invasive procedure and reducing surgical trauma due to its real-time guiding[100]. Moreover, a retrospective clinical trial revealed that right ventricular pacing (RVP) could alleviate symptoms and enhance exercise capacity[107]. Dyssynchronous ventricular activation, delaying lateral wall contraction relative to septal contraction induced by RVP may weaken myocardial contractility and eventually enlarge outflow tract during systolic period.

1.9 Hypothesis

The potential secondary mechanisms mediating cardiac fibrosis and remodeling in HCM remain unclear. Whether cardiac metabolic dysfunction contributes to the accelerated CF and cardiac dysfunction needs be clarified. In this work, I hypothesize that abnormal cardiac metabolism occurs at an early stage of HCM, and this metabolic dysfunction may lead to accelerated cardiac fibrosis and contractile dysfunction. In addition, cardiac calcium homeostasis imbalance may also promote abnormal fibrotic accumulation and cardiac pump

function. In my work, a specific mouse model of HCM ($ACTC^{E99k}$ mutation) was used due to its early cardiac fibrosis and dysfunction as early as 10-week based on our previous work. In my work, the degree of fibrotic accumulation and cardiac contractile function was evaluated at different time-points. Bulk RNA sequencing was performed to find out whether cardiac metabolism or calcium homeostasis was significantly changed in HCM at different points. Finally, relevant pathways were further verified to support the significant role of cardiac metabolism and calcium homeostasis.

Chapter 2. METHODS and MATERIALS

$ACTC^{E99K}$ mice (10-, 24-, 54-, 60- weeks old) used in my study were originally generated by Prof. Steve Marston (Imperial College London) on a C57BL10xCBA/Ca hybrid background and subsequently bred in our Oxford laboratory for over 10 generations. All experimental animals were housed in the British Heart Foundation (BHF) animal facility at the Wellcome Centre for Human Genetics (WHG). All procedures involving animals were conducted in accordance with the UK Animals (Scientific Procedures) Act 1986 (PPL: P37BA1809 held by HOUMAN ASHRAFIAN). Mice was euthanized by cervical dislocation, and hearts were rapidly excised and immersed in ice-cold Hank' Balanced Salt Solution (HBSS) for subsequent processing. The tibia was collected concurrently to account for growth variations. Heart weight (HW) and tibia length (TL) were recorded for each mouse, and HW/TL ration was calculated as an index of cardiac hypertrophy.

2.1 Echocardiography

Age- and sex- matched $ACTC^{E99K}$ and $ACTC^{NTG}$ mice (n = 5-16 per group) underwent standard transthoracic echocardiography. All echocardiographic measurements were conducted by lab technician, and echocardiographic analyses were blinded to the genotype. Briefly, mouse was anesthetized by 1-3% isoflurane delivered in oxygen via a nose cone or induction chamber to maintain sedation and regular breathing. Body temperature was maintained using a heating pad, and Electrocardiography (ECG) leads were attached to monitor heart rate and rhythm. Chest fur was removed, and pre-warmed ultrasound gel was applied. The isoflurane concentration was adjusted to maintain a physiological heart rate of 400-500 beats per minute. An ultrasound transducer (MX550d, Vevo 3100) was positioned to obtain left ventricular long-axis and short-axis views (at the papillary muscle level). M-mode echocardiography was recorded over at least five cardiac cycles. Left ventricular end-diastolic diameter (LVEDd), end-systolic

diameter (LVESd), and left ventricular posterior wall (LVPW) thickness were measured from M-mode images. All measurements were averaged over five consecutive cycles. Left ventricular ejection fraction (LVEF) was calculated as follows

$$LVEF(\%) = \frac{(LVEDD^2 - LVESD^2)}{LVEDD^2} \times 100$$

2.2 Histopathology and Immunofluorescence

2.2.1 Preparation of paraffin sections

Heart tissues were excised from the chest chamber immediately after euthanasia and rinsed by ice-cold phosphate-buffered saline (PBS). The myocardial tissue was moved into 4% paraformaldehyde (PFA) for 24 h. The samples were dehydrated through a graded series of ethanol from 70% ethanol to 100% ethanol for 1 h and added into 100% ethanol with another 1 h. All the tissues were added into different xylene for 2 h and then immersed into melted paraffin wax (60°C) for 2h (**Table 2**). Once the paraffin infiltration was completed, the heart tissue was put into the moulds filled with melted paraffin. The moulds were transferred to the cooling platform until the paraffin solidified. The embedded cardiac tissues were removed from the moulds and then trimmed appropriately for further use.

Table 2. Dehydration protocol for heart tissue processing for paraffin embedding.
This table outlines the stepwise ethanol and xylene treatment used to dehydrate cardiac tissues prior to paraffin embedding and sectioning

Step	Reagent	Alcohol	Duration (mins)
1	Ethanol	70%	60
2	Ethanol	80%	60
3	Ethanol	95%	60
4	Absolute Ethanol (I)	100%	60
5	Absolute Ethanol (II)	100%	60
6	Xylene I	100%	30
7	Xylene II	100%	30

The trimmed paraffin blocks were cooled on the ice water for 30 min and then sectioned into 5 μm thick slices by rotary microtome. All the sections were floated on a warm water (40°C) to make the section flat, and finally mounted on glass slides.

The slides were then deparaffinized in xylene for 10 mins for twice. The slides were then treated through a gradation of ethanol from 100% ethanol to 70% ethanol (3-5 mins for each concentration) and then rinsed into distilled water for 5 min (**Table 3**).

Table 3. Hydration protocol for paraffin-embedded tissue sections.

This table describes the rehydration steps for paraffin sections prior to histological or immunohistochemical staining.

Step	Reagent	Alcohol concentration	Duration (mins)
1	Xylene I	-	10
2	Xylene II	-	10
3	Absolute Ethanol (I)	100%	5
4	Absolute Ethanol (II)	100%	5
5	Ethanol	95%	3
6	Ethanol	90%	3
7	Ethanol	80%	3
8	Ethanol	70	3
9	Distilled water	-	5

2.2.2 Picrosirius red staining

The slides were immersed into picrosirius red solution for 1h at room temperature (RT) and then gently rinsed by 0.5% acetic acid solution for 2 min at RT to remove excessive dye. The slides were then transferred into ascending grade ethanol from 70% ethanol to 100% ethanol (3 min for each) and 100% ethanol for another 2 min. The slides were finally cleared in xylene for twice (5 mins for each) and then was mounted by resin-based mounting medium and covered with coverslips. After staining completed, all slides were scanned by Aperio CS2 digital slide scanner and the digital images were imported into FIJI Image J for semi-quantitative analysis of fibrotic accumulation. In brief, fibrotic deposition was semi-quantified by the percentage of the left ventricle area.

2.2.3 Immunofluorescence

For Immunofluorescence, heart samples were harvested and then rinsed by cold 1 × HBSS buffer to remove excessive blood. Heart tissues were split into two parts through long-axis, and then put into ascending grade sucrose solution for dehydration at 4 °C (**Table 4**).

Table 4. Dehydration protocol for frozen tissue preparation.

This table details the sucrose gradient used for cryoprotection of cardiac tissues prior to frozen sectioning.

Step	Reagent	Alcohol concentration	Duration (hours)
1	Sucrose I	10%	2-4
2	Sucrose II	20%	overnight
3	Sucrose III	30%	12

Tissues were immersed into a cryomold by optimal cutting temperature (OCT) compound, and these cryomolds were put onto a pre-cooled platform to snap-freeze the samples. Samples were frozen at -80°C until sectioning. Before sectioning, samples were placed into a cryostat chamber at -25°C, and the sectioning thickness adjusted to 8 μm. The tissue was trimmed appropriately, and then cut into default thickness smoothly and continuously. The sections were transferred to pre-cooled glass slides by a brush gently and stored at -80°C for further staining.

Slides were equilibrated at RT for 10 mins, and then fixed with 4% PFA (with PBS) for 15 mins at RT. Slides were washed with PBS at RT 3 times (5 mins each) to remove residual PFA. Slides were then permeabilized with 0.1% Triton X-100 for 10 mins at RT followed by washing with PBS (3 times, 5 mins for each). The slides were blocked using 5% bovine serum albumin (BSA) for 2 hours at 4°C. Alexa Fluor 488 labelled wheat germ agglutinin (5mg, WGA, Invitrogen, W11261, Carlsbad, USA) was diluted into 5 ml PBS to get working solution (1mg/mL). Appropriate volume of WGA (final concentration of 5 μg/mL) was added onto the slides, and the slides were incubated overnight at 4°C in a dark humidified chamber. After the

incubation completed, residual WGA solution was washed by PBS (3 times, 5 min for each). To mark the cell nuclei, 4′, 6-diamidino-2′-phenylindole (DAPI) at dilution of 1:1000 was added onto the slides at RT for 5 mins, and unbound DAPI was washed by PBS (3 times, 5 mins for each) in a dark humidified chamber. Mounting medium was added onto the slide and the slide was covered by mount coverslips. All the samples were imaged by confocal fluorescence microscopy in the dark (**Table 5**).

Table 5. Immunofluorescence staining protocol.

Step-by-step procedure for immunofluorescence staining of frozen heart sections, including fixation, permeabilization, blocking, and staining with WGA and DAPI.

Step	Reagent	Concentration (in PBS)	Temp	Duration
Equilibration	-	-	RT	10 mins
Fix	PFA	4%	RT	15 mins
Permeabilization	Triton X-100	0.1%	RT	10 mins
Block	BSA	5%	4°C	2 hours
Staining	WGA	5 μg/mL	4°C	Overnight
Staining	DAPI	1:1000 (1mg/mL)	RT	5 mins

2.3 Bulk RNA Sequencing

Total RNA was extracted from ventricular tissues using the Rneasy Midi Kit according to the manufacturer's instructions. In brief, appropriate ventricle samples from $ACTC^{E99K}$ and $ACTC^{NTG}$ mice at 10-week, 24-, 60-week were homogenized with 350 uL RLT buffer using a Rotor-stator homogenizer for 45 s. The tissue lysate was centrifuged for 10 mins at 5000 g and the supernatant collected. An equal volume of 70% ethanol was added to the supernatant and mixed by shaking vigorously. Samples were applied to RNeasy Midi columns and centrifuged

for 5 mins at 5000g; columns were washed with Buffer RW1 followed by centrifugation at 5000g for 5 mins. Appropriate Buffer RPE was then added into RNeasy column to wash through centrifugation at 5000g for 2 mins and 5 mins respectively. After drying the RNeasy silica-gel membrane, appropriate volume of RNAsse-free water was added onto the RNeasy silica-gel membrane, and the RNA was collected after centrifugation at 5000g for 3 mins. Afterwards, total RNA was diluted to appropriate concentration to quantify using Quant-IT RiboGreen RNA Assay Kit. The integrity and purification of RNA were also assessed by high sensitivity RNA ScreenTape and NEBNext Ultra^{TM} Directional RNA Library prep Kit for Illumina. Only samples with a high quality of RNA integrity (RNA Integrity Number > 7) were accepted for further sequencing. After the Libraries were built and quantified, all the samples were sequenced by a Nova Seq6000 platform using 150PE strategy.

After sequencing, raw sequencing data are saved as FASTQ files by the Illumina's proprietary software. Under the environment of Linux platform, FASTQ files are imported and analysed by the software of FastQC to identify low-quality bases, adapter contamination, and over-represented sequences, and then trimmed by the software of CutAdapt v2.10. For reference alignment, the raw data are aligned to the mouse reference genome (GRCm39) by STAR v2.7.3a, and the annotation was processed by featureCount v1.6.4. The raw gene count matrix was collected and finally imported into the R v4.1.0 for further use. Genes with extremely low expression were ruled out from the matrix.

The raw gene counts were normalized, and differential analysis performed to acquire differentially expressed genes (DEGs) with adjusted *P*-value < 0.05 and log2 fold-change > 1 by edgeR package v3.40.2. Gene ontology (GO) enrichment analysis was performed to list the significant pathways involved in biological processes and cell components, and molecular functions. Kyoto encyclopaedia of genes genomes (KEGG) pathway enrichment analysis was

performed to investigate the potential biological pathways based on the known DEGs. To interpretate and visualize the results clearly, volcano maps, bubble maps and heat maps were depicted to present the difference expression of certain genes between $ACTC^{E99K}$ and $ACTC^{NTG}$ group by ggplot2 package in R.

2.4 Protein extraction and Western blotting

Ventricular tissues from $ACTC^{E99K}$ and $ACTC^{NTG}$ mice at 10-week, 24-, 60-week were rinsed to remove blood and then put into liquid nitrogen for snap-frozen. All samples were put into lysis buffer to lyse the tissue to collect total protein. The lysis buffer consists of Radioimmunoprecipitation assay (RIPA) buffer, and protease and phosphatase inhibitor cocktails (100 ×). All samples with appropriate lysis buffer were homogenized on ice for 30 mins. The supernatant was acquired after centrifugation at 12,000 rpm for 15 min at 4℃ and moved to a new tube.

2.4.1 BCA assay

For each sample, the concentration of total protein was quantified by BCA protein assay kit and diluted to appropriate concentration for further experiment according to the manufacturer's instruction. 2000 μg/mL BSA solution was descending diluted by lysis buffer to obtain a series of protein standards with final concentration from 0 μg/mL to 2000 μg/mL (**Table 6**).

Table 6. Procotocl for BCA protein assay.

Preparation of bovine serum albumin (BSA) standards and sample dilution scheme for protein concentration quantification using the bicinchoninic acid (BCA) assay.

Vial	Diluent Volume (µL)	BSA source and Volume (µL)	Concentration (µg/µL)
A	0	500 of stock	2000
B	125	375 of stock	1500
C	200	200 of stock	1000
D	200	200 of vial B	750
E	200	200 of vial C	500
F	200	200 of vial E	250
G	200	200 of vial F	125

The BCA working reagent was acquired as mixing 50 parts BCA reagent A with one part of BCA reagent B (50:1). To quantify the concentration of each sample, all the standards and samples were replicated for 3 times. Each BCA standard, samples blank, and lysed sample were added into 1.5 mL tubes and then 250 µL working reagent was also added into the tubes followed by appropriate vortex. All standards, sample blank, and lysed samples were transferred into 96-well plate. The plate was incubated in a water bath at 37°C for 45 minutes. After incubation, the plate was cooled at RT and then inserted into microplate reader to measure the absorbance of each well at 562 nm. According to the absorbance value and known concentration of the standards, a standard curve and relative formula were generated to calculate the concentration of each protein sample based on the absorbance. For further gel electrophoresis, all of protein samples were denatured and adjusted to the same concentration by NuPAGE LDS Sample Buffer (4 ×), NuPAGE Reducing Agent (10 ×), and appropriate lysis buffer at 70°C for 10 mins (Table). All the samples were stored at -80°C for further use.

Table 7. Preparation of Western blotting samples.

Composition of denatured protein samples, including loading buffer and reducing agent

Reagent	**Sample**
Sample	X uL
NuPAGE LDS Sample Buffer (4 ×)	2.5 uL
NuPAGE Reducing Agent (10 ×)	1 uL
Deionized Water	to 6.5 uL
Total Volume	10 uL

2.4.2 Electrophoresis

NuPAGE Bis-Tris gels were used to separate different molecular weight of proteins. MES SDS or MOPS SDS running buffer were selected based on the different molecular weight of target proteins. Potential selecting strategies of NuPAGE Bis-Tris gels were made in accordance to the migration patterns of protein standards on NuPAGE Bis-Tris gels from ThermoFisher Scientific (**Figure 4**).

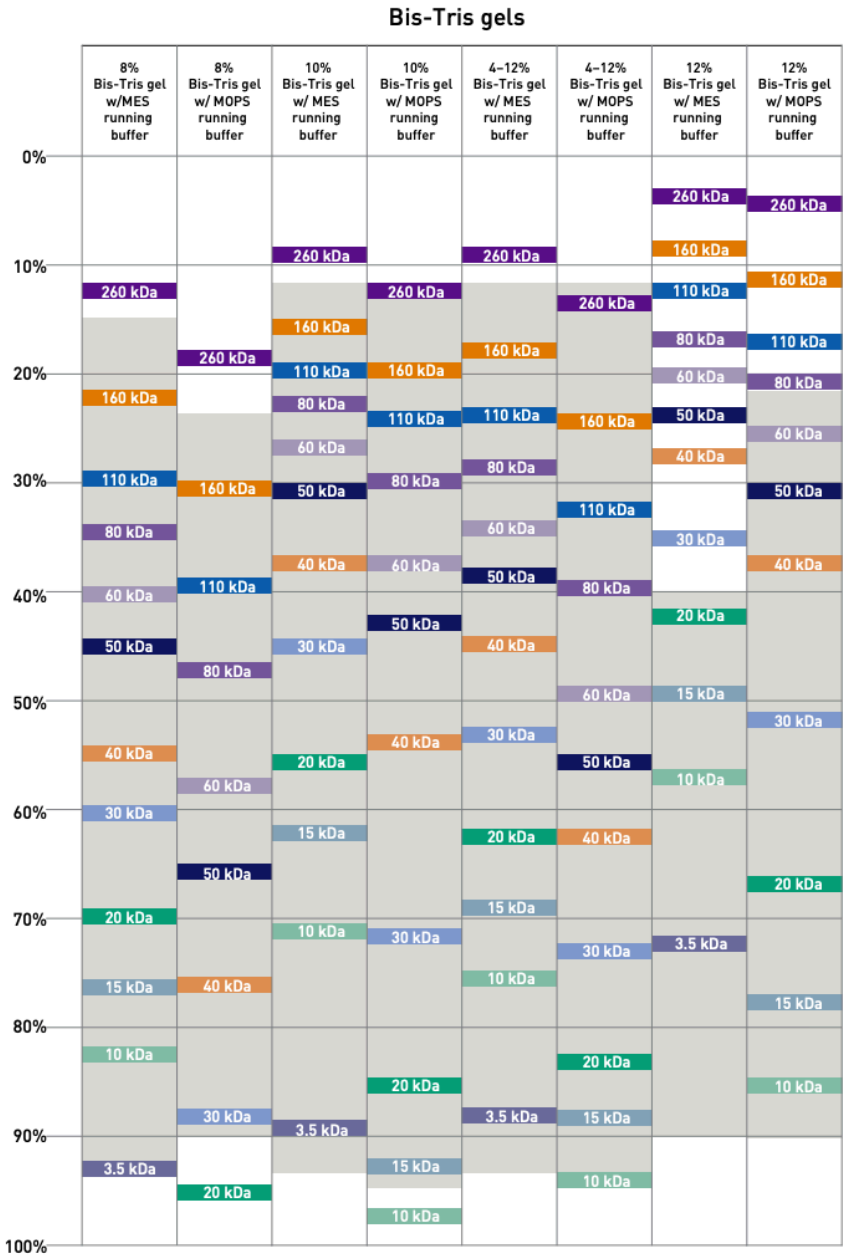

Figure 4. Migration patterns of protein standards on NuPAGE Bis-Tris gels. This reference image illustrates the electrophoretic migration of protein molecular weight markers on NuPAGE Bis-Tris gels, used to estimate the molecular weights of target protein in Western blot experiments. *From Thermofisher Scientific product documentation*.

The MES SDS Running buffer or MOPS SDS Running buffer were prepared as followed (Table, Table). For electrophoresis, working running buffer was mixed by 1 part 20 × MES SDS Running buffer or MOPS SDS Running buffer and 19 parts water.

Table 8. Preparation of 20 × MES SDS Running buffer.

Recipe for MES SDS Running buffer used for protein electrophoresis.

Reagent	**MES SDS Running buffer (20×)**
MES	97.6 g
Tris-Base	60.6 g
SDS	10.0 g
EDTA	3.0 g
Water	500 mL

Table 9. Preparation of 20 × MOPS SDS Running buffer.

Recipe for MOPS-based SDS Running buffer used for protein electrophoresis.

Reagent	**MOPS SDS Running buffer (20×)**
MOPS	104.6 g
Tris-Base	60.6 g
SDS	10.0 g
EDTA	3.0 g
Water	500 mL

NuPAGE electrophoresis system was used to perform protein electrophoresis. The NuPAGE gel with chosen polyacrylamide concentration was taken, rinsed by deionized waterand locked into place with the Gel Tension Wedge. 200 mL 1 × running buffer was poured into the upper buffer chamber and 600 mL into the lower buffer chamber. Protein samples were loaded into the wells and electrophoresis carried out using the following conditions (Table 10).

Table 10. Electrophoresis conditions for NuPAGE Bis-Tris gels.

Voltage and run time setting for protein separation using MES or MOPS running buffers.

Running buffer type	Voltage	Running time
MES SDS	200 V constant	35 mins
MOPS SDS	200 V constant	50 mins

2.4.3 Western blotting

After electrophoresis was completed, semi-wet blotting was performed to transfer proteins onto a polyvinylidene difluoride (PVDF) membrane using the XCell II blot module. 20 × NuPAGE transfer buffer and working transfer buffer were prepared as follows:

Table 11. Preparation of **20 × NuPAGE transfer buffer**

Composition of the stock transfer buffer used for semi-dry protein blotting

Reagent	**NuPAGE transfer buffer (20×)**
Bicine	10.2 g
Bis-Tris (free base)	13.1 g
EDTA	0.75 g
Water	125 mL

Table 12. Preparation of working transfer buffer.

Formulation of the final transfer buffer used for Western blotting, including antioxidant and methanol

Reagent	**Volume (mL)**
NuPAGE transfer buffer (20 ×)	50 mL
NuPAGE Antioxidant	1mL
Methanol	100 mL
Water	849 mL

The PVDF membrane was cut to meet the dimensions of the gel, and then pre-wetted in methanol for over 30s and rinsed by deionized water for further use. The trimmed gel was put on pre-soaked filter paper, and then covered by pre-soaked PVDF membrane followd by putting another pre-soaked filter paper on the top of the membrane, ensuring removing all trapped air bubbles. The soaked blotting pad was then moved into XCell II blot module. The transferring power condition was listed as follows:

Table 13. Membrane transfer protocol.

Conditions for semi-dry transfer of proteins from NuPAGE gels to PVDF membranes

Gel	**Transfer buffer**	**Membrane**	**Power**
MuPAGE Bis-Tris gel	1 × NuPAGE Transfer buffer with 10% methanol + 0.1% NuPAGE Antioxidant	PVDF	100 V constant for 1 hour

After the proteins were transferred on the PVDF membrane, the membrane was put into 5% skim milk diluted by Tris-buffered saline with 0.1% Tween 20 detergent (TBST) to prevent non-specific binding of antibodies for 2 hours at RT. The TBST was prepared as follows:

Table 14. Preparation of TBST working buffer.

Composition of Tris-buffered saline with Tween-20, used for membrane washing and antibody dilution

Reagent	**TBST (1×)**
Tris-HCl	2.42 g
NaCl	8.76 g
Tween-20	1 mL
Water	to 1000 mL

The membrane was incubated with relative primary antibodies for overnight. The primary antibodies were listed as follows:

Table 15. Primary antibodies used for Western blotting.

Lists of antibodies, their dilutions, and commercial sources of detecting OXPHOS complexes, SERCA2a, CPT1a, and α-tubulin.

Primary antibody	**Dilution**	**Company**
Total OXPHOS Antibody Cocktail antibody	1:250	Invitrogen (45-8099)
SERCA2a	1:5000	Abcam (ab150435)
CPT-1a	1:1000	Abcam (ab128568)
α-tubulin	1:10000	Abcam (ab7291)

After overnight incubation of primary antibodies, the membranes were washed by TBST buffer for 3 times (10 mins) followed by incubation of relative secondary antibodies for 2 hours at RT. The blots were exposed by ECL reagent and imaged through gel doc XR system. All images were imported into FIJI ImageJ software for the semi-quantification.

2.5 Mitochondrial Content

Heart samples were collected, and rinsed using cold ice HBSS, and homogenized in 200 μL DNA lysis buffer with 2 uL proteinase K (Stock concentration: 20 mg/mL) at 56°C for 2 hours (Table). Afterward, the lysate was mixed with equal volume of phenol:chloroform:isoamyl alcohol solution for over 30 s and then centrifuged at 12000 g for 10 mins at 4°C. The supernatant was collected in a new 1.5 mL tube with equal volume of 300 μL chloroform mixed vigorously for 30 s followed by centrifugation at 12000 g for 10 mins at 4°C. The upper aqueous phase was transferred into a new 2 mL tube and mixed with 2 volumes of ice-cold ethanol at -20°C for 1 hour. DNA pellet was collected after centrifugation at 12000 g for 10 mins. The DNA pellet was washed by 70% ethanol for twice and finally dried at RT for 10 mins. 50 uL Tris-EDTA (TE) buffer was added into the DNA pellet to resuspend the DNA. The concentration and purity of total DNA were measured by a NanoDrop spectrophotometer; a a A260/A280 ratio of c. 1.8 indicated DNA of suitable purity.

Table 16. Preparation of DNA lysis buffer.

Composition of the buffer used for genomic and mitochondrial DNA extraction from heart tissue

Reagent	**DNA lysis buffer (100 mL)**
Tris-HCl (1M, PH: 8.0)	1
EDTA (0.5M, PH: 8.0)	2
NaCl (5M)	2
SDS (10%)	5
Deionized Water	90

To evaluate the expression of mtDNA, ND1 and 16s rRNA were selected, while HK2 was used as a housekeeping reference gene. The Primer information was listed as follows (**Table 17**).

Table 17. qPCR Primers for mitochondrial and nuclear genes

Sequences of primers used to amplify ND1, 16s rRNA (mitochondrial), and HK2 (nuclear reference) genes

Gene	Primer	Sequence
ND1	Forward	5'-CAGCCTGACCCATAGCCATA-3'
	Reverse	5'-CGATGGTGAGAGCTAAGGTC-3'
16s rRNA	Forward	5'-CGTCTGGTAAAGGGTGCGTAG-3'
	Reverse	5'-AGGGTGACGGGCGGTGTGTA-3'
HK2	Forward	5'-AGCCACCACTCACCCTACT-3'
	Reverse	5'-CCAGGCATTCGGCAATGTG-3'

Total 20 μL qPCR reaction system for each sample was prepared in 96-well plate, and then mixed gently (Table). After sealing with optical adhesive film, the plate was inserted into a real-time PCR machine. The whole thermal cycling condition was programmed based on the primer and SYBR Green master mix (**Table 18**).

Table 18. qPCR reaction setup.

Components and volumes for each 20 **uL qPCR reaction using SYBR green chemistry**

Component (Total 20 uL)	**Volume (uL)**
SYBR Green Master Mix	10
Forward Primer	0.4
Reverse Primer	0.4
DNA	2
ddH2O	Up to 20

Table 19. qPCR thermal cycling conditions.

Temperature and time setting for amplification and melt curve analysis.

Step	**Temperature**	**Time**	**Cycles**
Initial denatureation	95°C	10 min	-
Denaturation	95°C	15 sec	40 cycles
Anneal/Extend	60°C	1 min	40 cycles
Melt curve analysis	72°C	35 sec	40 cycles

After the programme of Real-time PCR completed, the Ct value of each sample was exported for further analysis. ΔΔCt method was performed to semi-quantify the relative expression of ND1 or 16s rRNA compared to that of reference gene.

$$\Delta Ct = Ct_{\text{target}} - Ct_{\text{reference}}$$

$$\Delta\Delta Ct = \Delta Ct_{\text{sample}} - \Delta Ct_{\text{control}}$$

$$\text{Relative Expression} = 2^{-\Delta\Delta Ct}$$

2.6 Statistical analysis

In this study, all statistical analyses were performed by GraphPad Prism software (version 10.1). All the numerical values were presented as Mean ± standard deviation (SD). Prior to statistical testing, the normality of data distribution for each quantitative dataset was assessed using the Shapiro-Wilk test. A two-tailed unpaired Student's *t* test was performed to analyse the difference between two groups. The statistical difference was considered as P value < 0.05.

Chapter 3. RESULTS

3.1. Cardiac hypertrophy at early stage

This study employed the established HCM mouse model ACTC^{E99K}; to evaluate the cardiac hypertrophy in this model, HW/TL was determined at 10, 24 and 54 weeks in both ACTC^{NTG} and ACTC^{E99K}mice. ACTC^{NTG} mice had a slight, but not significant, increase in HW/TL from 10w- to 54w. In ACTC^{E99K} mice, HW/TL was gradually increased from 10-week to 54-week. HW/TL in ACTC^{E99K} mice had no difference at 10-week compared to that in ACTC^{NTG} mice, but there was a significant increase in HW/TL at 24-week and 54-weeks in ACTC^{E99K} mice (**Figure 5**). The result showed that ACTC^{E99K} heart weight was significantly increased compared to that in ACTC^{NTG} mice.

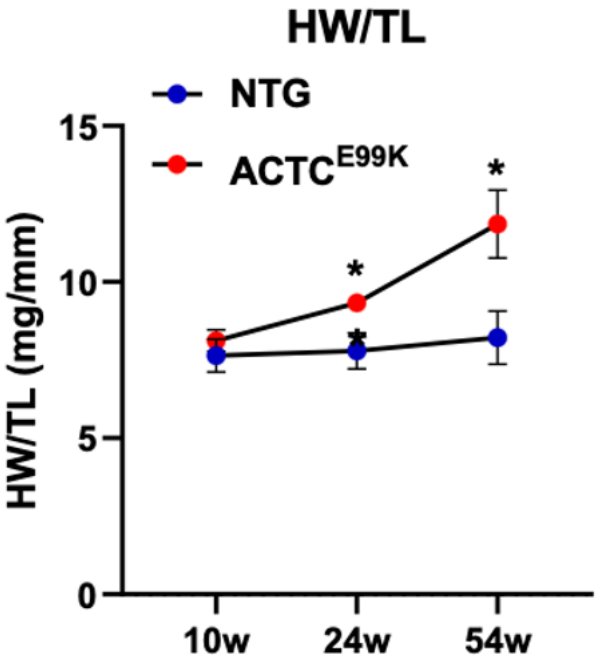

Figure 5. THE ACTC^{E99K} mutation induces progressive cardiac hypertrophy from 24 weeks of age. Quantitative analysis of cardiac hypertrophy assessed by the ratio of heart weight to tibia length (HW/TL) in ACTC^{E99K} and ACTC^{NTG} mice at 10-week, 24-week, and 54-week of age. $^{*}P$ value < 0.05. Data are presented as mean ± SD. While HW/TL was comparable between genotypes at the early 10-week time point, ACTC^{E99K} mice exhibited a significant and progressive increase in cardiac mass at 24 and 54 weeks. This result demonstrates a time-

dependent development of hypertrophy in this HCM model, with pathological growth becoming evident by mid-adulthood.

In addition, the size of myocytes in hearts in both ACTC^{E99K} mice and ACTC^{NTG} mice using WGA staining was measured. WGA is a lectin which binds glycoconjugates, and WGA staining has been established as a technique to quantify the size of cardiac myocytes in situ[108]. WGA staining of frozen heart slices of both ACTC^{E99K} and ACTC^{NTG} mice indicated that enlarged cardiomyocyte cross-sectional areas (CSA) were found in ACTC^{E99K} group compared to ACTC^{NTG} mice at 24-week (**Figure 6**). Thus, the ACTC^{E99K} mutation leads to obvious myocyte hypertrophy at 24-week.

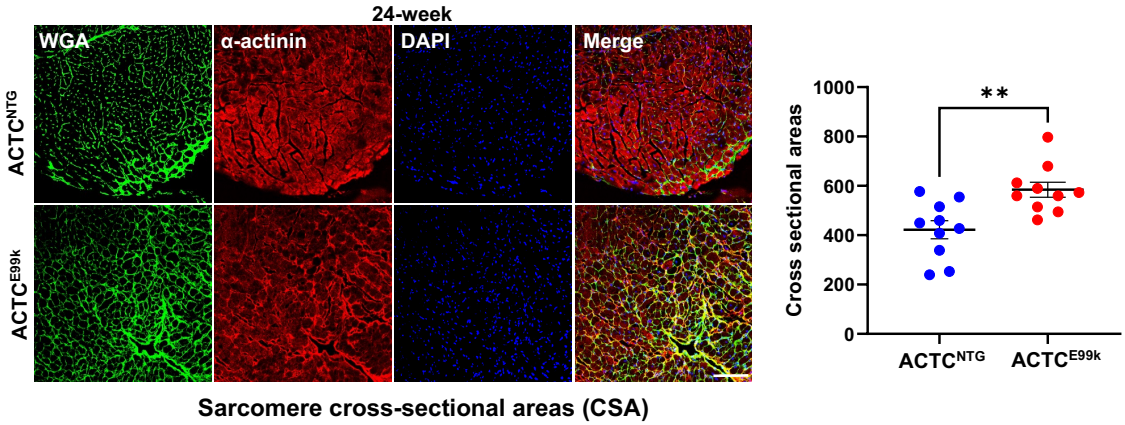

Figure 6. Hypertrophic remodeling at the cellular level of ACTC^{E99K} mice. (**Left**) Representative confocal microscopy images of left ventricular sections from 24-week-old ACTC^{E99K} and ACTC^{NTG} mice stained with Wheat Germ Agglutinin (WGA, green) to outline cell membranes, anti-α-actinin (red) to stain sarcomeres, and DAPI (blue) for nuclei. Scale bar, 100 μm. (**Right**) Quantitative analysis of cardiomyocyte cross-sectional area (CSA) derived from WGA staining. ACTC^{E99K} cardiomyocytes displayed a significantly enlarged CSA compared to ACTC^{NTG} controls, confirming that the observed increase in whole-heart mass is driven, at least in part, by the hypertrophy of individual cardiac muscle cells.

3.2 Accelerated fibrotic accumulation

To semi-quantify cardiac fibrosis, Sirius Red staining was performed in both ACTC^{NTG} mice and ACTC^{E99K} mice. This showed significant fibrotic accumulation at the apex of ACTC^{E99K}

mice at 24-week, while almost no obvious fibrotic staining was found in any area of ACTC^{NTG} mice (**Figure 7**).

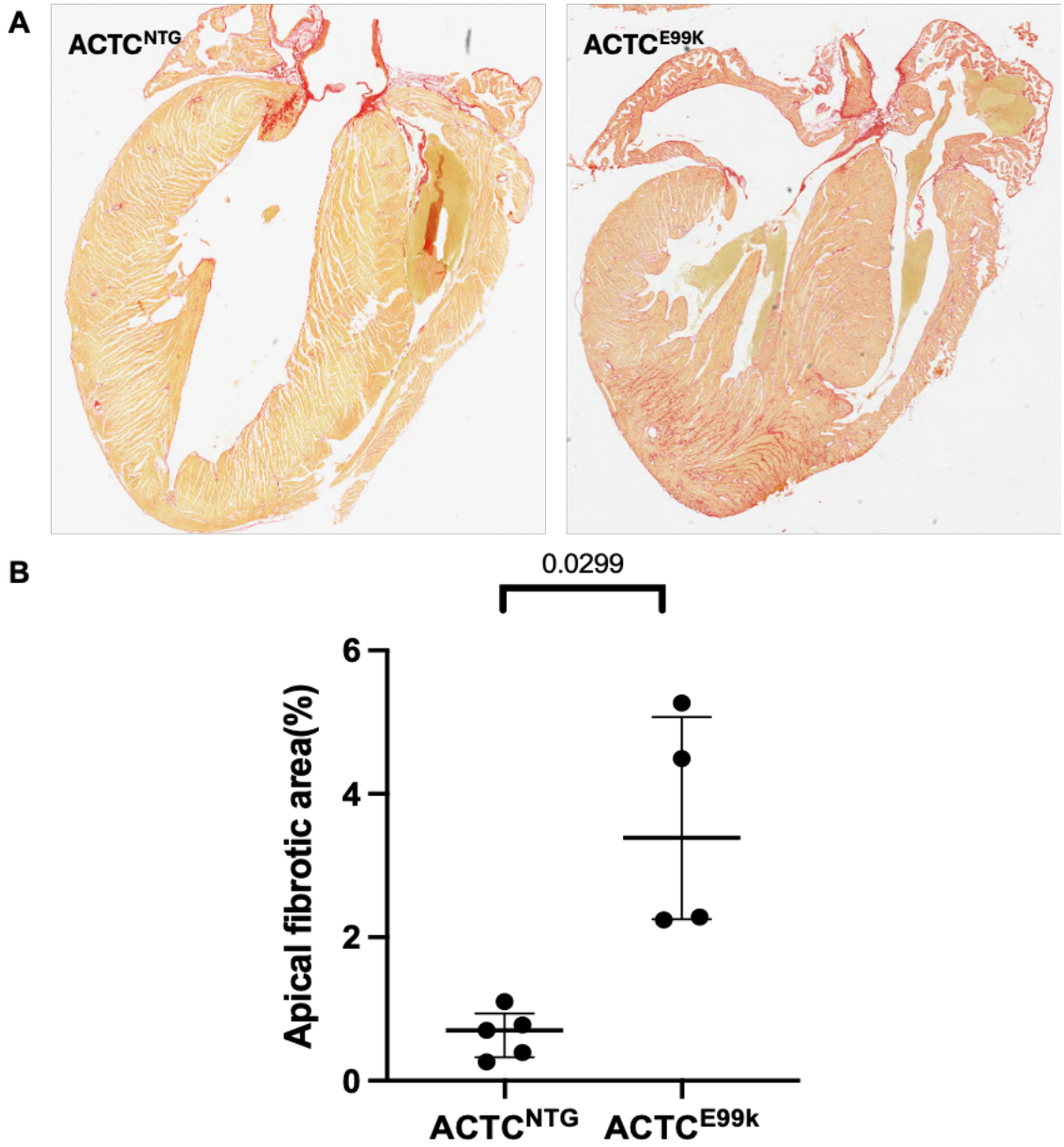

Figure 7. The ACTC^{E99K} heart exhibits accelerated and localized fibrotic deposition. (A) Representative photomicrographs of left ventricular sections from 24-week-old ACTC^{NTG} and ACTC^{E99K} mice stained with picrosirius red, which specifically stains collagen fibers in red, allowing for visualization of fibrotic areas. (B) Semi-quantitative analysis of the percentage of fibrotic area within the left ventricle. Data are presented as mean ± SD. ACTC^{E99K} hearts showed significant collagen accumulation, particularly prominent in the apical region, while ACTC^{NTG} hearts displayed minimal staining. This demonstrates that the mutation promotes

aggressive extracellular matrix remodeling and fibrosis, a hallmark of adverse cardiac remodeling in HCM.

3.3. Abnormal cardiac contractile function

Previously, the ACTC^{E99K} mouse model was found to exhibit cardiac contractile dysfunction with increased end-diastolic volume and end-diastolic pressure, and reduced relaxation rates compared with ACTC^{NTG} mice [35]. To examine the extent of cardiac contractile dysfunction of the ACTC^{E99K} mice in Oxford, the cardiac contractile performance of ACTC^{E99K} and ACTC^{NTG} mice was examined using echocardiography. LVEF was determined at three different time-points,10, 24, and 54-weeks. No difference was found among the different time-points in ACTC^{NTG} mice. However, 10-week and 24-week LVEF value of ACTC^{E99K} mice was significant reduced compared to that of ACTC^{NTG} mice. At 54-week, the EF value was below 60% at ACTC^{E99K} mice (**Figure 8**).

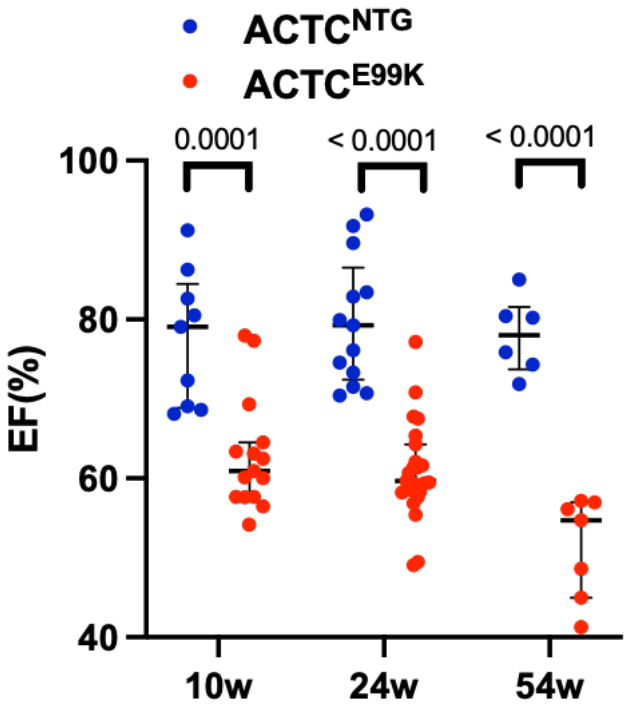

Figure 8. Early-onset and progressive contractile dysfunction in ACTC^{E99K} mice. Serial assessment of cardiac systolic function by transthoracic echocardiography. Left ventricular ejection fraction (LVEF) was measured in ACTC^{E99K} and ACTC^{NTG} mice at 10-week, 24-week,

and 54-week. Data are presented as mean ± SD. $ACTC^{NTG}$ mice maintained stable LVEF across all time points. In contrast, $ACTC^{E99K}$ exhibited a significant reduction in LVEF as early as 10-week, which progressed over time, with values falling below 60% by 54 weeks of age. This timeline revealed that contractile impairment precedes the full manifestation of hypertrophic and worsens with disease progression, indicating a direct impact of the mutation on cardiac pump function.

3.4. Differentiated expressed genes based on the transcriptome data

In the above work, I have verified that the $ACTC^{E99K}$ mutation leads to cardiac hypertrophy with typical cardiac fibrosis at the apex, and contractile dysfunction. The details of the whole process leading to this pathophysiological remodelling and dysfunction remains unclear. Thus, I performed bulk RNA sequencing and analysed the differences in expression at the transcriptional levels. Ventricular tissues were collected both groups at 10-, 24- or 60-week timepoints. Total RNA was extracted and sequenced to obtain transcriptome data through bulk RNA sequencing. In my analysis, 2682, 4787, and 10445 DEGs were identified between $ACTC^{E99K}$ and $ACTC^{NTG}$ mice at 10-, 24- and 60-week (**Figures 9-11**).

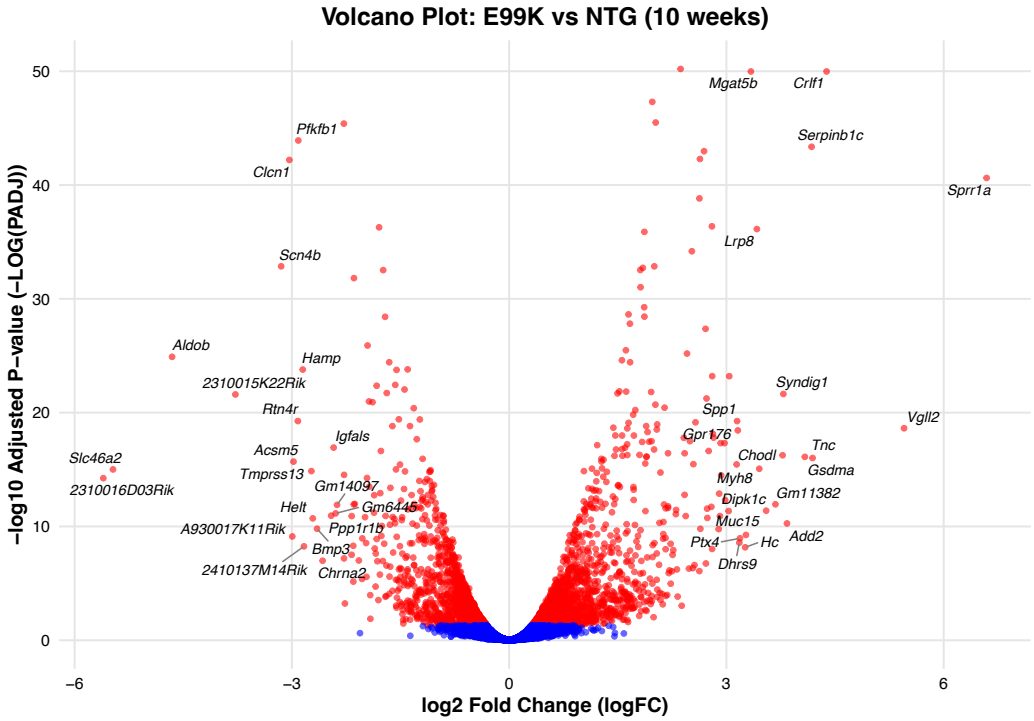

Figure 9. Early transcriptional alterations in ACTC^{E99K} hearts at 10 weeks revealed by volcano plot. Volcano plot visualizing the differential gene expression analysis between ACTC^{E99K} and ACTC^{NTG} ventricular tissues at the 10-week time point (n=3-4 biological replicates per group). Each data pointon the plot represents a single gene. The x-axis shows the log2 fold-change in gene expression (ACTC[E99K] vs. ACTC[NTG]), where values greater than 0 indicate upregulation and values less than 0 indicate downregulation in the mutant. The y-axis represents the statistical significance of the change, plotted as -log10(adjusted P-value). The grey points denote genes with no significant change. The red points highlight statistically significant differentially expressed genes (DEGs), defined by an adjusted P-value < 0.05 and an absolute log2 fold-change > 1 (dashed vertical lines). A total of 2,682 DEGs were identified at this early stage, with a notable number of significantly downregulated genes, indicating widespread transcriptional dysregulation precedes overt histological hypertrophy.

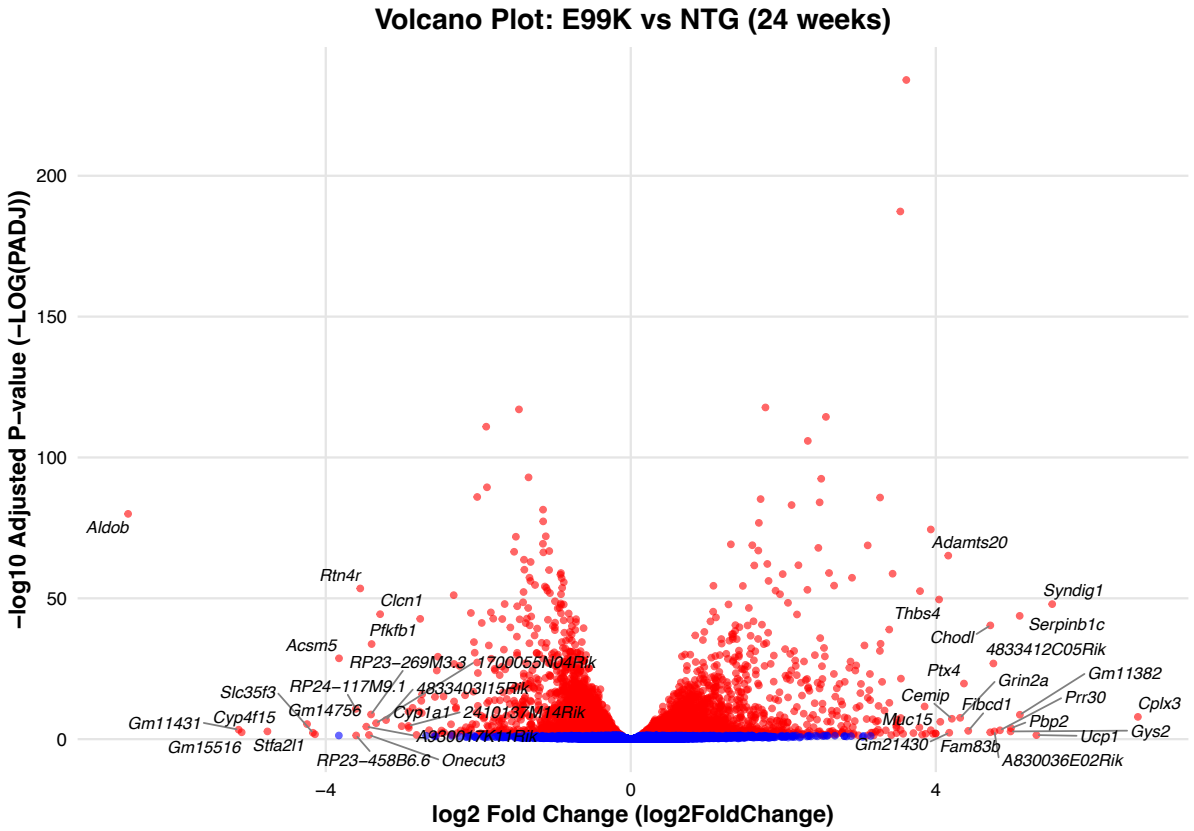

Figure 10. Escalation of transcriptomic dysregulation in ACTC^{E99K} hearts at 24 weeks. Volcano plot displaying the results of differential expression analysis from RNA-seq of ventricular tissues at 24 weeks of age (n =3-4 per group). Significantly upregulated genes (adjusted P-value < 0.05 and log2 fold-change > 1) and downregulated genes (adjusted P-value < 0.05 and log2 fold-change < -1) are shown in red. The number of significant DEGs substantially increased to 4787 at this time point compared to 10 weeks, reflecting a marked expansion of transcriptional perturbations as the disease phenotype matures. The distribution shows a broad spectrum of both upregulated and downregulated genes, encompassing pathways critical to metabolism, fibrosis, and sarcomere function, coinciding with the period of established cardiac hypertrophy and fibrosis observed histologically.

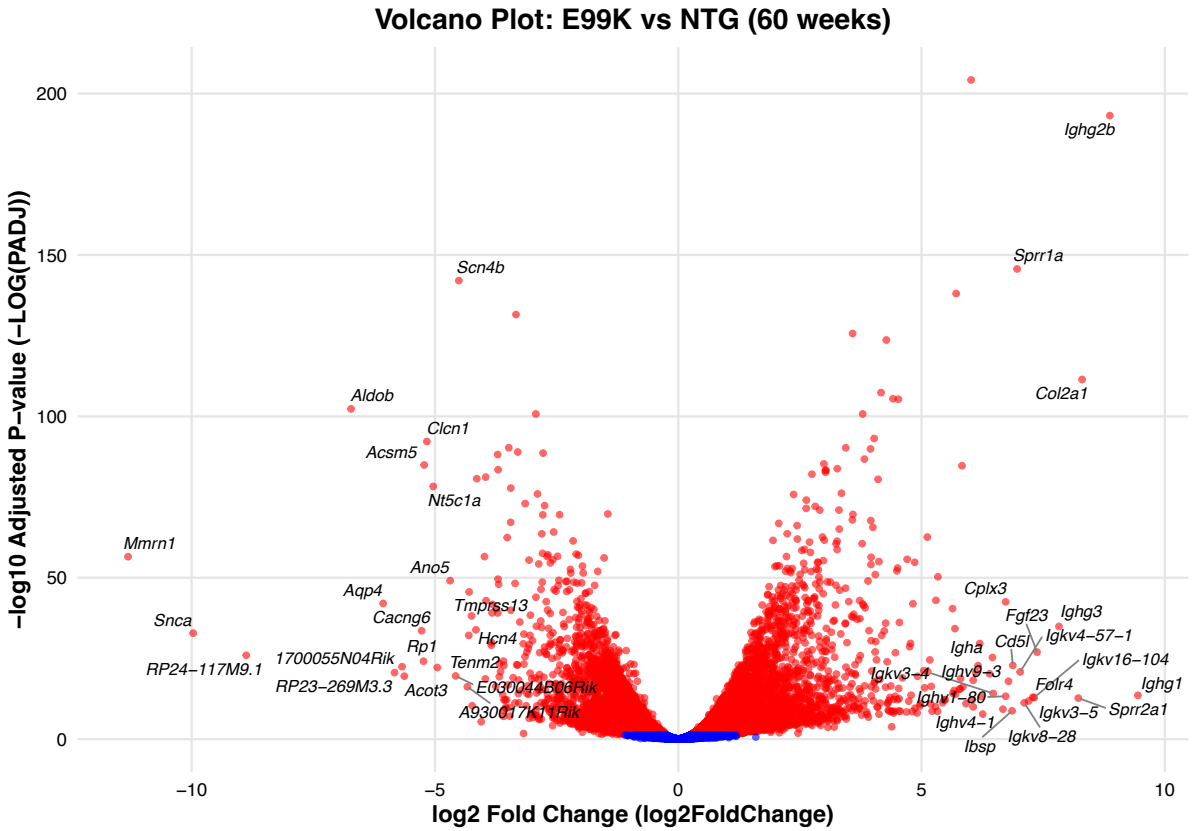

Figure 11. Profound global transcriptomic remodeling in end-stage ACTC^{E99K} hearts at 60 weeks. Volcano plot illustrating the extensive differential gene expression profile in ACTC^{E99K} versus ACTC^{NTG} ventricles at the late 60-week time point (n = 3-4 per group). The analysis identified a striking total of 10,445 DEGs (red point), underscoring the massive scale of significantly upregulated genes, many with large fold-changes. This pattern is consistent with a robust activation of immune and inflammatory response pathways, as well as exensive extracellular matrix remodeling, which dominates the transcriptomic landscape of the terminally failing HCM heart. The sheer number of DEGs highlights the complexity and progression of the molecular pathophysiology in this model.

I have listed the top 20 upregulated or downregulated genes respectively at 10-, 24- and 60-week (Table 20). There were three genes - Aldob, Acsm5 and A930017K11Rik - that were downregulated at all three timepoints, but no gene upregulated at all timepoints. Aldob encodes aldolase B and Acsm5 encodes Acyl-CoA Synthetase Medium-Chain Family Member 5, which is both involved in metabolic pathways.

Table 20. Top 20 upregulated and downregulated DEGs at 10-, 24-, and 60-weeks.

Lists of the most significantly altered genes in ACTC^{E99K} hearts compared to ACTC^{NTG} across three time points

Downregulated			Up regulated		
10-week	**24-week**	**60-week**	**10-week**	**24-week**	**60-week**
Aldob	Aldob	Aldob	Sprr1a	Cplx3	Ighg1
Acsm5	Acsm5	Acsm5	Vgll2	Ighg3	Ighg2b
A930017K11Rik	A930017K11Rik	A930017K11Rik	Crlf1	Syndig1	Col2a1
2310015K22Rik	Gm14165	Mmrn1	Gsdma	Ucp1	Sprr2a1
Scn4b	Tmem181b-ps	Aqp4	Serpinb1c	Gm11382	Ighg3
Clcn1	Cyp4f15	RP23-269M3.3	Tnc	Serpinb1c	Fgf23
2310016D03Rik	Gm14756	1700055N04Rik	Add2	Pbp2	Igkv16-104
Slc46a2	Slc35f3	Acot3	Syndig1	Gys2	Folr4
Rtn4r	Stfa2l1	Cacng6	Chodl	Prr30	Igkv3-5
Pfkfb1	Mrgpra2b	Rp1	Gm11382	A830036E02Rik	Igkv8-28
Hamp	Gm11431	Snca	Dipk1c	4833412C05Rik	Igkv4-57-1
2410137M14Rik	RP24-117M9.1	Clcn1	Myh8	Chodl	Sprr1a
Tmprss13	RP23-458B6.6	Nt5c1a	Lrp8	Fam83b	Cd5l
Helt	Gm9625	Tenm2	Mgat5b	Fibcd1	Ibsp
Bmp3	Rtn4r	Ano5	Muc15	Ptx4	Ighv9-3
Chrna2	Gm15516	E030044B06Rik	Hc	Grin2a	Ighv1-80
Ppp1r1b	Onecut3	Scn4b	Ptx4	Cemip	Cplx3
Igfals	RP23-269M3.3	RP24-117M9.1	Dhrs9	Gm21430	Ighv4-1
Gm6445	Pfkfb1	Hcn4	Gpr176	Adamts20	Igkv3-4
Gm14097	RP23-52N17.1	Tmprss13	Spp1	Muc15	Igha

3.5. GO analysis based on the transcriptome data

In addition, GO enrichment analysis was performed on the data from all three timepoints to identify the significant pathways involved in biological processes, cell components, and molecular functions. For the cell components categories, at 10-, 24- and 60-week, collagen-containing extracellular matrix, mitochondrial matrix, and mitochondrial protein-containing complex were all upregulated in ACTC^{E99K} (**Figures 12-14**).

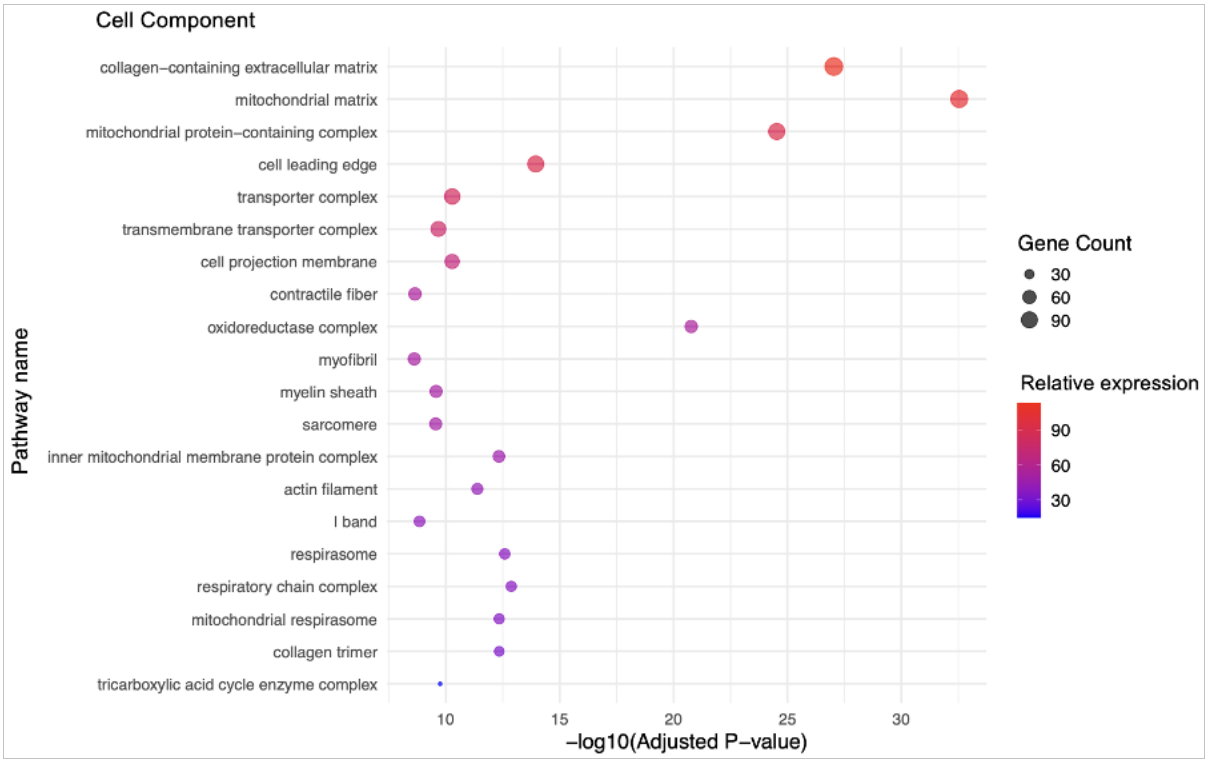

Figure 12. Gene Ontology (GO) Enrichment Analysis (Cell Component) in ACTC^{E99K} and ACTC^{NTG} mice at 10 weeks. Bubble chart displaying significantly enriched cellular components from GO analysis of DEGs at 10 weeks. Each bubble represents a GO term. The size of the bubble corresponds to the number of genes enriched in that term (Gene Count). The colour of the bubble indicates the relative expression level of the genes in that term within ACTC^{E99K} group compared to ACTC^{NTG} NTG (colour scale from low to high). Early alterations in mitochondrial components and collagen-containing extracellular matrix are evident, indicating initial stages of metabolic and structural remodelling.

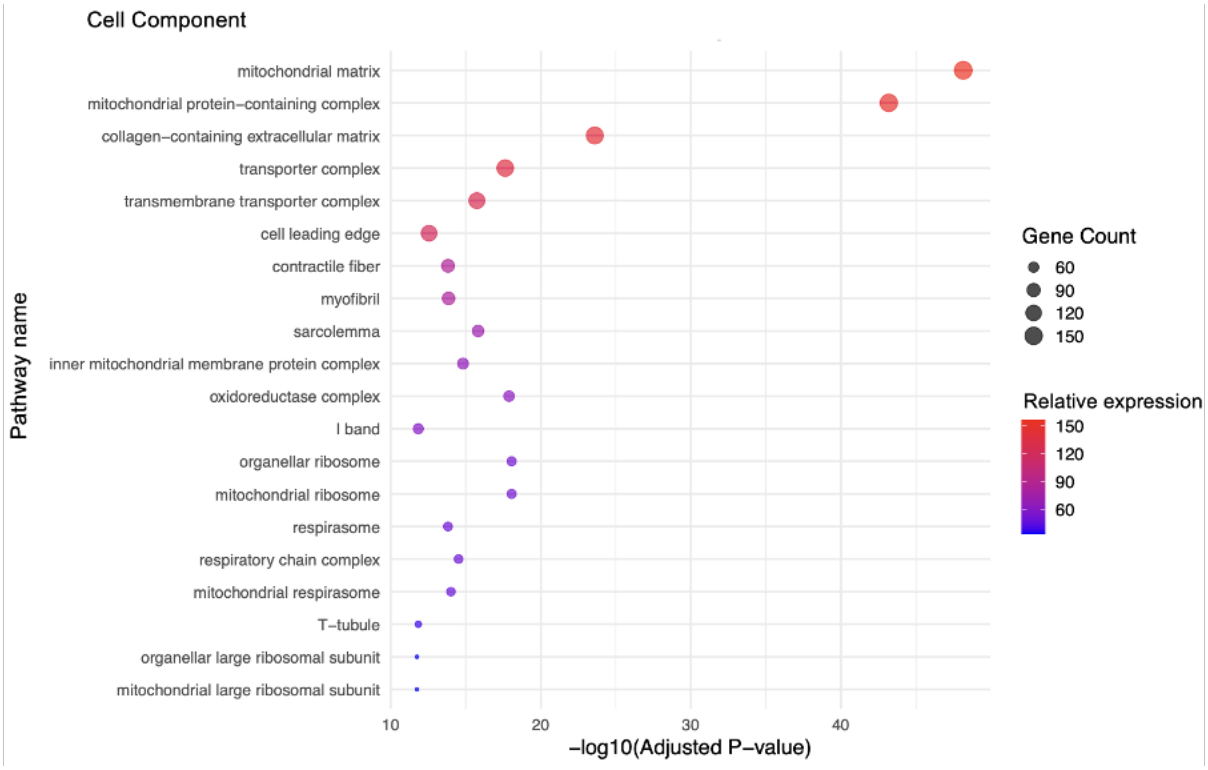

Figure 13. Gene Ontology (GO) Enrichment Analysis (Cell Component) in ACTC^{E99K} and ACTC^{NTG} mice at 24 weeks. Bubble chart of enriched cellular components from GO analysis at 24 weeks. Bubble size represents the number of genes (Gene Count) mapped to each term. Bubble colour represents the relative expression level. Pathway related to mitochondria and the extracellular matrix remain prominently enriched, reinforcing their central role in the pathophysiology of HCM at this progressive stage.

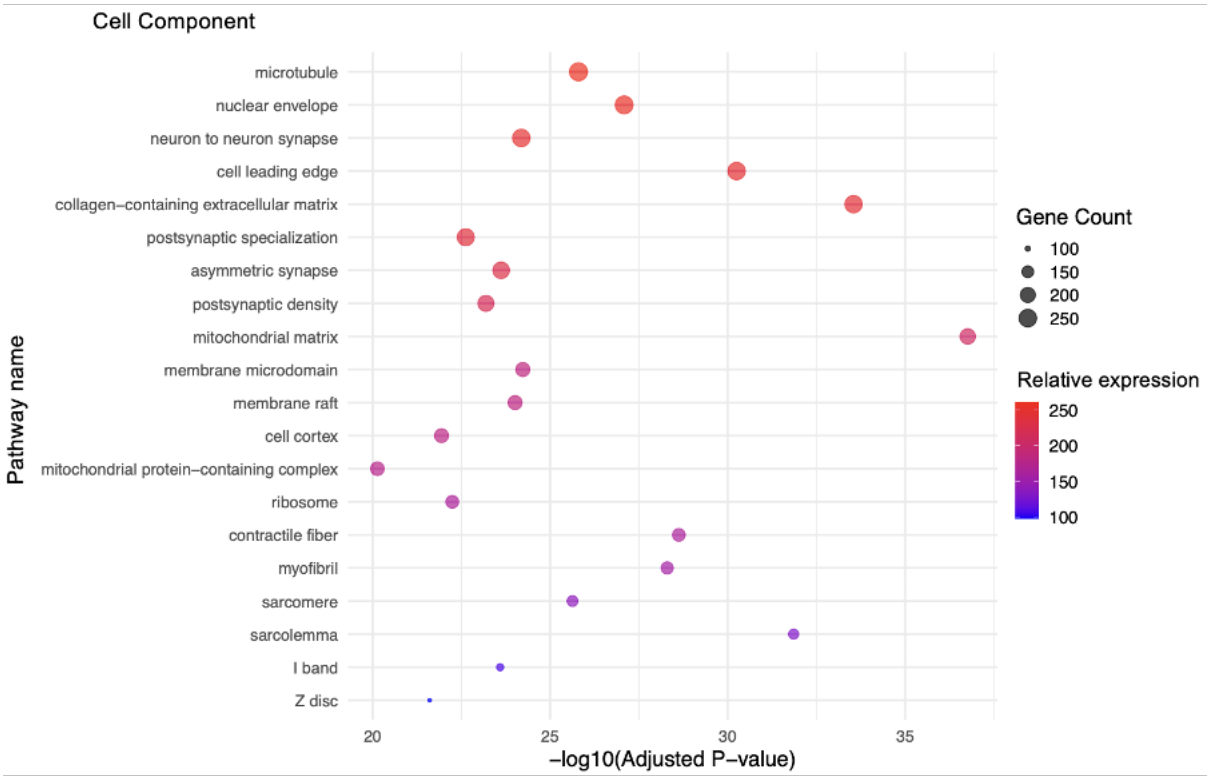

Figure 14. Gene Ontology (GO) Enrichment Analysis (Cell Component) in ACTC^{E99K} and ACTC^{NTG} mice at 60 weeks. Bubble chart showing enriched cellular components at the late 60-week timepoint. Bubble size indicates Gene Count, bubble colour indicates relative expression. Alongside persistent mitochondrial and extracellular matrix (ECM) terms, significant enrichment in neuronal-related components is observed, suggesting potential alterations in cardiac innervation during advanced disease progression.

In addition, under my GO analysis based on the bulk RNA sequencing, all the genes involved in the molecular function categories were assessed. Genes related to actin binding were affected significantly at all time-points (**Figures 15-17**). At 24- and 60-week, the nucleoside-triphosphatase regulator activity differed between ACTC^{E99K} mice and ACTC^{NTG} mice, while this activity was not identified at 10-week.

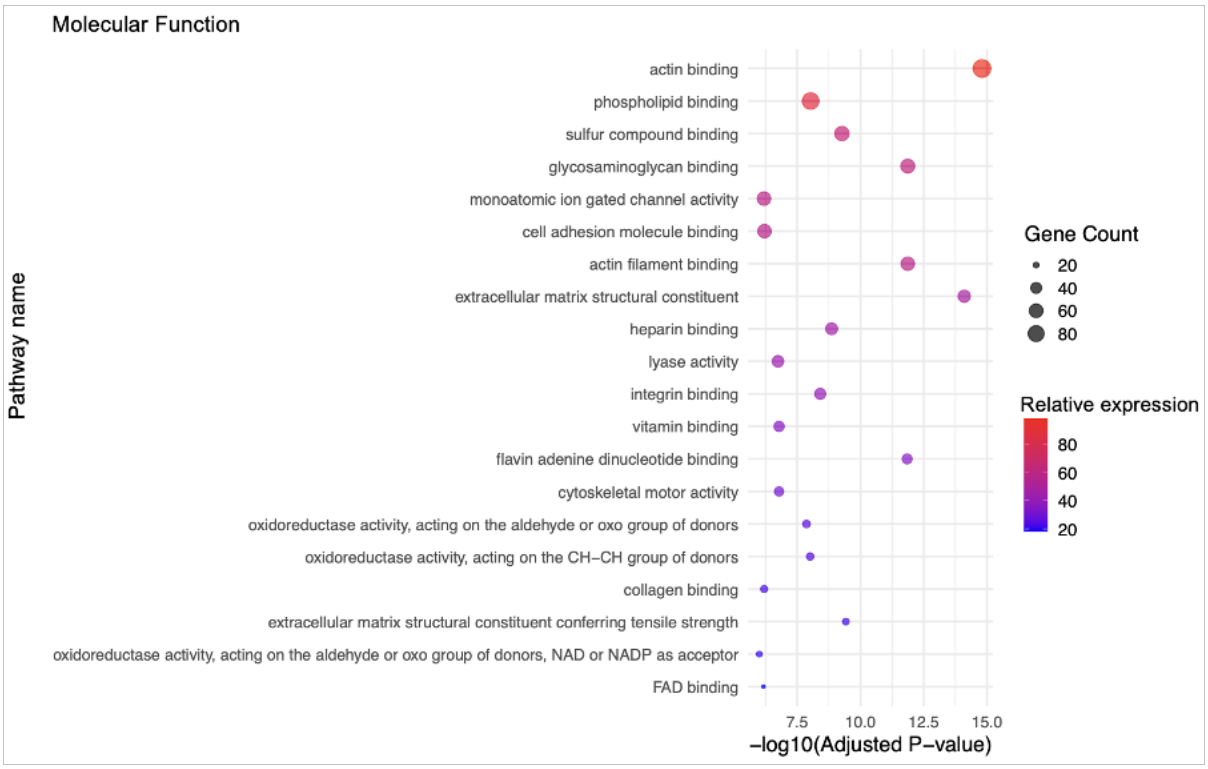

Figure 15. Gene Ontology (GO) Enrichment Analysis (Molecular Function) in ACTC^{E99K} and ACTC^{NTG} mice at 10 weeks. Bubble chart illustrating significantly enriched molecular function of DEGs at 10 weeks. Bubble size corresponds to the number of genes in the term (Gene Count). Bubble colour corresponds to the relative expression level. Early changes in "oxidoreductase activity" and "actin binding" hint at initial metabolic disturbances and direct impacts on the sarcomeric apparatus.

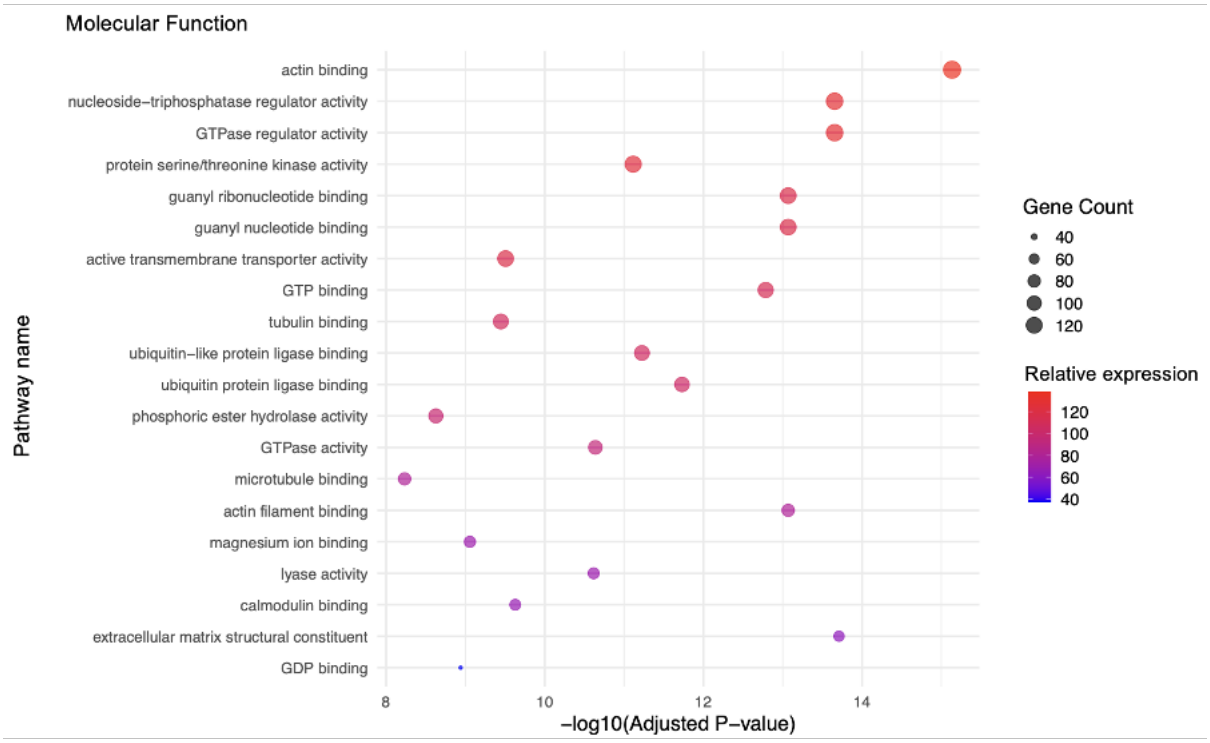

Figure 16. Gene Ontology (GO) Enrichment Analysis (Molecular Function) in ACTC^{E99K} and ACTC^{NTG} mice at 24 weeks. The size of the dot represents the Gene Count for each term. The colour of the dot represents the relative expression level. The spectrum of affected functions broadens, now including "nucleoside-triphosphatase regulator activity", which is crucial for the function of ATP-dependent motors and enzymes like myosin and mitochondrial complexes.

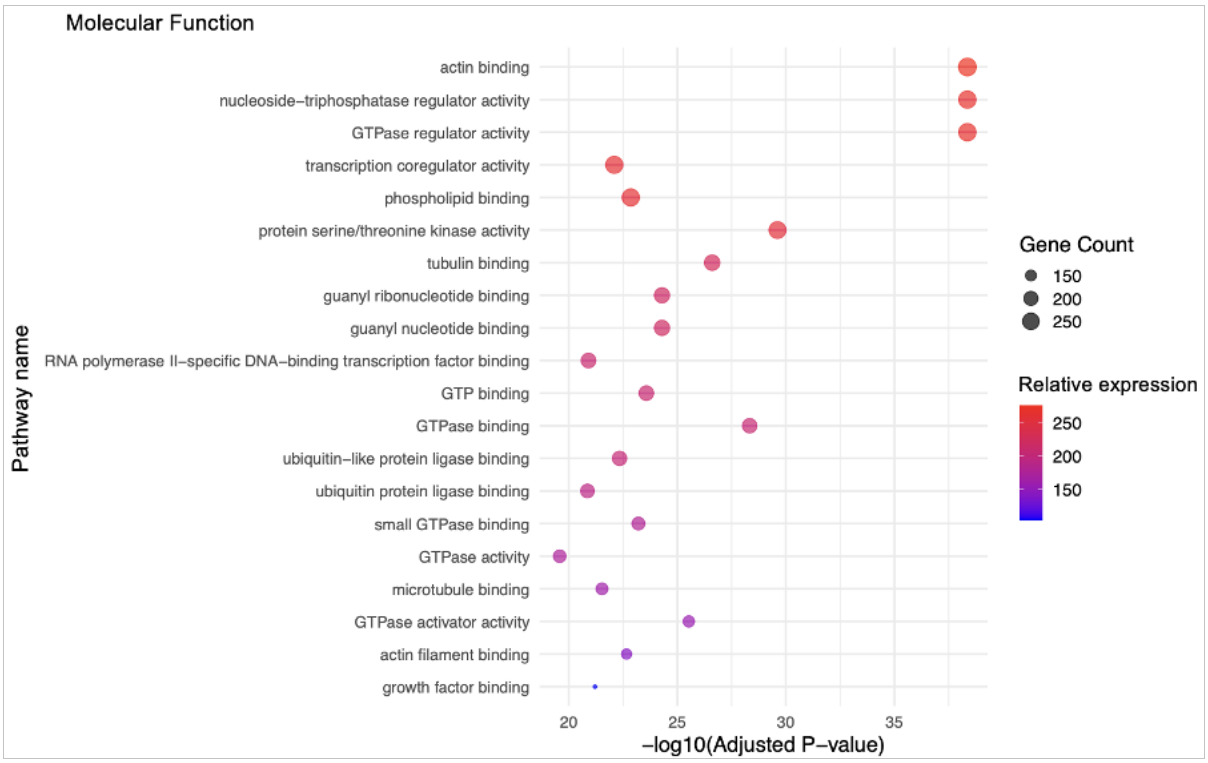

Figure 17. Gene Ontology (GO) Enrichment Analysis (Molecular Function) in ACTC^{E99K} and ACTC^{NTG} mice at 24 weeks. Dot size represents the number of genes associated with each term (Gene Count). Dot colour represents the relative expression level. The analysis reveals a complex landscape of functional alterations, including continued effects on cytoskeletal binding and energy-related enzyme activities in the terminally remodelled heart.

To understand the potential biological processes involved in the ACTC^{E99K} mutation induced HCM, I screened out differentiated biological processes between ACTC^{E99K} and ACTC^{NTG} group under GO analysis. I found there were significant metabolic processes changing between ACTC^{E99K} mice and ACTC^{NTG} mice but at 60-week, several processes including immune response or muscle cell differentiation related genes expressed significant difference between ACTC^{E99K} mice and ACTC^{NTG} mice (**Figure 18-20**).

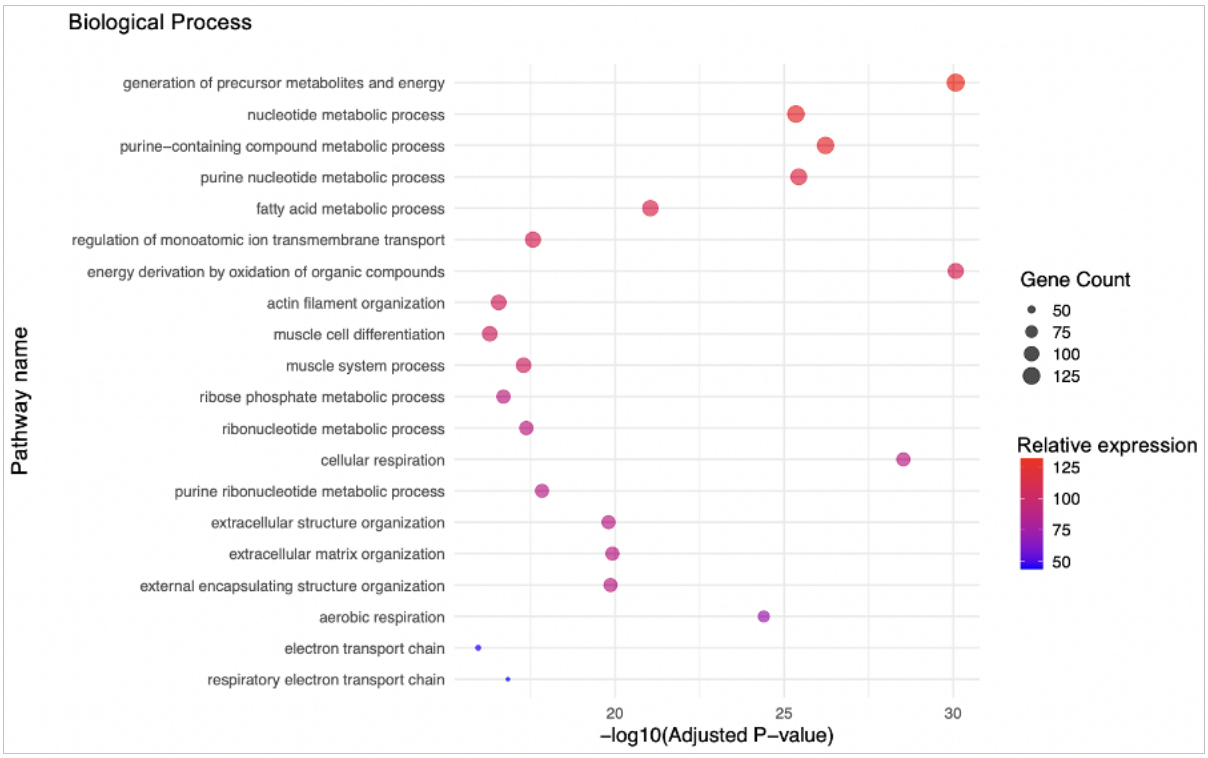

Figure 18. Gene Ontology (GO) Enrichment Analysis (Biological Process) in ACTC^{E99K} and ACTC^{NTG} mice at 10 weeks. Bubble chart showcasing significantly enriched biological processes at the 10-week timepoint. Bubble size indicates the number of genes enriched in each term (Gene Count). Bubble colour indicates the relative expression level. Processes related to energy generation ("generation of precursor metabolites and energy", "electron transport chain") and muscle function ("muscle system processes") are prominently downregulated, indicating an early and fundamental shift in the heart's energy generation and utilization.

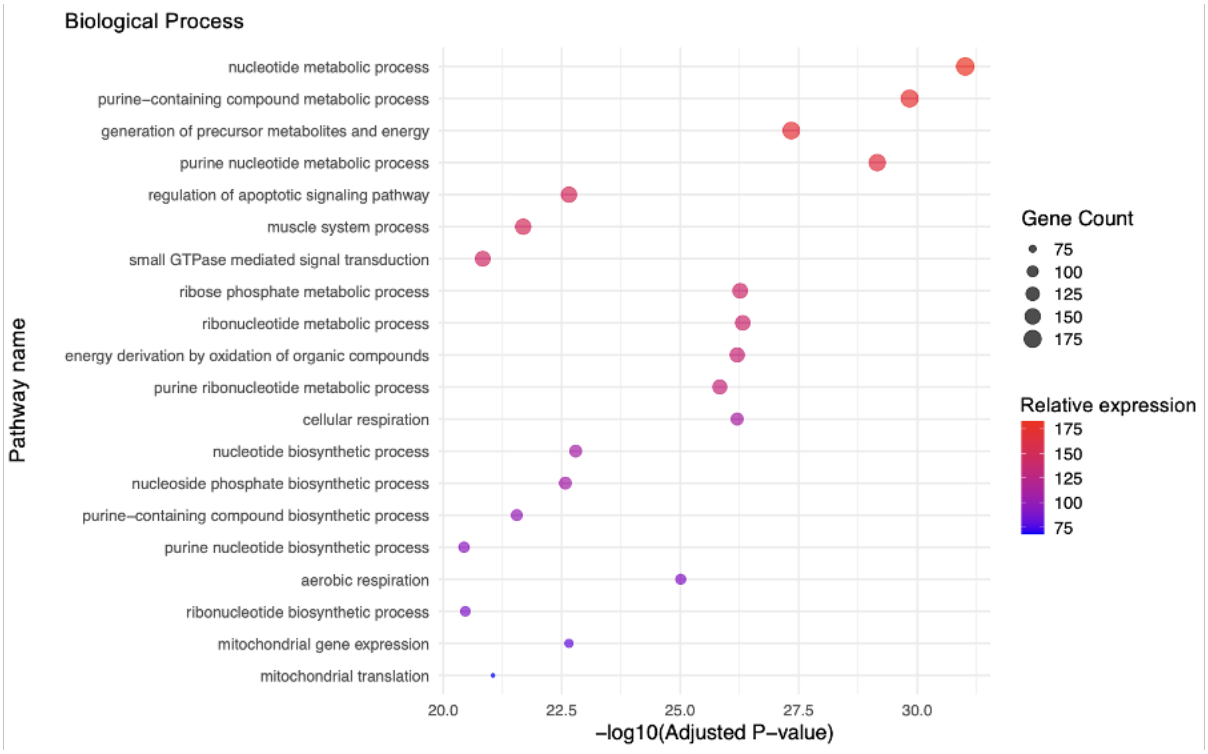

Figure 19. Gene Ontology (GO) Enrichment Analysis (Biological Process) in ACTC^{E99K} and ACTC^{NTG} mice at 24 weeks. Bubble chart of enriched biological processes at 24 weeks. The size of the bubble corresponds to the Gene Count. The colour of the bubble corresponds to the relative expression level. The enrichement of metabolic and nucleotide biosynthetic processes persists, while terms related to "extracellular matrix organization" become significant, correlating with the histologically observed fibrosis at this stage.

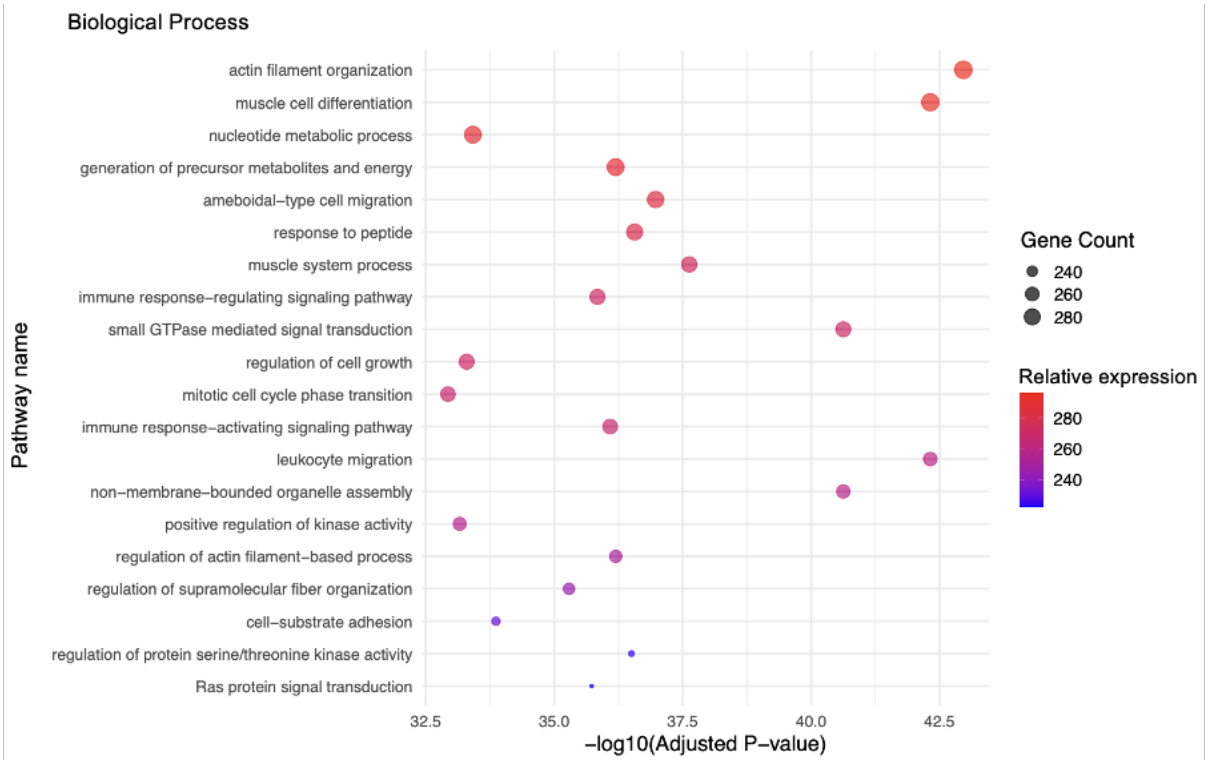

Figure 20. Gene Ontology (GO) Enrichment Analysis (Biological Process) in ACTC^{E99K} and ACTC^{NTG} mice at 60 weeks. Bubble size represents the Gene Count for each pathway. Bubble colour represents the relative expression level. A notable shift is observed, with strong enrichment of immune and inflammatory response pathways, suggesting a prominent role of the immune system in the late-stage remodelling process.

3.6. KEGG analysis based on the transcriptome data

Finally, I performed KEGG analysis to investigated whether the DEGs can be enriched to specific pathways participating the pathophysiological process of ACTC^{E99K} induced HCM. The results showed that at 10- and 24-week, the DEGs were enriched in the pathways of neurodegeneration, Alzheimer disease and amyotrophic lateral sclerosis, but at 60-week, the DEGs were additional enriched in the mitogen-activated protein kinase (MAPK) signalling pathway (**Figure 21-23**).

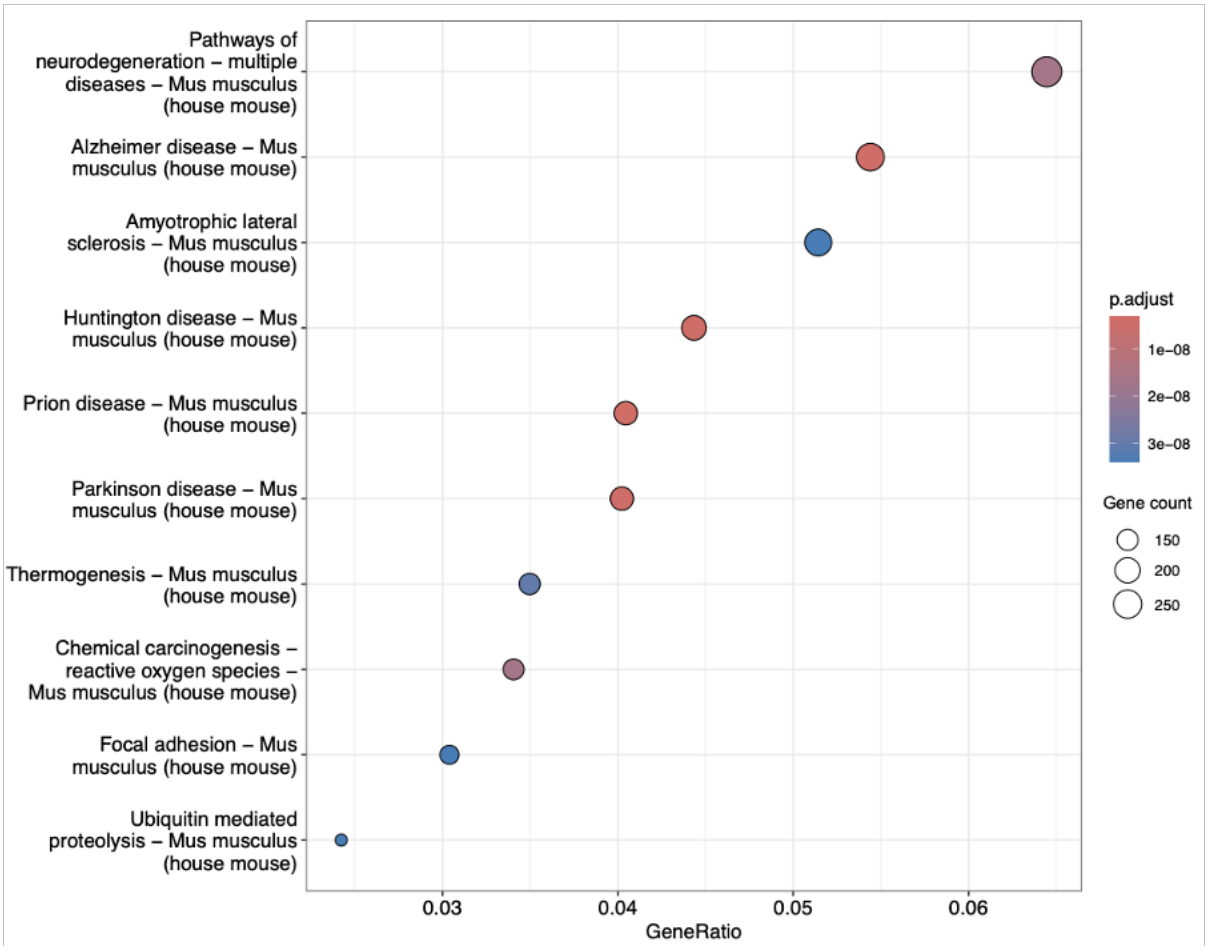

Figure 21. Kyoto Encyclopedia of Genes and Genomes (KEGG) Pathway Enrichment Analysis in ACTC^{E99K} and ACTC^{NTG} mice at 10 weeks. Bar plot of significantly enriched KEGG pathways based on DEGs at 10 weeks. The length of the bar represents the Gene Ratio (proportion of DEGs mapped to the pathway). The colour of the bar corresponds to the statistical significance (-log10(Adjusted P-value)), as shown in the legend (p.adjust). Pathway such as "Neurodegeneration" and "Alzheimer disease" are enriched, which may share underlying mechanisms like oxidative stress or proteostatic dysfunction with cardiac pathology.

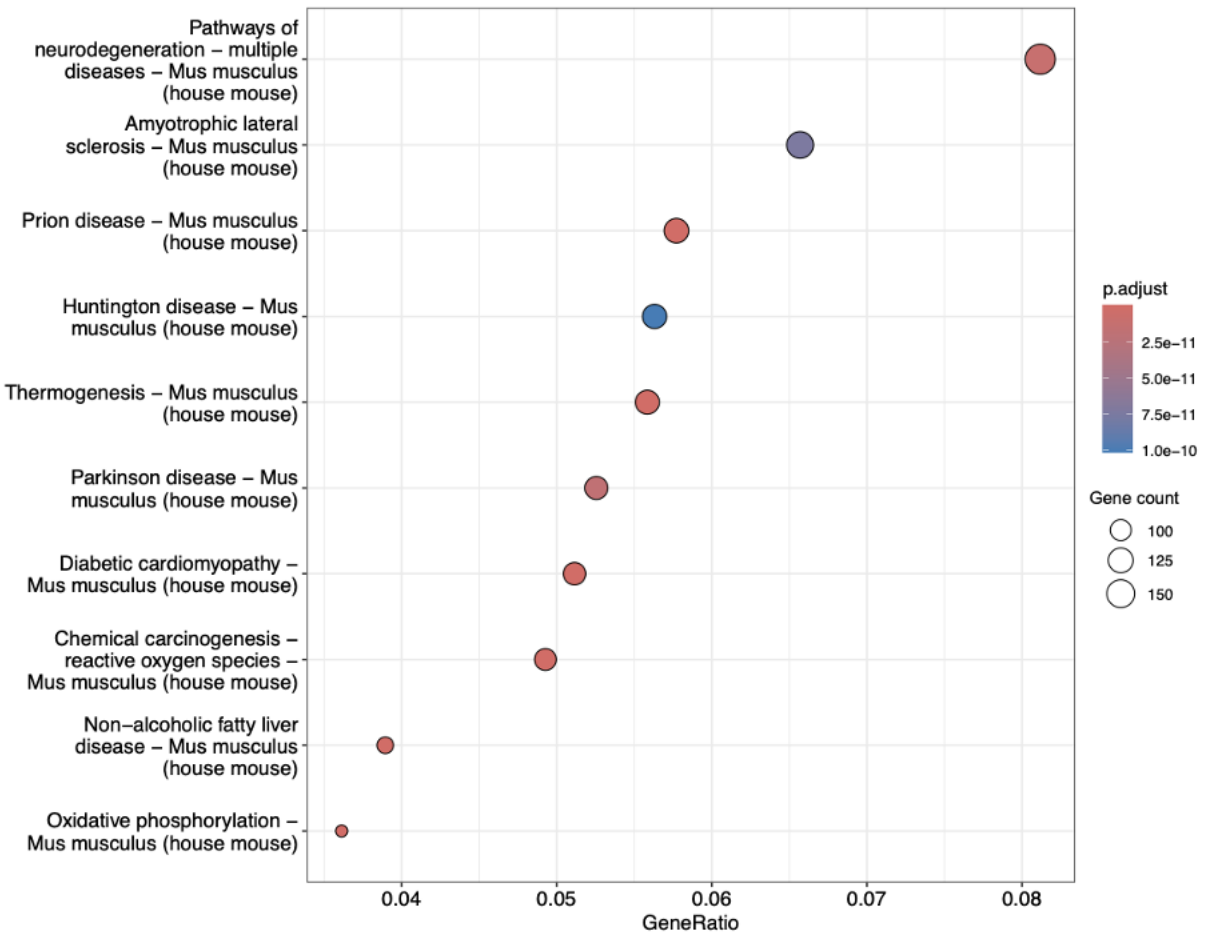

Figure 22. Kyoto Encyclopedia of Genes and Genomes (KEGG) Pathway Enrichment Analysis in ACTC^{E99K} and ACTC^{NTG} mice at 24 weeks. Bar plot showing enriched KEGG pathways at 24 weeks. The x-axis represents the Gene Ratio. The colour gradient of the bars represents the adjusted P-value (p.adjust), with more significant terms shown in darker shades. The size of the circles overlaid on the bars represents the number of genes (Gene Count) in each term. The persistence of neurodegeneration-related pathways alongside the emergence of terms like "Diabetic cardiomyopathy" reflects the ongoing and multifaceted cellular stress response.

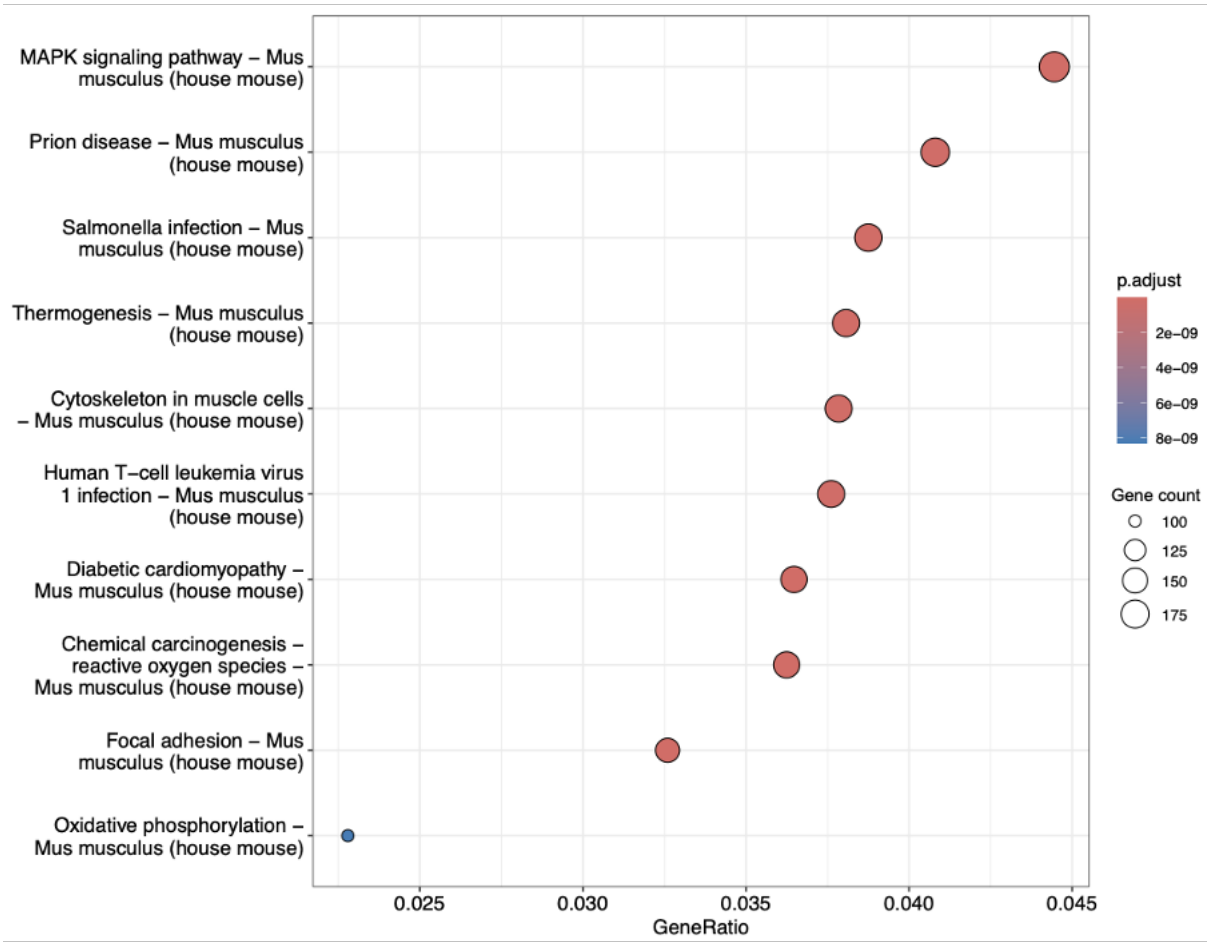

Figure 23. Kyoto Encyclopedia of Genes and Genomes (KEGG) Pathway Enrichment Analysis in ACTC^{E99K} and ACTC^{NTG} mice at 60 weeks. Bar plot of enriched KEGG pathways at 60 weeks. The x-axis shows the Gene Ratio. Bar colour indicates the statistical significance (-log10(adjusted P-value)). The size of the superimposed circles represents the number of DEGs (Gene Count) enriched in each pathway. A critical finding is the significant enrichment of the "MAPK signalling pathway", a key regulator of cell growth, hypertrophy, and stress response, highlighting its potential role in advanced HCM pathogenesis.

3.7. Differentiated expression of electron transport chain-related genes

To investigate whether there are changes to the energetics pathways in the ACTC^{E99K} at the transcript level, comparison of genes related to the electron transport chain (ETC) was performed between the ACTC^{E99K} and ACTC^{NTG} groups at 10- and 24- week respectively. At 10 weeks, a series of genes involved in Complexes I to V of the ETC were downregulated in the ACTC^{E99K} group, with similar results observed at 24 weeks (**Figure 24-25**). These results suggested that ACTC^{E99K} mutation may induce energetic dysfunction.

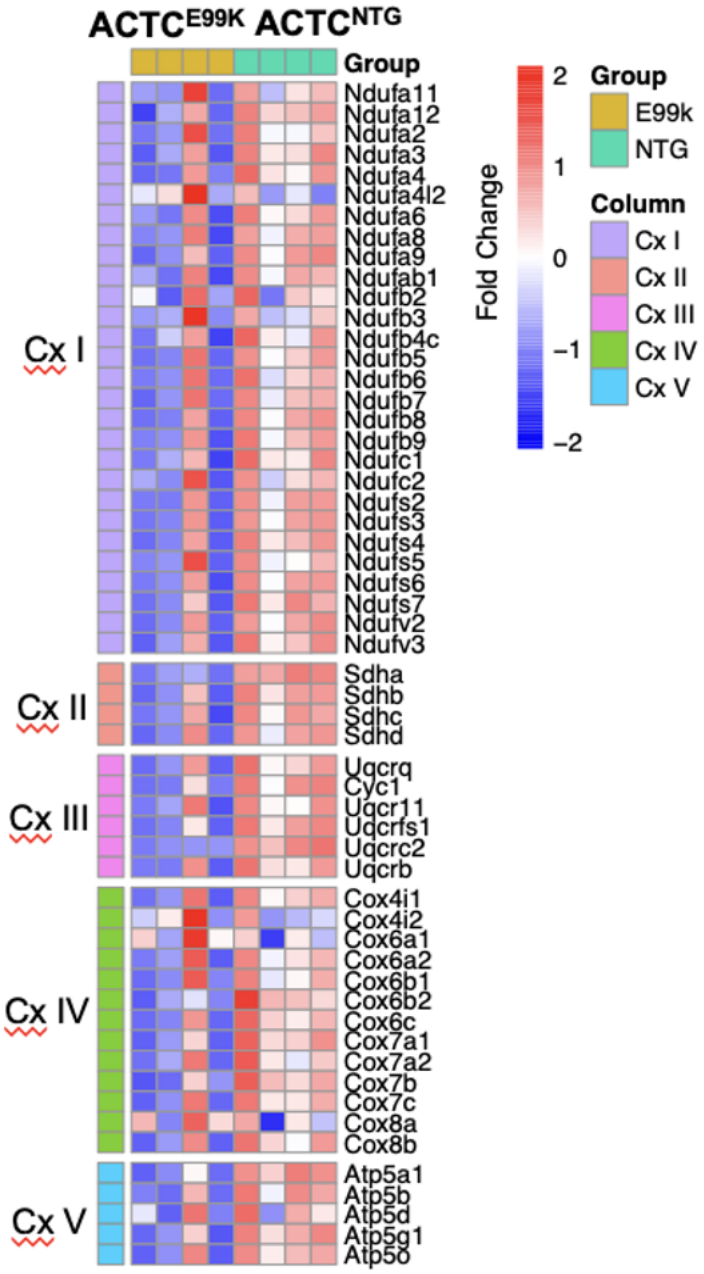

Figure 24. Transcriptional downregulation of electron transport chain (ETC) complexes in ACTC^{E99K} hearts at 10 weeks. Heatmap generated from RNA-seq data, displaying the expression levels of genes encoding key subunits of mitochondrial oxidative phosphorylation complexes (I-V) in ventricular tissues from ACTC^{E99K} and ACTC^{NTG} hearts at 10-week of age. Each row represents an individual gene, and each column represents an independent biological replicate (n = 3-4 per group). The colour scale indicates Z-score normalized expression levels, with bule representing downregulation and red representing upregulation of ACTC^{E99K} compared to the ACTC^{NTG} group. A coordinated downregulating across multiple subunits of all five complexes is evident as early as 10 weeks, indicating an early-onset impairment in

mitochondrial respiratory capacity. Cx I: NADH Dehydrogenase (Complex I), Cx II: Succinate Dehydrogenase Complex (Complex II), Cx III: Cytochrome bc_1 Complex (Complex III), Cx IV: Cytochrome c Oxidase (Complex IV), Cx V: ATP Synthase (Complex V).

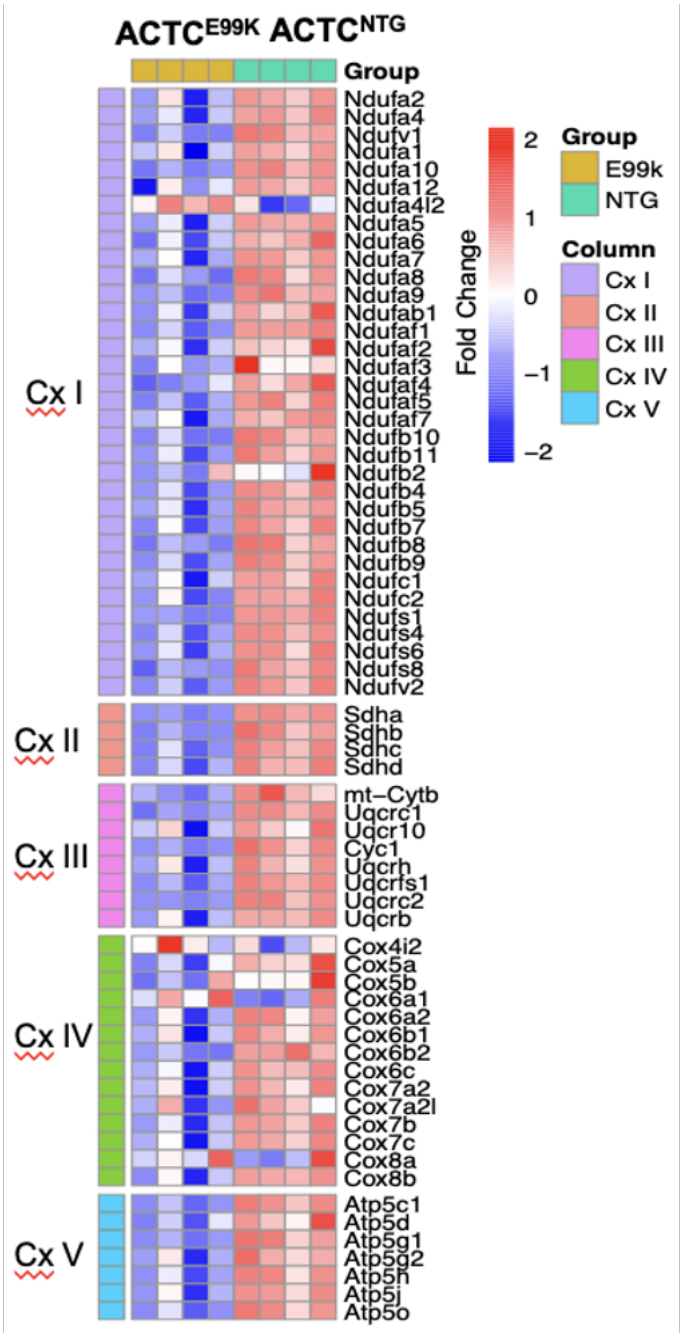

Figure 25. Sustained impairment of ETC gene expression in ACTC^{E99K} hearts at 24 weeks. Heatmap visualizing the expression profiles of genes encoding subunits of mitochondrial complexes I-V from RNA-seq data of 24-week-old ACTC^{E99K} and ACTC^{NTG} hearts ventricular tissues. The colour spectrum (blue to red) corresponds to Z-score normalized expression, revealed a persistent and broad suppression of the transcriptional program governing oxidative phosphorylation at 24 weeks. This sustained downregulation suggests a chronic energy deficit state in the mutant hearts, which likely contributes to the progression of contractile dysfunction and pathological remodeling. Cx I: NADH Dehydrogenase (Complex I), Cx II: Succinate

Dehydrogenase Complex (Complex II), Cx III: Cytochrome bc_1 Complex (Complex III), Cx IV: Cytochrome c Oxidase (Complex IV), Cx V: ATP Synthase (Complex V).

3.8. Differentiated expression of electron transport chain-related proteins

To confirm whether transcriptomic differences in ETC-related genes between the $ACTC^{E99K}$ and $ACTC^{NTG}$ group could result in changes at the protein levels, classic ETC-related proteins from Complexes I to V (Atp5a, UQCRC2, MTCO1, SDHB, NDUFB8) were quantitated by western blot analysis at different time-points (10, 24, and 54 weeks). Although no difference of Complex I (NDUFB8) was observed between $ACTC^{E99K}$ and $ACTC^{NTG}$ group at each time-point, the remaining proteins were significantly decreased in the $ACTC^{E99K}$ group at least at one time-point (**Figure 26**).

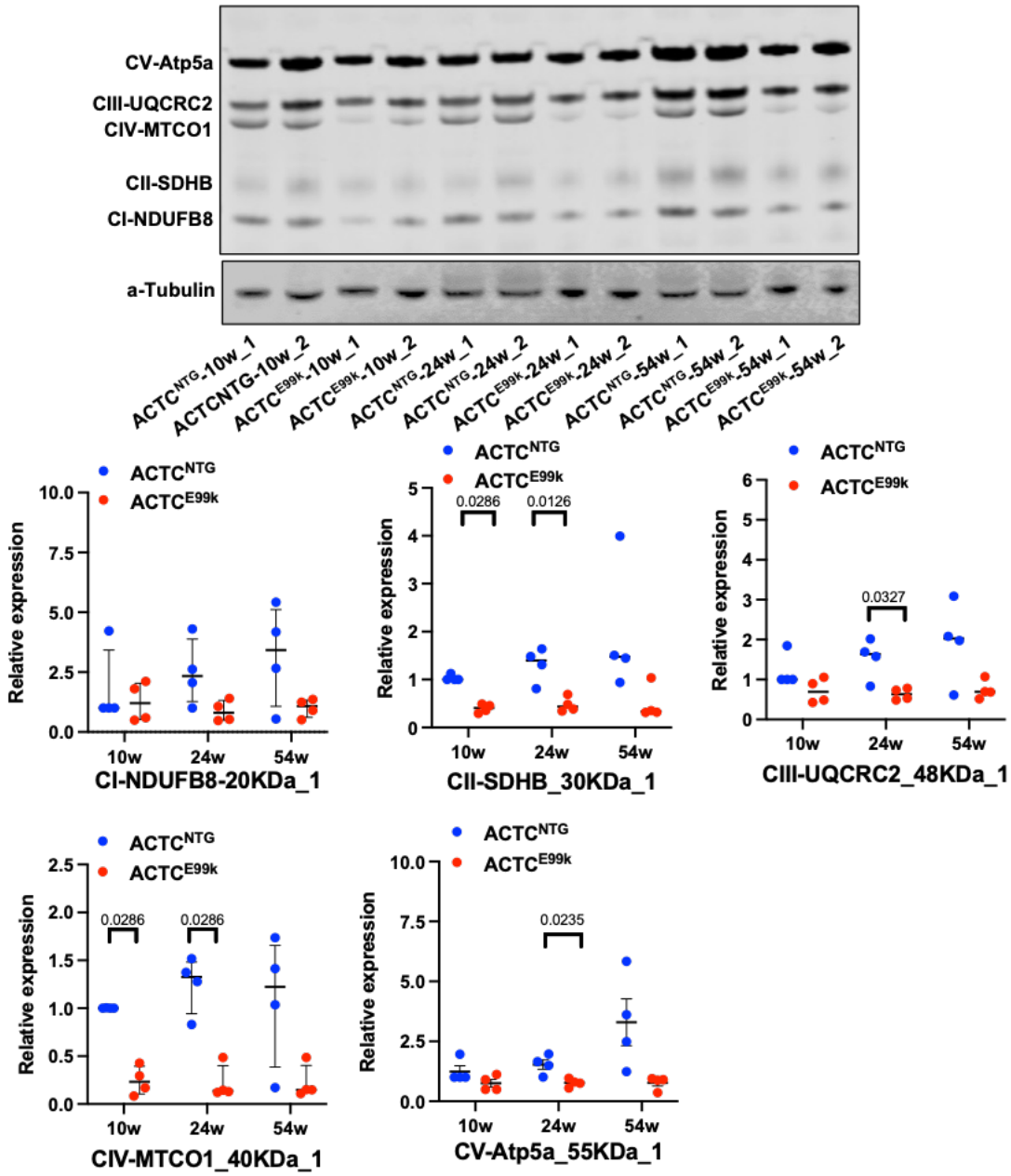

Figure 26. Altered abundance of oxidative phosphorylation (OXPHOS) system proteins in ACTC^{E99K} hearts. (Top) Representative Western blot images of oxidative phosphorylation (OXPHOS) complex proteins (CI-NDUFB8, CII-SDHB, CIII-UQCRC2, CIV-MTCO1, CV-ATP5A) and loading control (α-Tubulin) in ventricular lysates from ACTC^{E99K} and ACTC^{NTG} mice at 10, 24, and 54 weeks. (Bottom) semi-quantification of protein levels normalized to α-Tubulin. Data are presented as mean ± SD (n=3-5 mice per group). Significant reductions in the abundance of multiple ETC components, particularly at later time points, confirm the transcriptomic findings and demonstrate a post-translational impairment of the mitochondrial respiratory machinery in HCM pathogenesis.

3.9. Differentiated expression of glycometabolism and fatty acid metabolism-related proteins

To investigate which type of cardiac metabolism was affected in ACTC^{E99K} induce HCM, I compared the transcriptional expression of genes related to glycometabolism and fatty acid metabolism between two groups. The results showed several genes involved in glycometabolism and fatty acid metabolism were significant decreased at the transcriptional level in ACTC^{E99K} mice (**Figure 27**).

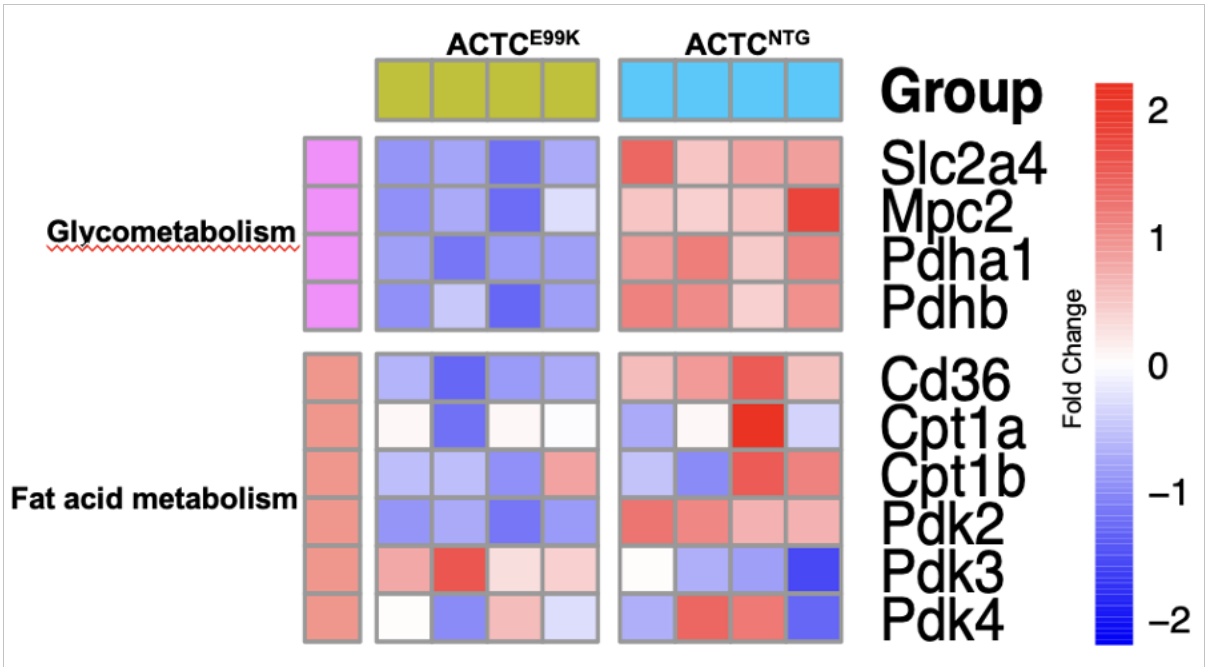

Figure 27. Coordinated dysregulation of metabolic and calcium handling pathways at the transcriptional level in ACTC^{E99K} hearts at 24 weeks. Heatmap of RNA-seq data from 24-week-old hearts, showing the expression pattern of selected key genes involved in distinct yet interconnected pathological processes glycometabolism (e.g., Slc2a4, Pdha1), fatty acid metabolism (e.g., Cpt1a, Cpt1b), and sarcoplasmic reticulum calcium handling (e.g., Atp2a2/SERCA2a, Ryr2). The colour scale indicates Z-score normalized expression levels. The concurrent downregulation of genes critical for both major energy substrates and calcium cycling highlights the integrated nature of metabolic and electrophysiological dysfunction in ACTC^{E99K}-induced HCM.

3.10. Decreased CPT1a expression in ACTC^{E99K} induced HCM

Additionally, I detected carnitine palmitoyltransferase 1a (CPT1a) expression at the protein level, as a significant protein in fatty acid metabolism. The results showed that CPT1a was downregulated in the ACTC^{E99K} group at 24- and 54-week, but no difference was observed at 10-week (**Figure 28**).

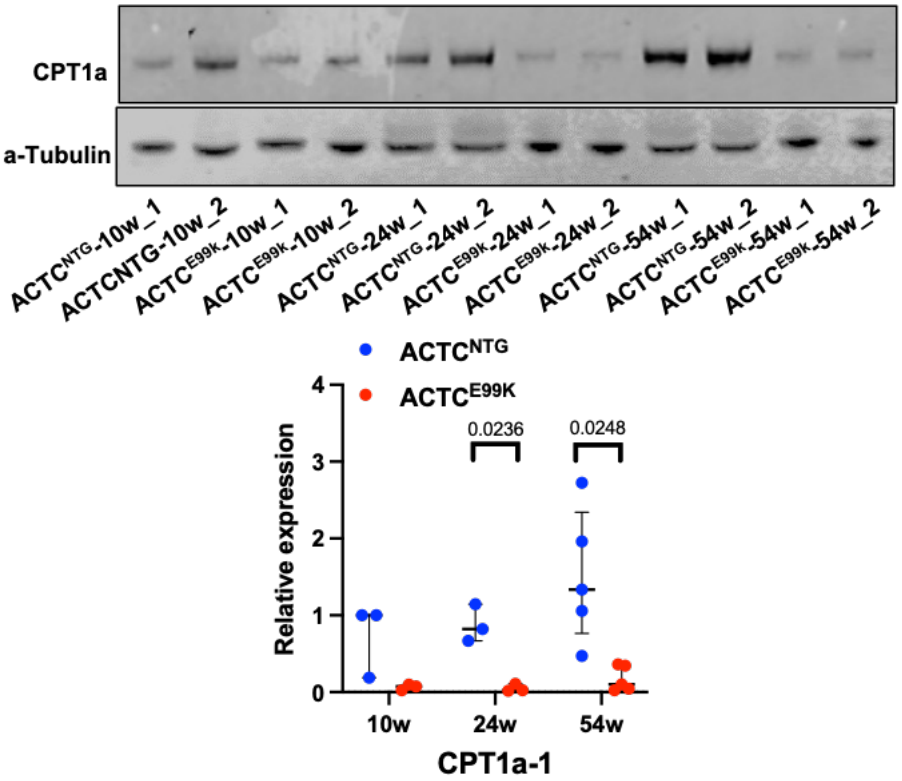

Figure 28. **Progressive loss of CPT1a protein in ACTC^{E99K} hearts.** (Top) Representative Western blot images of carnitine palmitoyltransferase 1a (CPT1a), the rate-limiting enzyme for mitochondrial fatty acid uptake, in ventricles of ACTC^{E99K} and ACTC^{NTG} mice at 10, 24, 54 weeks. Loading control (α-Tubulin) serves as the loading control. (Bottom) Densitometric quantification of CPT1a protein levels normalized to α-Tubulin across different ages. Data are presented as mean ± SD (n=3-5 mice per group). While no difference was observed at the early 10-week time point, CPT1a protein was significantly downregulated at 24 and 54 weeks, indicating a develop defect in fatty acid oxidation capacity that coincides with the progression of hypertrophy and dysfunction.

3.11. Differentiated expression of mitochondria-related genes

To confirm whether mitochondrial metabolism was affected in ACTC^{E99K} mice, the transcriptional data implied that many mitochondrial-related genes showed decreased expression at 10- and 24-week in ACTC^{E99K} mice (**Figure 29-30**).

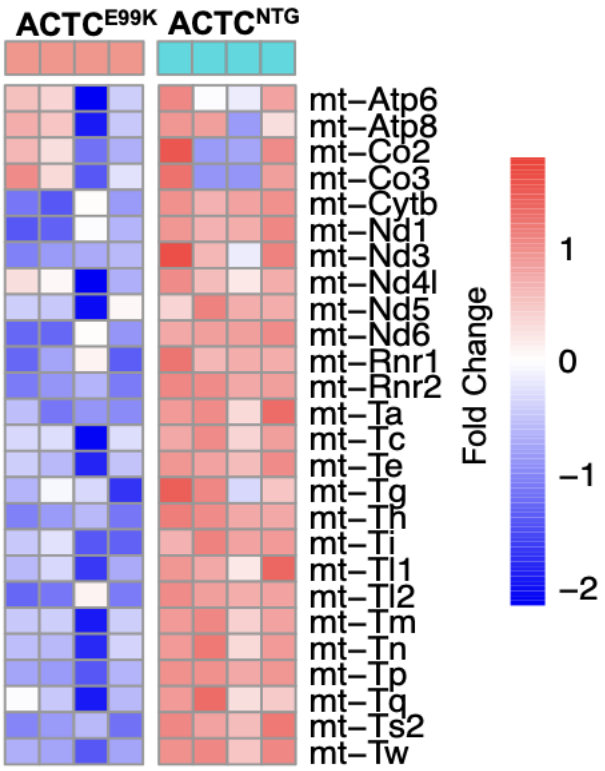

Figure 29. **Broad downregulation of mitochondrial-related genes in ACTC^{E99K} hearts at 10 weeks.** Comprehensive heatmap of RNA-seq data illustrating the expression of a wide array of genes associated with various mitochondrial functions, including biogenesis, metabolism, and transport, in 10-week-old ACTC^{E99K} and ACTC^{NTG} hearts. The colour scale represents Z-score normalized expression. The pervasive blue hue across numerous genes indicates a global transcriptional suppression of the mitochondrial genome and nuclear-encoded mitochondrial genes at this early disease stage, preceding overt systolic failure.

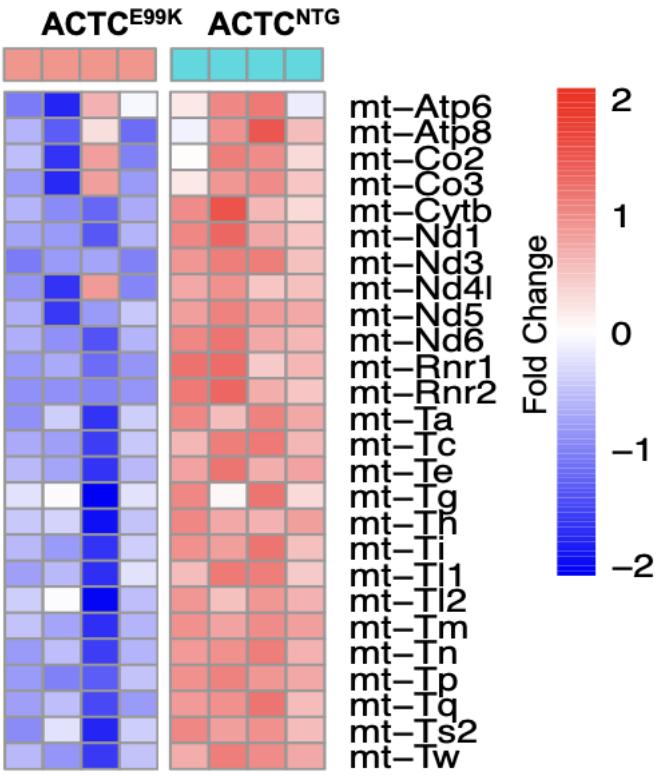

Figure 30. **Persistent suppression of the mitochondrial transcriptome at 24 weeks.** Heatmap of RNA-seq data showing the expression profile of a broad panel of mitochondrial-related genes in 24-week-old hearts. The colour scale indicates Z-score normalized expression levels. The widespread and sustained downregulation observed reinforces that mitochondrial transcriptional dysregulation is a core and persistent feature of the ACTC^{E99K} HCM model, contributing to the chronic energetic impairment.

3.12. Mitochondrial content

Additionally, I detected mitochondrial content between two groups at 10-, 24-, and 54-week. The expression levels of ND1 and 16s rRNA were used as representatives of mitochondrial DNA (mtDNA); both were decreased in ACTC^{E99K} mice at each time-point (**Figures 31-32**). These results implied that content of cardiac mitochondria was significantly decreased in ACTC^{E99K} mice at all time-points.

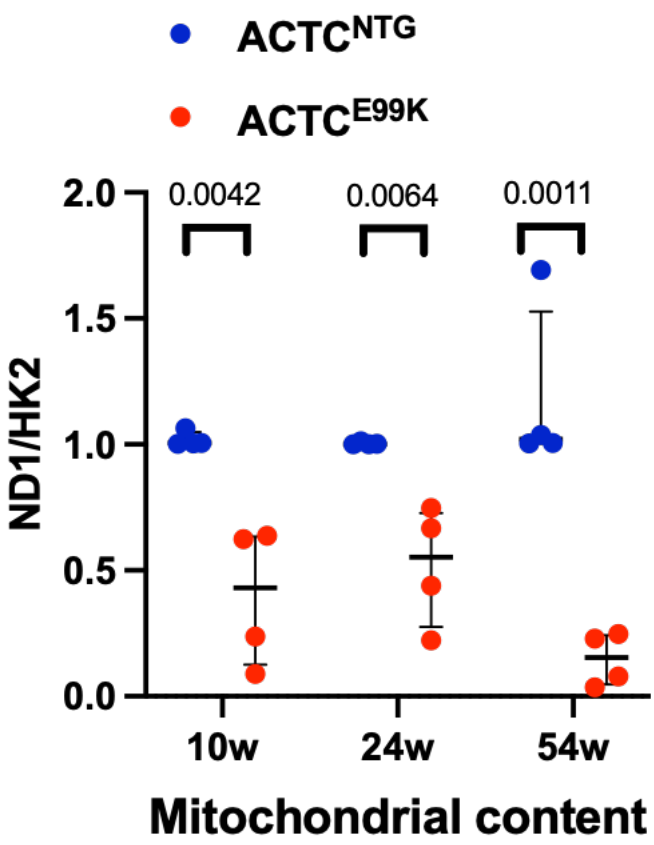

Figure 31. **Reduced mitochondrial DNA content in ACTC^{E99K} hearts.** Quantitative PCR (qPCR) analysis of mitochondrial DNA (mtDNA) content relative to genomic DNA in ventricles of ACTC^{E99K} and ACTC^{NTG} mice at 10, 24, and 54 weeks. MtDNA was quantified using primers specific for the mitochondrial gene ND1 and normalized to the nuclear gene HK2. Data are presented as mean ± SD (n=4 mice per group). A significant reduction in mtDNA copy number was detected in ACTC^{E99K} hearts at all time points, suggesting a loss of mitochondrial mass or integrity that begins early and persists throughout disease progression.

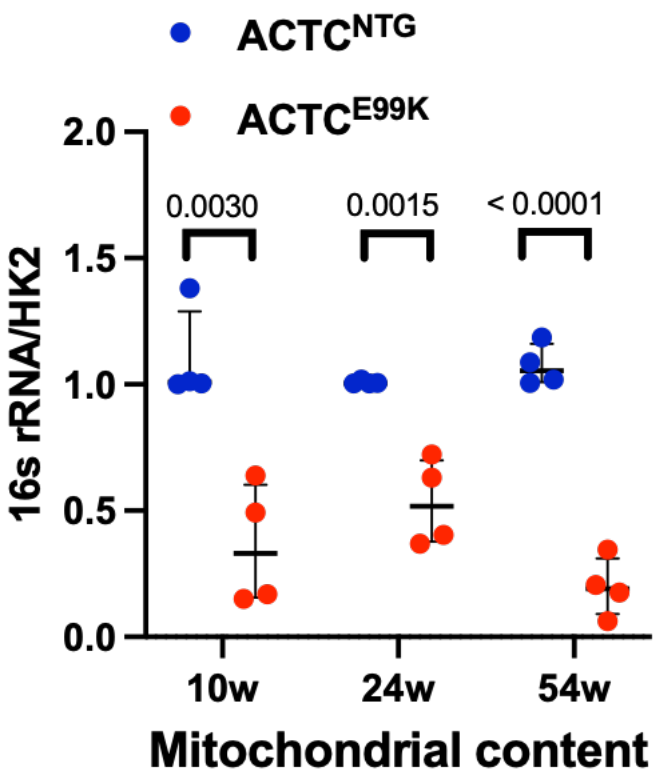

Figure 32. **Reduced mitochondrial DNA content in ACTC^{E99K} hearts.** Quantitative PCR analysis (qPCR) of mitochondrial DNA (mtDNA) content relative to genomic DNA, using primers for the mitochondrial 16S rRNA gene and normalized to the nuclear gene HK2 in ventricles of ACTC^{E99K} and ACTC^{NTG} mice at 10, 24, and 54 weeks. The consistent decrease in mtDNA levels, as measured by this second, independent mitochondrial target, validates the finding of diminished mitochondrial content in ACTC^{E99K} hearts and strengthens the conclusion of mitochondrial depletion in HCM. Data are presented as mean ± SD (n=4 mice per group).

3.13. Calcium homeostasis

Given the contractile function was affected in ACTC^{E99K} mice, I analysed transcripts of proteins involved in calcium homeostasis in the sarcoplasmic reticulum between the two groups. Transcriptome data indicated decreased transcriptional expression of calcium-related genes in ACTC^{E99K} mice (**Figure 33**).

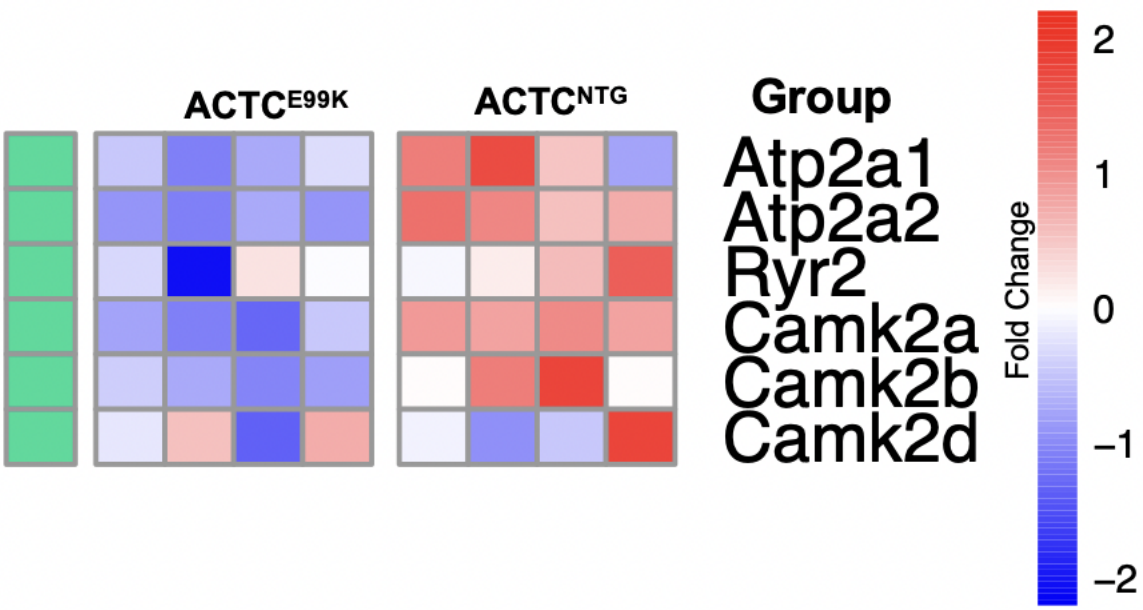

Figure 33. **Perturbed calcium homeostasis gene expression in ACTC^{E99K} hearts.** Heatmap of RNA-seq data from 24-week-old hearts, depicting the expression of pivotal genes governing cardiac calcium homeostasis. This includes the sarcoplasmic reticulum (SR) calcium reuptake pump (Atp2a2/SERCA2a), the SR calcium release channel (Ryr2), and key regulatory kinases (Camk2d). The colour scale indicates Z-score normalized expression levels. The predominant downregulation of these critical regulators provides a molecular basis for the impaired calcium cycling and slowed relaxation observed in HCM, linking sarcomeric mutations to electrophysiological abnormalities.

SERCA2a expression at the protein level was evaluated by western blot. The result showed SERCA2a was downregulated in the ACTC^{E99K} group at 24- and 54-week, but no difference was observed at 10-week (**Figure 34**).

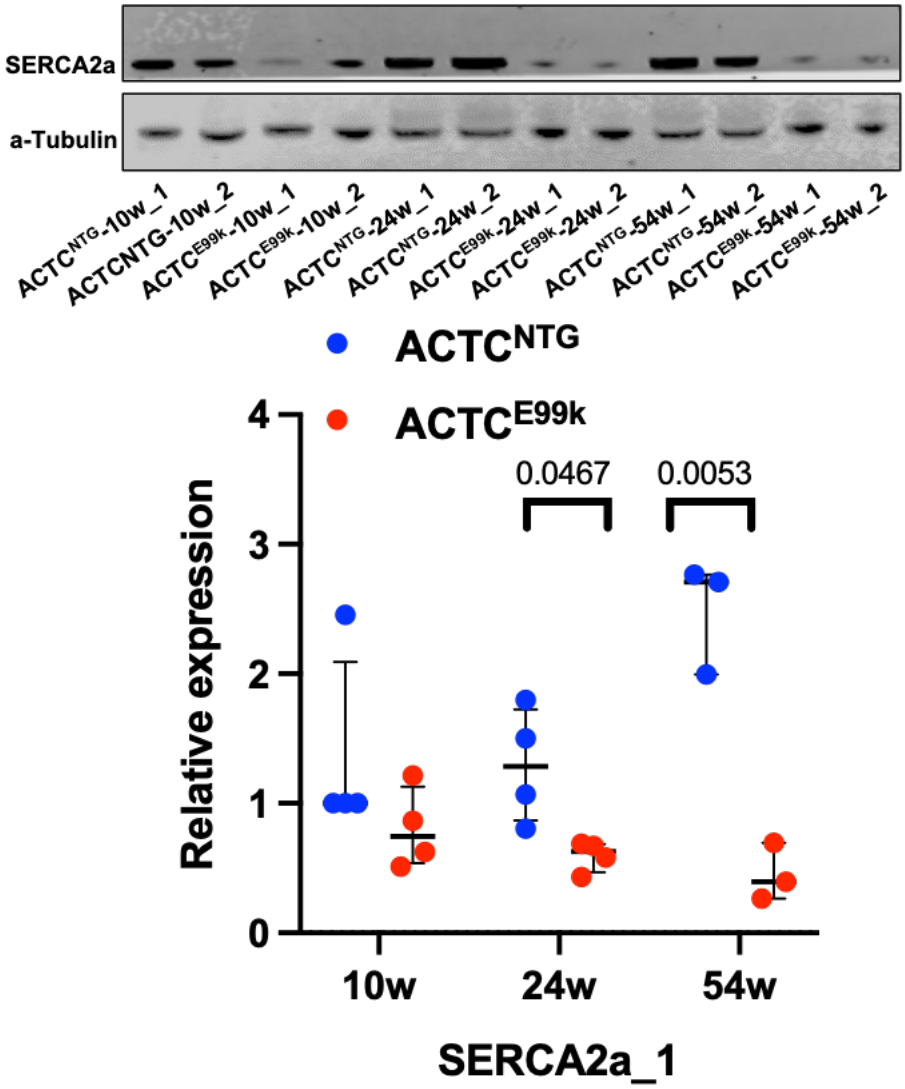

Figure 34. SERCA2a protein expression is decreased in ACTC^{E99K} hearts from 24 weeks. **(Top)** Representative Western blot images of SERCA2a, the primary pump responsible for diastolic calcium reuptake into the SR, and loading control (α-Tubulin) in ventricular lysates from ACTC^{E99K} and ACTC^{NTG} mice. **(Bottom)** Densitometric quantification of SERCA2a protein levels normalized to α-Tubulin. Data are presented as mean ± SD (n=3-5 mice per group). SERCA2a protein expression was significantly reduced at 24 and 54 weeks, but not at 10 weeks, indicating that this specific defect in calcium handling develops alongside the progression of contractile dysfunction and heart failure.

Chapter 4. DISCUSSION

The findings presented in this work demonstrate that the ACTC^{E99K} mutation triggers early-onset cardiac hypertrophy, with a pronounced predisposition of the apical region, accompanied by accelerated fibrotic accumulation. Furthermore, the mutation induces significant contractile dysfunction, evidenced by a reduced EF from as early as 10-week of age. Bulk RNA sequencing revealed persistent downregulation of key metabolic genes including Aldob and Acsm5 across the disease time course. GO enrichment analysis highlighted significant alterations in mitochondrial components and extracellular matrix from the early stages, with a progression towards immune response activation at the later time point. KEGG pathway analysis further implicated the MAPK signalling pathway in the advanced disease stage. Crucially, I provide compelling evidence for a severe impairment of cardiac energetics, with downregulation of both glycometabolic and fatty acid oxidative pathways, accompanied by mitochondrial dysfunction and disruption of calcium homeostasis. My data strongly suggest that abnormal mitochondrial metabolism and dysregulated calcium handling are key contributors to the pathogenesis of ACTC^{E99K} -induced HCM. This study thereby validates the ACTC^{E99K} mouse as a highly suitable model for dissecting the molecular mechanisms linking sarcomeric mutations to metabolic dysregulation and subsequent cardiac remodelling in HCM (**Figure 35**).

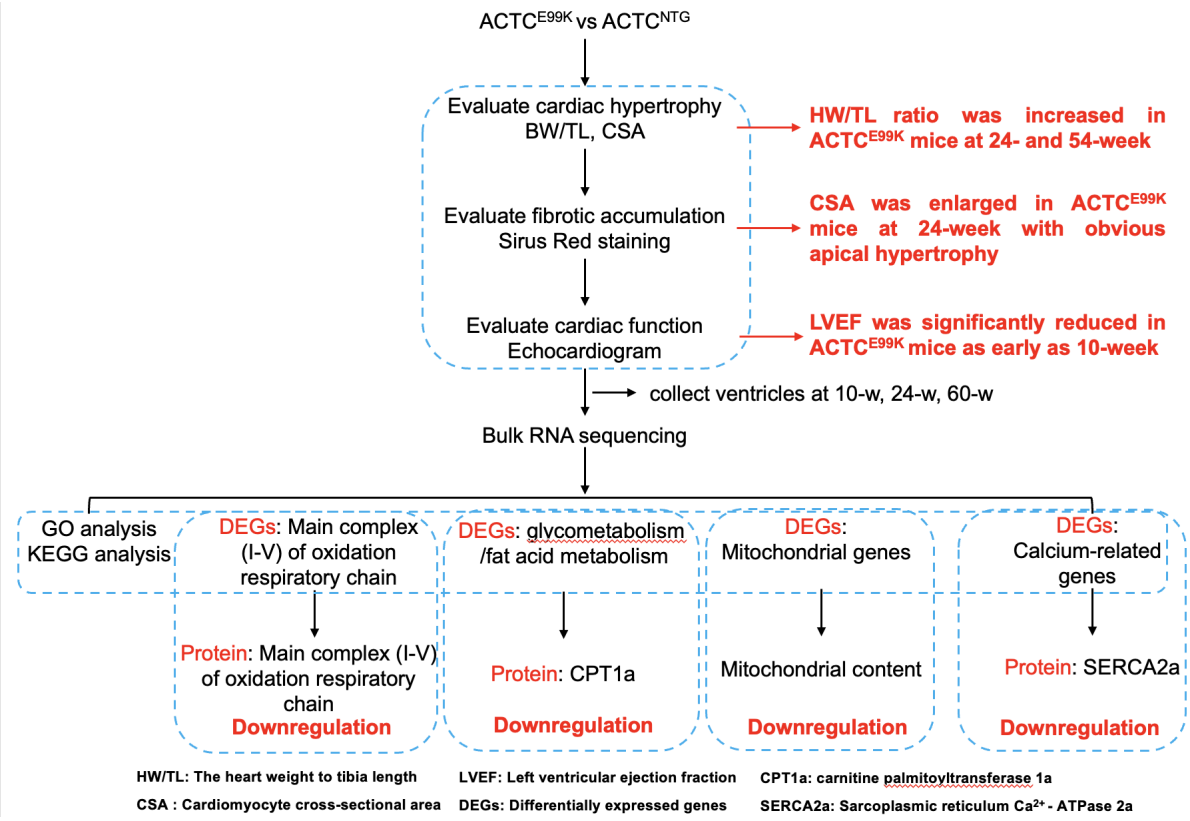

Figure 35. Schematic summary of the proposed pathogenic mechanism in ACTC^{E99K}-induced HCM. This diagram integrates the key finding of the study to illustrate the hypothesized cascade of events. The primary ACTC^{E99K} sarcomeric mutation leads to early transcriptional dysregulation, causing a combined impairment in glycometabolism and fatty acid oxidation, mitochondrial dysfunction evidenced by reduced ETC protein expression and mtDNA content, and disrupted calcium homeostasis. These interconnected deficits in energy supply and electrophysiological stability ultimately drive the pathological endpoints of accelerated cardiac fibrosis and contractile dysfunction with reduced ejection fraction, characterizing the HCM phenotype.

In clinical practice, HCM is characterized by asymmetrical hypertrophy of the interventricular septum and left ventricular free wall, featuring cardiomyocyte enlargement and interstitial fibrosis[109]. Echocardiography serves as a primary non-invasive diagnostic tool, assessing ventricular wall thickness, subaortic pressure gradients, and systolic anterior motion of the mitral valve[110]. In addition, CMR has emerged as a powerful modality for high-resolution

evaluation of wall motion abnormalities and detection of replacement fibrosis via late gadolinium enhancement (LGE)[82, 111].

The familial aggregation of HCM has long been recognized, with pathogenic variants in genes encoding sarcomeric proteins constituting the predominant genetic substrate. Approximately 40-50% of HCM patients harbour causative mutations in one of eight core sarcomere genes[89]. While mutations in non-sarcomere genes (e.g., CSRP3) can cause HCM[112], a substantial proportion of patients are classified as genotype-negative, suggesting a potential polygenic or oligogenic inheritance[113, 114]. Although significant effort has been dedicated to identifying genetic variants, the secondary mechanisms driving disease pathogenesis remain less well elucidated. Therefore, a well-characterized experimental model is indispensable for a comprehensive investigation of HCM pathophysiology.

Various model systems have been developed to study HCM, ranging from reductionist biochemical approaches to more physiological whole-animal models, which includes intact heart strips, isolated cardiomyocytes, myofibrils from tissues/cells, purified actomyosin, animal models, and human pluripotent stem cells[115]. A number of mouse lines modelling a specific genetic mutation in a sarcomeric protein have been constructed and investigated to establish the potential mechanisms of HCM[35, 116], these have included modelling specific mutations found in the human genes MYH7, MYBPC3, TNNT2, TNNI3, TPM1, MYL2 and MYL3. Although ACTC mutations account for a small fraction of HCM cases, the clinical phenotype of the $ACTC^{E99K}$ mutation has been well-documented in human patients with severe diastolic dysfunction and rare systolic dysfunction[42]. The complete conservation of the amino acid sequence between human and mouse ACTC provides high confidence that the $ACTC^{E99K}$ mouse model faithfully recapitulates the complex pathophysiology of human HCM. In this study, a transgenic rodent model of HCM was chosen, in which the codon 101 of the

ACTC gene was mutated; as in the human, the two N-terminal amino acids were removed post-translationally to form the mature protein, and hence the E99 codon refers to the amino acid in the mature form [35]. In HCM patients, the E99K ACTC mutation is consistently associated with apical hypertrophy, and this feature is replicated in the mouse model in this study[42]. In addition, as reported by Song et al., the $ACTC^{E99K}$ HCM mice showed a pronounced incidence of sudden cardiac death (SCD) particularly in female aged from 28 to 42 days of age[35]. This period of high lethality was attributed to arrhythmic events likely stemming from the mutation-induced increase in myofilament Ca^{2+} sensitivity, which perturbs intracellular Ca^{2+} handling and action potential dynamics, creating a pro-arrhythmic substrate[35].

My data confirm that $ACTC^{E99K}$ HCM mice develop a characteristic phenotype of cardiac hypertrophy and prominent apical fibrosis, consistent with previous reports[35]. HW/TL, a key indicator of cardiac hypertrophy, was significantly increased in $ACTC^{E99K}$ mice from 24-week onward, while a previous study showed the ratio of heart weight and body weight (HW/BW) of $ACTC^{E99K}$ group had no difference at 21-week, but increased at 29-week compared to that of $ACTC^{NTG}$ group, successfully replicating the apical hypertrophy observed in human patient samples[35]. In HCM patients, abnormal fibrotic accumulation is common, with its severity and distribution potentially influenced by the underlying genetic substrate[42], and patients without sarcomere gene mutations may have lower fibrosis[117]. In my mouse model, this type of cardiac hypertrophy was replicated successfully, which was also supported by previous study[35]. LGE and diffuse fibrosis through T1 mapping and/or extracellular volume (ECV) contribute to semi-quantifying cardiac fibrosis, which suggested regional and greater LGE may be found in HCM patients with sarcomere gene mutations. In addition, for HCM patients, cardiac fibrosis is always worsened gradually combined with poor clinical outcomes[118]. My work found the abnormal fibrotic accumulation in the whole heart especially apex, which was

supported by MR results from previous report[35]. Therefore, my ACTC^{E99K} HCM model may be suitable to investigate the mechanism of HCM caused by sarcomere gene mutation.

The mechanisms driving functional decompensation and progression to HF in HCM remain incompletely understood, with myocardial replacement fibrosis being a key candidate. Patients typically present with HF with preserved ejection (HFpEF) initially, however recent evidence indicates that a significant proportion of patients with MYBPC3 and MYH7 mutations can develop advanced HF with reduced ejection fraction (HFrEF)[2, 66]. Around 17% HCM patients may develop advanced HF, and symptoms of HF can be worsened followed by systolic dysfunction. In my HCM model, I observed impaired cardiac systolic function from the early stage of 10 weeks. Song et al. also performed echocardiography and cardiac MR to assess the contraction parameters for ACTC^{E99K} HCM model from 21-weeks, and showed a significant decrease of left ventricular EF value at the 21-week timepoint[35]. This early onset of an HFrEF-like phenotype in the ACTC^{E99K} HCM mouse model, which contrasts with the classical HCM presentation, provides a unique opportunity to study the transition to advanced HF.

Over the past two decades, more than 1000 mutations, predominantly in sarcomeric genes, have been linked to HCM[2, 119]. The initial phase of HCM is frequently associated with increased total force production coupled with inefficient ATP utilization, leading to high myocardial energy demand[120]. When this excess demand cannot be met, energetic stress and adverse remodelling ensue, culminating in metabolic abnormalities and altered substrate utilization. The observation that specific mtDNA mutations can also cause HCM further underscores the contribution of energetic impairment to the disease pathophysiology[25, 121]. In my study, Aldob and Acsm5 were among the very few genes consistently downregulated at all time points. Aldob encodes aldolase B, a crucial enzyme in glycolysis, while Acsm5 activates medium-chain fatty acids for β-oxidation. Their persistent downregulation strongly

supports the notion that a generalized attenuation of cardiac metabolism is a central feature of ACTC^{E99K} HCM pathogenesis. GO analysis reinforced this, showing significant enrichment of DEGs in mitochondrial-related cellular components and metabolic biological processes at early and mid-stages, with a notable shift towards immune and inflammatory pathways at the late stage.

Specifically, the transcriptional expression of components across all five complexes of the mitochondrial respiratory chain was reduced in my HCM mouse model, which is consistent with previously reported integrated omics analysis of human samples[25]. This aligns with integrated multi-omics analyses of human HCM samples, which identified aberrant metabolic signalling as a common node in disease pathogenesis, affecting both glucose and lipid metabolism, which is broadly consistent with my data. My transcriptomic data confirmed significant perturbations in both glycometabolism and fatty acid metabolism. The downregulation of CPT1a and CPT1b, critical regulators of mitochondrial fatty acid uptake, suggests a substantial impairment in fatty acid oxidation. Inactivation of CPT1b has been shown to negatively impact fatty acid oxidation in cardiomyocytes, and its depletion has been linked to severe HCM, highlighting the pathophysiological relevance of my findings[122]. Previous study also demonstrated the depletion of CPT1b may result in potential fatal HCM[123]. For the mitochondrial complex activity, previous study showed in HCM patients, the ATP production was significantly decreased with a significant decrease of mitochondrial complex II and V[25]. While we did not directly assay mitochondrial complex activities, the observed downregulation of their protein components is consistent with reports of decreased ATP production and reduced activities of Complex II and V in human HCM samples.

Mitochondria, through oxidative phosphorylation (OXPHOS), supply the majority of the heart's energy, and impaired OXPHOS directly affects the ability to meet myocardial energetic

demands – a phenomenon reported in both animal and human HCM[91]. Abnormal mitochondrial morphology including disorganization and reduced cristae density, has been detected in HCM using transmission electron microscope (TEM)[25, 91, 124]. To further validate this, I quantified the mitochondrial DNA content and found it to be reduced from 10 weeks onwards, a finding consistent with observations in human HCM samples[25]. Mitochondrial DNA is particularly vulnerable to ROS due to the lack of protective histones and limited repair capacity[125]. The early reduction in mtDNA content in the $ACTC^{E99K}$ HCM model likely contributes to the ETC alterations and parallels the pathophysiological progression in human HCM.

In HCM, genetic mutations in sarcomeric proteins often lead to aberrant calcium handling, increasing arrhythmic risk and worsening cardiac function[4, 94]. Calcium homeostasis is critical for excitation-contraction coupling, and its dysregulation can manifest as altered resting calcium levels, abnormal transients, and modified expression of calcium-handling proteins[93]. In human HCM, calcium signalling dysregulation comprises both genotype-dependent and genotype-independent components[94]. For instance, post-translational activation of calcium/calmodulin-dependent protein kinase type II (CaMKII) is specific to sarcomere mutation-positive HCM, while reduced SERCA2a expression and impaired sarcoplasmic reticulum Ca^{2+} uptake appear to be common features across all HCM subtypes[94]. In our model, the downregulation of SERCA2a protein aligns with this genotype-independent calcium signalling dysfunction[94]. Furthermore, our transcriptomic analysis revealed a broader downregulation of calcium-regulating genes, reinforcing that calcium homeostasis is compromised.

Inherited HCM is initiated by genetically determined cardiomyocyte dysfunction (typically hypercontractility), but its full progression involves extra-cardiomyocyte events, including

dysregulated fibrosis and immune activation. My study implicates abnormal mitochondrial metabolism and calcium dysregulation in the pathogenesis of ACTC^{E99K} HCM. The communication between hypertrophic cardiomyocytes and non-myocytes, however, remains an open question. In other cardiac stress models, cardiomyocytes release specific component, including dysfunctional mitochondrial, which can signal to adjacent macrophages, suggesting that stress signals are actively transmitted to the non-myocyte compartment to orchestrate pathology[126].

My GO analysis (Cell component) at 60 weeks of age revealed significant enrichment in neuronal signalling pathways, which may reflect alterations in cardiac sympathetic innervation. According to Coote and Chauhan, the sympathetic nervous system exerts critical control over cardiac function, with preganglionic neurons originating from the T1–T6 spinal segments and synapsing primarily in the stellate and cervical ganglia before projecting to the heart. These nerves differentially regulate chronotropy, inotropy, and dromotropy in a region-specific manner, and their dysregulation is implicated in arrhythmogenesis and heart failure[127]. The observed enrichment in neuronal pathways in our ACTC^{E99K} HCM model may indicate compensatory or maladaptive remodelling of cardiac sympathetic innervation during disease progression. Such neuro-cardiac interactions could further exacerbate metabolic dysfunction and calcium mishandling, contributing to the observed contractile impairment and fibrotic accumulation. Moreover, targeted neuromodulatory approaches such as dorsal spinal cord stimulation have shown promise in mitigating sympathetic overactivity in HCM, suggesting that sympathetic pathways represent a potential therapeutic target worthy of further investigation in this model.

While this study provides insights into the abnormal metabolic and calcium handling alterations in accelerated cardiac fibrosis and dysfunction of ACTC^{E99K} induced HCM, several

limitations should be acknowledged. First, the use of α-tubulin as a loading control for Western blot analysis may not be ideal in the context of cardiac hypertrophy and fibrosis, as tubulin expression can be influenced by cellular stress, cytoskeletal remodelling, or disease state. Future studies should consider using multiple housekeeping proteins to improve the reliability of protein quantification. Second, the statistical analysis relied solely on the unpaired Student's t-test for comparisons between two groups. While appropriate for many experiments, this approach does not account for multiple comparisons across time points or between multiple groups. The use of ANOVA with post-hoc tests would have been more suitable for longitudinal data and multi-group analyses, reducing the risk of Type I errors. Additionally, the sample sizes in some experimental groups, particularly for echocardiography and molecular analyses, might be relatively small, which limits the statistical power and generalizability of the findings. Finally, the transcriptomic data represent an average of gene expression across all cell types present in the ventricular tissue, including cardiomyocytes, fibroblasts, immune cells, and endothelial cells. Consequently, the observed differential expression, particularly in pathways related to metabolism, extracellular matrix, and immune response, cannot be unequivocally assigned to cardiomyocytes. This cellular heterogeneity obscures cell-type-specific mechanisms, and future work utilizing single-cell or single-nucleus RNA sequencing would be critical to deconvolute these contributions.

Chapter 5. CONCLUSION

In summary, this study demonstrates that the ACTC^{E99K} mutation drives a robust HCM phenotype characterized by the early onset of cardiac hypertrophy, accelerated apical fibrosis, and significant contractile dysfunction with reduced ejection fraction. My integrated molecular analysis revealed that these structural and functional deficits are underpinned by a profound dysregulation of cardiac metabolism, evidenced by the coordinated downregulation of glycolytic and fatty acid oxidative pathways, mitochondrial dysfunction, and disrupted calcium homeostasis. The ACTC^{E99K} mouse model faithfully recapitulates key features of human HCM and serves as an ideal experimental platform for future investigations into the detailed molecular mechanisms linking sarcomeric mutations to metabolic stress and pathological remodeling, potentially informing novel therapeutic strategies.

Chapter 6. FUTURE PLAN

For possible continuation of my study, to confirm whether excessive myocyte death contributes to impaired LVEF as early as 10 weeks of age, I would perform Terminal-deoxynucleoitidyl Transferase Mediated Nick End Labeling (TUNEL) staining to semi-quantify the apoptosis of cardiomyocytes. In addition, I would use TEM to detect the mitochondrial distribution and mitochondrial encapsulated vesicles in heart tissue. Immunofluorescent staining of α-SMA, vimentin or CD45 in heart tissue would be performed and the 3D reconstructed images may define the spatial relation between myocyte components and non-myocytes. Non-myocytes would be sorted and collected through digestion of ventricular tissues, and the expression of MYH7, Troponin I type 3 (TnI3), as typical cell marker of cardiomyocyte may be detected in cardiac fibroblasts and cardiac resident immune cells of $ACTC^{E99k}$ transgenic mice and $ACTC^{NTG}$ mice at 10 weeks, 24 weeks, and 60 weeks. Purified fibroblasts and immune cells will be sorted by FACS and further analysed by Western blotting to detect MYH7 and TnnI3 expression. Cardiac vesicles would be collected by serial centrifugation (forces at 50g, 300g and 1000g) followed by appropriate digestion. Cardiomyocytes derived vesicles would be purified by FACS with MYH7 positive, TnnI3 positive, CD31 negative, and Draq5 negative. Cardiomyocytes vesicles would undergo proteomic analysis and mitochondrial DNA levels would also be detected.

Chapter 7. REFERENCES

1. Maron, B.J., E.J. Rowin, and M.S. Maron, *Global Burden of Hypertrophic Cardiomyopathy*. JACC Heart Fail, 2018. **6**(5): p. 376-378.
2. Ommen, S.R., C.Y. Ho, I.M. Asif, S. Balaji, M.A. Burke, S.M. Day, . . . C.B. Waldman, *2024 AHA/ACC/AMSSM/HRS/PACES/SCMR Guideline for the Management of Hypertrophic Cardiomyopathy: A Report of the American Heart Association/American College of Cardiology Joint Committee on Clinical Practice Guidelines*. Circulation, 2024. **149**(23): p. e1239-e1311.
3. Maron, B.J., M.Y. Desai, R.A. Nishimura, P. Spirito, H. Rakowski, J.A. Towbin, . . . M.V. Sherrid, *Management of Hypertrophic Cardiomyopathy: JACC State-of-the-Art Review*. J Am Coll Cardiol, 2022. **79**(4): p. 390-414.
4. Marian, A.J., *Molecular Genetic Basis of Hypertrophic Cardiomyopathy*. Circ Res, 2021. **128**(10): p. 1533-1553.
5. Rowin, E.J., M.S. Maron, S. Wells, P.P. Patel, B.C. Koethe, and B.J. Maron, *Impact of Sex on Clinical Course and Survival in the Contemporary Treatment Era for Hypertrophic Cardiomyopathy*. J Am Heart Assoc, 2019. **8**(21): p. e012041.
6. Eberly, L.A., S.M. Day, E.A. Ashley, D.L. Jacoby, J.L. Jefferies, S.D. Colan, . . . N.K. Lakdawala, *Association of Race With Disease Expression and Clinical Outcomes Among Patients With Hypertrophic Cardiomyopathy*. JAMA Cardiol, 2020. **5**(1): p. 83-91.
7. Braunwald, E., *Hypertrophic cardiomyopathy: The first century 1869-1969*. Glob Cardiol Sci Pract, 2012. **2012**(1): p. 5.
8. Pare, J.A., R.G. Fraser, W.J. Pirozynski, J.A. Shanks, and D. Stubington, *Hereditary cardiovascular dysplasia. A form of familial cardiomyopathy*. Am J Med, 1961. **31**: p. 37-62.
9. Lehman, S.J., C. Crocini, and L.A. Leinwand, *Targeting the sarcomere in inherited cardiomyopathies*. Nat Rev Cardiol, 2022. **19**(6): p. 353-363.

10. Geisterfer-Lowrance, A.A., S. Kass, G. Tanigawa, H.P. Vosberg, W. McKenna, C.E. Seidman, and J.G. Seidman, *A molecular basis for familial hypertrophic cardiomyopathy: a beta cardiac myosin heavy chain gene missense mutation*. Cell, 1990. **62**(5): p. 999-1006.

11. Gordon, A.M., E. Homsher, and M. Regnier, *Regulation of contraction in striated muscle*. Physiol Rev, 2000. **80**(2): p. 853-924.

12. Michel, L., I. Helfrich, U.B. Hendgen-Cotta, R.I. Mincu, S. Korste, S.M. Mrotzek, . . . T. Rassaf, *Targeting early stages of cardiotoxicity from anti-PD1 immune checkpoint inhibitor therapy*. Eur Heart J, 2022. **43**(4): p. 316-329.

13. Martin, A.A., B.R. Thompson, D. Hahn, A.B.B. Angulski, N. Hosny, H. Cohen, and J.M. Metzger, *Cardiac Sarcomere Signaling in Health and Disease*. Int J Mol Sci, 2022. **23**(24).

14. Granzier, H. and S. Labeit, *Structure-function relations of the giant elastic protein titin in striated and smooth muscle cells*. Muscle Nerve, 2007. **36**(6): p. 740-55.

15. Sequeira, V., E.R. Witjas-Paalberends, D.W. Kuster, and J. van der Velden, *Cardiac myosin-binding protein C: hypertrophic cardiomyopathy mutations and structure-function relationships*. Pflugers Arch, 2014. **466**(2): p. 201-6.

16. Heling, L., M.A. Geeves, and N.M. Kad, *MyBP-C: one protein to govern them all*. J Muscle Res Cell Motil, 2020. **41**(1): p. 91-101.

17. Bers, D.M., *Cardiac excitation–contraction coupling*. Nature, 2002. **415**(6868): p. 198-205.

18. Eisner, D.A., J.L. Caldwell, K. Kistamas, and A.W. Trafford, *Calcium and Excitation-Contraction Coupling in the Heart*. Circ Res, 2017. **121**(2): p. 181-195.

19. Gordon, A.M., M. Regnier, and E. Homsher, *Skeletal and cardiac muscle contractile activation: tropomyosin "rocks and rolls"*. News Physiol Sci, 2001. **16**: p. 49-55.

20. Badr, M.A., J.R. Pinto, M.W. Davidson, and P.B. Chase, *Fluorescent Protein-Based Ca2+ Sensor Reveals Global, Divalent Cation-Dependent Conformational Changes in Cardiac Troponin C*. PLoS One, 2016. **11**(10): p. e0164222.

21. Kranias, E.G. and R.J. Hajjar, *Modulation of cardiac contractility by the phospholamban/SERCA2a regulatome*. Circ Res, 2012. **110**(12): p. 1646-60.

22. Irving, M., *Regulation of Contraction by the Thick Filaments in Skeletal Muscle*. Biophys J, 2017. **113**(12): p. 2579-2594.

23. Brunello, E. and L. Fusi, *Regulating Striated Muscle Contraction: Through Thick and Thin*. Annu Rev Physiol, 2024. **86**: p. 255-275.

24. Garcia-Pavia, P., A. Oreziak, A. Masri, R. Barriales-Villa, T.P. Abraham, A.T. Owens, . . . I. Olivotto, *Long-term effect of mavacamten in obstructive hypertrophic cardiomyopathy*. Eur Heart J, 2024.

25. Ranjbarvaziri, S., K.B. Kooiker, M. Ellenberger, G. Fajardo, M. Zhao, A.S. Vander Roest, . . . D. Bernstein, *Altered Cardiac Energetics and Mitochondrial Dysfunction in Hypertrophic Cardiomyopathy*. Circulation, 2021. **144**(21): p. 1714-1731.

26. Burke, M.A., S.A. Cook, J.G. Seidman, and C.E. Seidman, *Clinical and Mechanistic Insights Into the Genetics of Cardiomyopathy*. J Am Coll Cardiol, 2016. **68**(25): p. 2871-2886.

27. Topriceanu, C.C., A.C. Pereira, J.C. Moon, G. Captur, and C.Y. Ho, *Meta-Analysis of Penetrance and Systematic Review on Transition to Disease in Genetic Hypertrophic Cardiomyopathy*. Circulation, 2024. **149**(2): p. 107-123.

28. Authors/Task Force, m., P.M. Elliott, A. Anastasakis, M.A. Borger, M. Borggrefe, F. Cecchi, . . . H. Watkins, *2014 ESC Guidelines on diagnosis and management of hypertrophic cardiomyopathy: the Task Force for the Diagnosis and Management of Hypertrophic Cardiomyopathy of the European Society of Cardiology (ESC)*. Eur Heart J, 2014. **35**(39): p. 2733-79.

29. Curran, L., A. de Marvao, P. Inglese, K.A. McGurk, P.R. Schiratti, A. Clement, . . . D.P. O'Regan, *Genotype-Phenotype Taxonomy of Hypertrophic Cardiomyopathy*. Circ Genom Precis Med, 2023. **16**(6): p. e004200.

30. Richard, P., P. Charron, L. Carrier, C. Ledeuil, T. Cheav, C. Pichereau, . . . E.H.F. Project, *Hypertrophic cardiomyopathy: distribution of disease genes, spectrum of*

mutations, and implications for a molecular diagnosis strategy. Circulation, 2003. **107**(17): p. 2227-32.

31. Helms, A.S., A.D. Thompson, A.A. Glazier, N. Hafeez, S. Kabani, J. Rodriguez, . . . S.M. Day, *Spatial and Functional Distribution of MYBPC3 Pathogenic Variants and Clinical Outcomes in Patients With Hypertrophic Cardiomyopathy*. Circ Genom Precis Med, 2020. **13**(5): p. 396-405.

32. Poetter, K., H. Jiang, S. Hassanzadeh, S.R. Master, A. Chang, M.C. Dalakas, . . . N.D. Epstein, *Mutations in either the essential or regulatory light chains of myosin are associated with a rare myopathy in human heart and skeletal muscle*. Nat Genet, 1996. **13**(1): p. 63-9.

33. Satoh, M., M. Takahashi, T. Sakamoto, M. Hiroe, F. Marumo, and A. Kimura, *Structural analysis of the titin gene in hypertrophic cardiomyopathy: identification of a novel disease gene*. Biochem Biophys Res Commun, 1999. **262**(2): p. 411-7.

34. Carniel, E., M.R. Taylor, G. Sinagra, A. Di Lenarda, L. Ku, P.R. Fain, . . . L. Mestroni, *Alpha-myosin heavy chain: a sarcomeric gene associated with dilated and hypertrophic phenotypes of cardiomyopathy*. Circulation, 2005. **112**(1): p. 54-9.

35. Song, W., E. Dyer, D.J. Stuckey, O. Copeland, M.C. Leung, C. Bayliss, . . . S.B. Marston, *Molecular mechanism of the E99K mutation in cardiac actin (ACTC Gene) that causes apical hypertrophy in man and mouse*. J Biol Chem, 2011. **286**(31): p. 27582-93.

36. Mogensen, J., I.C. Klausen, A.K. Pedersen, H. Egeblad, P. Bross, T.A. Kruse, . . . A.D. Borglum, *Alpha-cardiac actin is a novel disease gene in familial hypertrophic cardiomyopathy*. J Clin Invest, 1999. **103**(10): p. R39-43.

37. Alfares, A.A., M.A. Kelly, G. McDermott, B.H. Funke, M.S. Lebo, S.B. Baxter, . . . H.L. Rehm, *Results of clinical genetic testing of 2,912 probands with hypertrophic cardiomyopathy: expanded panels offer limited additional sensitivity*. Genet Med, 2015. **17**(11): p. 880-8.

38. Becker, E., F. Navarro-Lopez, A. Francino, B. Brenner, and T. Kraft, *Quantification of mutant versus wild-type myosin in human muscle biopsies using nano-LC/ESI-MS*. Anal Chem, 2007. **79**(24): p. 9531-8.

39. Bottinelli, R., D.A. Coviello, C.S. Redwood, M.A. Pellegrino, B.J. Maron, P. Spirito, . . . C. Reggiani, *A mutant tropomyosin that causes hypertrophic cardiomyopathy is expressed in vivo and associated with an increased calcium sensitivity*. Circ Res, 1998. **82**(1): p. 106-15.

40. Watkins, H., H. Ashrafian, and C. Redwood, *Inherited cardiomyopathies*. N Engl J Med, 2011. **364**(17): p. 1643-56.

41. Ashrafian, H., C. Redwood, E. Blair, and H. Watkins, *Hypertrophic cardiomyopathy:a paradigm for myocardial energy depletion*. Trends Genet, 2003. **19**(5): p. 263-8.

42. Monserrat, L., M. Hermida-Prieto, X. Fernandez, I. Rodriguez, C. Dumont, L. Cazon, . . . A. Castro-Beiras, *Mutation in the alpha-cardiac actin gene associated with apical hypertrophic cardiomyopathy, left ventricular non-compaction, and septal defects*. Eur Heart J, 2007. **28**(16): p. 1953-61.

43. Bai, F., H.M. Caster, J.F. Dawson, and M. Kawai, *The immediate effect of HCM causing actin mutants E99K and A230V on actin-Tm-myosin interaction in thin-filament reconstituted myocardium*. J Mol Cell Cardiol, 2015. **79**: p. 123-32.

44. Smith, J.G.W., T. Owen, J.R. Bhagwan, D. Mosqueira, E. Scott, I. Mannhardt, . . . C. Denning, *Isogenic Pairs of hiPSC-CMs with Hypertrophic Cardiomyopathy/LVNC-Associated ACTC1 E99K Mutation Unveil Differential Functional Deficits*. Stem Cell Reports, 2018. **11**(5): p. 1226-1243.

45. Burkart, V., K. Kowalski, D. Aldag-Niebling, J. Beck, D.A. Frick, T. Holler, . . . T. Kraft, *Transcriptional bursts and heterogeneity among cardiomyocytes in hypertrophic cardiomyopathy*. Front Cardiovasc Med, 2022. **9**: p. 987889.

46. Ho, C.Y., S.M. Day, E.A. Ashley, M. Michels, A.C. Pereira, D. Jacoby, . . . I. Olivotto, *Genotype and Lifetime Burden of Disease in Hypertrophic Cardiomyopathy:*

Insights from the Sarcomeric Human Cardiomyopathy Registry (SHaRe). Circulation, 2018. **138**(14): p. 1387-1398.

47. Lopes, L.R., M.-A. Losi, N. Sheikh, C. Laroche, P. Charron, J. Gimeno, . . . E. Marques-Sule, *Association between common cardiovascular risk factors and clinical phenotype in patients with hypertrophic cardiomyopathy from the European Society of Cardiology (ESC) EurObservational Research Programme (EORP) Cardiomyopathy/Myocarditis registry*. European Heart Journal - Quality of Care and Clinical Outcomes, 2023. **9**(1): p. 42-53.

48. Marian, A.J. and E. Braunwald, *Hypertrophic Cardiomyopathy: Genetics, Pathogenesis, Clinical Manifestations, Diagnosis, and Therapy*. Circ Res, 2017. **121**(7): p. 749-770.

49. Bertero, E., C. Chiti, M.A. Schiavo, G. Tini, P. Costa, G. Todiere, . . . M. Canepa, *Real-world candidacy to mavacamten in a contemporary hypertrophic obstructive cardiomyopathy population*. Eur J Heart Fail, 2024. **26**(1): p. 59-64.

50. Maurizi, N., P. Antiochos, A. Owens, N. Lakdwala, S. Saberi, M.W. Russell, . . . I. Olivotto, *Long-Term Outcomes After Septal Reduction Therapies in Obstructive Hypertrophic Cardiomyopathy: Insights From the SHARE Registry*. Circulation, 2024. **150**(17): p. 1377-1390.

51. Hermida, U., D. Stojanovski, B. Raman, R. Ariga, A.A. Young, V. Carapella, . . . P. Lamata, *Left ventricular anatomy in obstructive hypertrophic cardiomyopathy: beyond basal septal hypertrophy*. Eur Heart J Cardiovasc Imaging, 2023. **24**(6): p. 807-818.

52. Geske, J.B., P. Sorajja, S.R. Ommen, and R.A. Nishimura, *Variability of left ventricular outflow tract gradient during cardiac catheterization in patients with hypertrophic cardiomyopathy*. JACC Cardiovasc Interv, 2011. **4**(6): p. 704-9.

53. Joshi, S., U.K. Patel, S.S. Yao, V. Castenada, A. Isambert, G. Winson, . . . M.V. Sherrid, *Standing and exercise Doppler echocardiography in obstructive hypertrophic cardiomyopathy: the range of gradients with upright activity*. J Am Soc Echocardiogr, 2011. **24**(1): p. 75-82.

54. Ayoub, C., J.B. Geske, C.M. Larsen, C.G. Scott, K.W. Klarich, and P.A. Pellikka, *Comparison of Valsalva Maneuver, Amyl Nitrite, and Exercise Echocardiography to Demonstrate Latent Left Ventricular Outflow Obstruction in Hypertrophic Cardiomyopathy*. Am J Cardiol, 2017. **120**(12): p. 2265-2271.

55. Bois, J.P., J.B. Geske, T.A. Foley, S.R. Ommen, and P.A. Pellikka, *Comparison of Maximal Wall Thickness in Hypertrophic Cardiomyopathy Differs Between Magnetic Resonance Imaging and Transthoracic Echocardiography*. Am J Cardiol, 2017. **119**(4): p. 643-650.

56. Biagini, E., P. Spirito, G. Rocchi, M. Ferlito, S. Rosmini, F. Lai, . . . C. Rapezzi, *Prognostic implications of the Doppler restrictive filling pattern in hypertrophic cardiomyopathy*. Am J Cardiol, 2009. **104**(12): p. 1727-31.

57. Molisana, M., A. Selimi, G. Gizzi, S. D'Agostino, U. Ianni, and V.M. Parato, *Different mechanisms of mitral regurgitation in hypertrophic cardiomyopathy: A clinical case and literature review*. Front Cardiovasc Med, 2022. **9**: p. 1020054.

58. Kim, D.Y., J. Seo, I. Cho, G.R. Hong, J.W. Ha, and C.Y. Shim, *Prognostic Implication of Mitral Valve Disease and Its Progression in East Asian Patients With Hypertrophic Cardiomyopathy*. J Am Heart Assoc, 2023. **12**(3): p. e024792.

59. Coleman, J.A., Z. Ashkir, B. Raman, and A. Bueno-Orovio, *Mechanisms and prognostic impact of myocardial ischaemia in hypertrophic cardiomyopathy*. Int J Cardiovasc Imaging, 2023. **39**(10): p. 1979-1996.

60. Maron, B.J., S.E. Epstein, and W.C. Roberts, *Hypertrophic cardiomyopathy and transmural myocardial infarction without significant atherosclerosis of the extramural coronary arteries*. Am J Cardiol, 1979. **43**(6): p. 1086-102.

61. Bogatyreva, F.M., V.R.Y. Kaplunova, M.V. Kozhevnikova, G.A. Shakaryants, N.V. Khabarova, E.V. Privalova, and Y.N. Belenkov, *[Assessment of the structural and functional state of blood vessels in patients with hypertrophic cardiomyopathy]*. Kardiologiia, 2021. **61**(12): p. 16-21.

62. Tesic, M., A. Djordjevic-Dikic, B. Beleslin, D. Trifunovic, V. Giga, J. Marinkovic, . . . B. Vujisic-Tesic, *Regional difference of microcirculation in patients with*

asymmetric hypertrophic cardiomyopathy: transthoracic Doppler coronary flow velocity reserve analysis. J Am Soc Echocardiogr, 2013. **26**(7): p. 775-82.

63. Marszalek, R.J., R. John Solaro, and B.M. Wolska, *Coronary arterial vasculature in the pathophysiology of hypertrophic cardiomyopathy*. Pflugers Arch, 2019. **471**(5): p. 769-780.

64. Basso, C., G. Thiene, S. Mackey-Bojack, A.C. Frigo, D. Corrado, and B.J. Maron, *Myocardial bridging, a frequent component of the hypertrophic cardiomyopathy phenotype, lacks systematic association with sudden cardiac death*. Eur Heart J, 2009. **30**(13): p. 1627-34.

65. Weissler-Snir, A., W. Hindieh, C. Gruner, D. Fourey, E. Appelbaum, E. Rowin, . . . R.H. Chan, *Lack of Phenotypic Differences by Cardiovascular Magnetic Resonance Imaging in MYH7 (beta-Myosin Heavy Chain)- Versus MYBPC3 (Myosin-Binding Protein C)-Related Hypertrophic Cardiomyopathy*. Circ Cardiovasc Imaging, 2017. **10**(2).

66. Beltrami, M., E. Fedele, C. Fumagalli, F. Mazzarotto, F. Girolami, C. Ferrantini, . . . I. Olivotto, *Long-Term Prevalence of Systolic Dysfunction in MYBPC3 Versus MYH7-Related Hypertrophic Cardiomyopathy*. Circ Genom Precis Med, 2023. **16**(4): p. 363-371.

67. Raman, B., R. Ariga, M. Spartera, S. Sivalokanathan, K. Chan, S. Dass, . . . S. Neubauer, *Progression of myocardial fibrosis in hypertrophic cardiomyopathy: mechanisms and clinical implications*. Eur Heart J Cardiovasc Imaging, 2019. **20**(2): p. 157-167.

68. Eijgenraam, T.R., H.H.W. Sillje, and R.A. de Boer, *Current understanding of fibrosis in genetic cardiomyopathies*. Trends Cardiovasc Med, 2020. **30**(6): p. 353-361.

69. Ho, C.Y., B. Lopez, O.R. Coelho-Filho, N.K. Lakdawala, A.L. Cirino, P. Jarolim, . . . C.E. Seidman, *Myocardial fibrosis as an early manifestation of hypertrophic cardiomyopathy*. N Engl J Med, 2010. **363**(6): p. 552-63.

70. Kim, J.B., G.J. Porreca, L. Song, S.C. Greenway, J.M. Gorham, G.M. Church, . . . J.G. Seidman, *Polony multiplex analysis of gene expression (PMAGE) in mouse hypertrophic cardiomyopathy*. Science, 2007. **316**(5830): p. 1481-4.

71. Frangogiannis, N.G., *Cardiac fibrosis*. Cardiovasc Res, 2021. **117**(6): p. 1450-1488.

72. Weber, K.T., *Cardiac interstitium in health and disease: the fibrillar collagen network*. J Am Coll Cardiol, 1989. **13**(7): p. 1637-52.

73. Bajpai, G., C. Schneider, N. Wong, A. Bredemeyer, M. Hulsmans, M. Nahrendorf, . . . K.J. Lavine, *The human heart contains distinct macrophage subsets with divergent origins and functions*. Nat Med, 2018. **24**(8): p. 1234-1245.

74. Epelman, S., K.J. Lavine, A.E. Beaudin, D.K. Sojka, J.A. Carrero, B. Calderon, . . . D.L. Mann, *Embryonic and adult-derived resident cardiac macrophages are maintained through distinct mechanisms at steady state and during inflammation*. Immunity, 2014. **40**(1): p. 91-104.

75. Ivey, M.J., J.T. Kuwabara, K.L. Riggsbee, and M.D. Tallquist, *Platelet-derived growth factor receptor-alpha is essential for cardiac fibroblast survival*. Am J Physiol Heart Circ Physiol, 2019. **317**(2): p. H330-H344.

76. Tallquist, M.D., *Cardiac Fibroblast Diversity*. Annu Rev Physiol, 2020. **82**: p. 63-78.

77. Hinz, B., *The myofibroblast: paradigm for a mechanically active cell*. J Biomech, 2010. **43**(1): p. 146-55.

78. Carlson, S., D. Helterline, L. Asbe, S. Dupras, E. Minami, S. Farris, and A. Stempien-Otero, *Cardiac macrophages adopt profibrotic/M2 phenotype in infarcted hearts: Role of urokinase plasminogen activator*. J Mol Cell Cardiol, 2017. **108**: p. 42-49.

79. Nevers, T., A.M. Salvador, A. Grodecki-Pena, A. Knapp, F. Velazquez, M. Aronovitz, . . . P. Alcaide, *Left Ventricular T-Cell Recruitment Contributes to the Pathogenesis of Heart Failure*. Circ Heart Fail, 2015. **8**(4): p. 776-87.

80. Shiraishi, M., Y. Shintani, Y. Shintani, H. Ishida, R. Saba, A. Yamaguchi, . . . K. Suzuki, *Alternatively activated macrophages determine repair of the infarcted adult murine heart*. J Clin Invest, 2016. **126**(6): p. 2151-66.

81. Sun, X., B. Nkennor, O. Mastikhina, K. Soon, and S.S. Nunes, *Endothelium-mediated contributions to fibrosis*. Semin Cell Dev Biol, 2020. **101**: p. 78-86.

82. Nakamori, S., E.J. Rowin, J. Rodriguez, L.H. Ngo, W.J. Manning, M. Maron, and R. Nezafat, *Accelerated myocardial fibrosis in young to middle-aged patients with hypertrophic cardiomyopathy*. J Cardiovasc Magn Reson, 2024. **26**(2): p. 101072.

83. Weissler-Snir, A., K. Allan, K. Cunningham, K.A. Connelly, D.S. Lee, D.A. Spears, . . . P. Dorian, *Hypertrophic Cardiomyopathy-Related Sudden Cardiac Death in Young People in Ontario*. Circulation, 2019. **140**(21): p. 1706-1716.

84. Nollet, E.E., I. Duursma, A. Rozenbaum, M. Eggelbusch, R.C.I. Wust, S.A.C. Schoonvelde, . . . J. van der Velden, *Mitochondrial dysfunction in human hypertrophic cardiomyopathy is linked to cardiomyocyte architecture disruption and corrected by improving NADH-driven mitochondrial respiration*. Eur Heart J, 2023. **44**(13): p. 1170-1185.

85. Spindler, M., K.W. Saupe, M.E. Christe, H.L. Sweeney, C.E. Seidman, J.G. Seidman, and J.S. Ingwall, *Diastolic dysfunction and altered energetics in the alphaMHC403/+ mouse model of familial hypertrophic cardiomyopathy*. J Clin Invest, 1998. **101**(8): p. 1775-83.

86. Crilley, J.G., E.A. Boehm, E. Blair, B. Rajagopalan, A.M. Blamire, P. Styles, . . . H. Watkins, *Hypertrophic cardiomyopathy due to sarcomeric gene mutations is characterized by impaired energy metabolism irrespective of the degree of hypertrophy*. J Am Coll Cardiol, 2003. **41**(10): p. 1776-82.

87. Lopaschuk, G.D., Q.G. Karwi, R. Tian, A.R. Wende, and E.D. Abel, *Cardiac Energy Metabolism in Heart Failure*. Circ Res, 2021. **128**(10): p. 1487-1513.

88. Pal, N., A. Acharjee, Z. Ament, T. Dent, A. Yavari, M. Mahmod, . . . J.L. Griffin, *Metabolic profiling of aortic stenosis and hypertrophic cardiomyopathy identifies mechanistic contrasts in substrate utilization*. FASEB J, 2024. **38**(6): p. e23505.

89. Previs, M.J., T.S. O'Leary, M.P. Morley, B.M. Palmer, M. LeWinter, J.M. Yob, . . . S.M. Day, *Defects in the Proteome and Metabolome in Human Hypertrophic Cardiomyopathy*. Circ Heart Fail, 2022. **15**(6): p. e009521.

90. Schuldt, M., J. Pei, M. Harakalova, L.M. Dorsch, S. Schlossarek, M. Mokry, . . . D.W.D. Kuster, *Proteomic and Functional Studies Reveal Detyrosinated Tubulin as Treatment Target in Sarcomere Mutation-Induced Hypertrophic Cardiomyopathy*. Circ Heart Fail, 2021. **14**(1): p. e007022.

91. Li, B., F. Liu, X. Chen, T. Chen, J. Zhang, Y. Liu, . . . Y. Wu, *FARS2 Deficiency Causes Cardiomyopathy by Disrupting Mitochondrial Homeostasis and the Mitochondrial Quality Control System*. Circulation, 2024. **149**(16): p. 1268-1284.

92. van der Velden, J., C.G. Tocchetti, G. Varricchi, A. Bianco, V. Sequeira, D. Hilfiker-Kleiner, . . . S. Heymans, *Metabolic changes in hypertrophic cardiomyopathies: scientific update from the Working Group of Myocardial Function of the European Society of Cardiology*. Cardiovasc Res, 2018. **114**(10): p. 1273-1280.

93. Lehman, S.J., L. Tal-Grinspan, M.L. Lynn, J. Strom, G.E. Benitez, M.E. Anderson, and J.C. Tardiff, *Chronic Calmodulin-Kinase II Activation Drives Disease Progression in Mutation-Specific Hypertrophic Cardiomyopathy*. Circulation, 2019. **139**(12): p. 1517-1529.

94. Helms, A.S., F.J. Alvarado, J. Yob, V.T. Tang, F. Pagani, M.W. Russell, . . . S.M. Day, *Genotype-Dependent and -Independent Calcium Signaling Dysregulation in Human Hypertrophic Cardiomyopathy*. Circulation, 2016. **134**(22): p. 1738-1748.

95. Hutt, E. and M.Y. Desai, *Medical Treatment Strategies for Hypertrophic Cardiomyopathy*. Am J Cardiol, 2024. **212S**: p. S33-S41.

96. Adler, A., D. Fourey, A. Weissler-Snir, W. Hindieh, R.H. Chan, M.H. Gollob, and H. Rakowski, *Safety of Outpatient Initiation of Disopyramide for Obstructive Hypertrophic Cardiomyopathy Patients*. J Am Heart Assoc, 2017. **6**(6).

97. Ommen, S.R., B.J. Maron, I. Olivotto, M.S. Maron, F. Cecchi, S. Betocchi, . . . R.A. Nishimura, *Long-term effects of surgical septal myectomy on survival in patients with obstructive hypertrophic cardiomyopathy*. J Am Coll Cardiol, 2005. **46**(3): p. 470-6.

98. Pelliccia, F., G. Niccoli, F. Gragnano, G. Limongelli, E. Moscarella, G. Ando, . . . P. Calabro, *Alcohol septal ablation for hypertrophic obstructive cardiomyopathy: a contemporary reappraisal*. EuroIntervention, 2019. **15**(5): p. 411-417.

99. Ta, S., J. Li, D.H. Hsi, R. Hu, C. Lei, B. Shan, . . . L. Liu, *Percutaneous intramyocardial septal radiofrequency ablation after 5-year follow-up*. Heart, 2024. **110**(11): p. 792-799.

100. Fang, J., Y. Liu, Y. Zhu, R. Li, R. Wang, D.W. Wang, . . . X. Wei, *First-in-Human Transapical Beating-Heart Septal Myectomy in Patients With Hypertrophic Obstructive Cardiomyopathy*. J Am Coll Cardiol, 2023. **82**(7): p. 575-586.

101. Anderson, D.M., G.L. Raff, T.A. Ports, B.H. Brundage, W.W. Parmley, and K. Chatterjee, *Hypertrophic obstructive cardiomyopathy. Effects of acute and chronic verapamil treatment on left ventricular systolic and diastolic function*. Br Heart J, 1984. **51**(5): p. 523-9.

102. Sherrid, M.V., I. Barac, W.J. McKenna, P.M. Elliott, S. Dickie, L. Chojnowska, . . . B.J. Maron, *Multicenter study of the efficacy and safety of disopyramide in obstructive hypertrophic cardiomyopathy*. J Am Coll Cardiol, 2005. **45**(8): p. 1251-8.

103. Saberi, S., N. Cardim, M. Yamani, J. Schulz-Menger, W. Li, V. Florea, . . . D. Jacoby, *Mavacamten Favorably Impacts Cardiac Structure in Obstructive Hypertrophic Cardiomyopathy: EXPLORER-HCM Cardiac Magnetic Resonance Substudy Analysis*. Circulation, 2021. **143**(6): p. 606-608.

104. Braunwald, E., S. Saberi, T.P. Abraham, P.M. Elliott, and I. Olivotto, *Mavacamten: a first-in-class myosin inhibitor for obstructive hypertrophic cardiomyopathy*. Eur Heart J, 2023. **44**(44): p. 4622-4633.

105. Mentias, A., N.G. Smedira, A. Krishnaswamy, G.W. Reed, S. Ospina, M. Thamilarasan, . . . M.Y. Desai, *Survival After Septal Reduction in Patients >65 Years Old With Obstructive Hypertrophic Cardiomyopathy*. J Am Coll Cardiol, 2023. **81**(2): p. 105-115.

106. Chang, R., D. Luo, W. He, W. Tang, J. Chen, J. Li, . . . L. Wang, *A novel method for septal reduction therapy by three-dimensional guided transvenous intraseptal pulsed-field ablation*. Heart Rhythm, 2024. **21**(3): p. 258-267.

107. Mohal, J.S., Z.I. Whinnett, S.A. Mohiddin, J. Malcolmson, P. Elliott, J.O.M. Ormerod, . . . A.D. Arnold, *Electromechanically Optimized Right Ventricular Pacing for Obstructive Hypertrophic Cardiomyopathy (EMORI-HCM)*. J Am Coll Cardiol, 2025.

108. Gergely, T.G., T. Kovacs, A. Kovacs, V.E. Toth, N.V. Sayour, G.M. Morotz, . . . Z.V. Varga, *CardiLect: A combined cross-species lectin histochemistry protocol for the automated analysis of cardiac remodelling*. ESC Heart Fail, 2024.

109. Toepfer, C.N., A.C. Garfinkel, G. Venturini, H. Wakimoto, G. Repetti, L. Alamo, . . . C.E. Seidman, *Myosin Sequestration Regulates Sarcomere Function, Cardiomyocyte Energetics, and Metabolism, Informing the Pathogenesis of Hypertrophic Cardiomyopathy*. Circulation, 2020. **141**(10): p. 828-842.

110. Braunwald, E., *Hypertrophic Cardiomyopathy: A Brief Overview*. Am J Cardiol, 2024. **212S**: p. S1-S3.

111. Wang, J., S. Yang, X. Ma, K. Zhao, K. Yang, S. Yu, . . . S. Zhao, *Assessment of late gadolinium enhancement in hypertrophic cardiomyopathy improves risk stratification based on current guidelines*. Eur Heart J, 2023. **44**(45): p. 4781-4792.

112. Allouba, M., R. Walsh, A. Afify, M. Hosny, S. Halawa, A. Galal, . . . Y. Aguib, *Ethnicity, consanguinity, and genetic architecture of hypertrophic cardiomyopathy*. Eur Heart J, 2023. **44**(48): p. 5146-5158.

113. Walsh, R., R. Buchan, A. Wilk, S. John, L.E. Felkin, K.L. Thomson, . . . S.A. Cook, *Defining the genetic architecture of hypertrophic cardiomyopathy: re-evaluating the role of non-sarcomeric genes*. Eur Heart J, 2017. **38**(46): p. 3461-3468.

114. Geier, C., A. Perrot, C. Ozcelik, P. Binner, D. Counsell, K. Hoffmann, . . . K.J. Osterziel, *Mutations in the human muscle LIM protein gene in families with hypertrophic cardiomyopathy*. Circulation, 2003. **107**(10): p. 1390-5.

115. Mosqueira, D., J.G.W. Smith, J.R. Bhagwan, and C. Denning, *Modeling Hypertrophic Cardiomyopathy: Mechanistic Insights and Pharmacological Intervention*. Trends Mol Med, 2019. **25**(9): p. 775-790.

116. Vakrou, S., Y. Liu, L. Zhu, G.V. Greenland, B. Simsek, V.B. Hebl, . . . M.R. Abraham, *Differences in molecular phenotype in mouse and human hypertrophic cardiomyopathy*. Sci Rep, 2021. **11**(1): p. 13163.

117. Vullaganti, S., J. Levine, N. Raiker, A.A. Syed, J.D. Collins, J.C. Carr, . . . L. Choudhury, *Fibrosis in Hypertrophic Cardiomyopathy Patients With and Without Sarcomere Gene Mutations*. Heart Lung Circ, 2021. **30**(10): p. 1496-1501.

118. Habib, M., A. Adler, K. Fardfini, S. Hoss, K. Hanneman, E.J. Rowin, . . . R.H. Chan, *Progression of Myocardial Fibrosis in Hypertrophic Cardiomyopathy: A Cardiac Magnetic Resonance Study*. JACC Cardiovasc Imaging, 2021. **14**(5): p. 947-958.

119. Spudich, J.A., *Three perspectives on the molecular basis of hypercontractility caused by hypertrophic cardiomyopathy mutations*. Pflugers Arch, 2019. **471**(5): p. 701-717.

120. Maron, B.J. and M.S. Maron, *Hypertrophic cardiomyopathy*. Lancet, 2013. **381**(9862): p. 242-55.

121. Elliott, P. and W.J. McKenna, *Hypertrophic cardiomyopathy*. Lancet, 2004. **363**(9424): p. 1881-91.

122. Li, X., F. Wu, S. Gunther, M. Looso, C. Kuenne, T. Zhang, . . . T. Braun, *Inhibition of fatty acid oxidation enables heart regeneration in adult mice*. Nature, 2023. **622**(7983): p. 619-626.

123. Angelini, A., P.K. Saha, A. Jain, S.Y. Jung, R.L. Mynatt, X. Pi, and L. Xie, *PHDs/CPT1B/VDAC1 axis regulates long-chain fatty acid oxidation in cardiomyocytes*. Cell Rep, 2021. **37**(1): p. 109767.

124. Unno, K., S. Isobe, H. Izawa, X.W. Cheng, M. Kobayashi, A. Hirashiki, . . . T. Murohara, *Relation of functional and morphological changes in mitochondria to myocardial contractile and relaxation reserves in asymptomatic to mildly*

symptomatic patients with hypertrophic cardiomyopathy. Eur Heart J, 2009. **30**(15): p. 1853-62.

125. Liu, X. and Z. Chen, *The pathophysiological role of mitochondrial oxidative stress in lung diseases*. J Transl Med, 2017. **15**(1): p. 207.

126. Nicolas-Avila, J.A., A.V. Lechuga-Vieco, L. Esteban-Martinez, M. Sanchez-Diaz, E. Diaz-Garcia, D.J. Santiago, . . . A. Hidalgo, *A Network of Macrophages Supports Mitochondrial Homeostasis in the Heart*. Cell, 2020. **183**(1): p. 94-109 e23.

127. Coote, J.H. and R.A. Chauhan, *The sympathetic innervation of the heart: Important new insights*. Auton Neurosci, 2016. **199**: p. 17-23.